Author:
Brustad, Synne C C

Title:
The relationship between the Atlantic meridional overturning circulation and coastal sea level in CMIP5 models

The relationship between the Atlantic meridional overturning circulation and coastal sea level in CMIP5 models

Synne Christin Castberg Brustad

A dissertation submitted to the University of Bristol in accordance with the requirements for award of the degree of Masters of Science by Research (MScR) in the Faculty of Science.

School of Geographical Sciences

University of Bristol

December 2019

Word count: 29 878

Abstract

The importance of the Atlantic meridional overturning circulation (AMOC) for the Earth's climate is widely recognised. As a complement to temporally and spatially scarce in-situ AMOC observations, several studies have sought a connection between AMOC and sea level variability. Tide gauges and coastal sea level (CSL) are of special interest as they offer over century-long data and cost-effective monitoring. Yet, to what extent AMOC variability influences CSL is subject to conflicting evidence, challenging the validity of CSL as AMOC proxies.

This study examines the relationship between the AMOC and sea level variability along the North American east coast in a large number (>40) of CMIP5 models over the period 1920-2300 on interannual and decadal timescales. As such it extends existing studies having focused primarily on a single ocean model, observations or a limited subset of state-of-the-art coupled models. The spatiotemporal characteristics of the relationship are examined by; 1) assessing the direct relationship, including a comparison between initial AMOC simulations and a sea surface height-based reconstruction of the AMOC derived from linear regression, and 2) calculating an AMOC index based on alongshore CSL composites. About half of the CMIP5 models generate moderate to strong AMOC-CSL anticorrelations (<-0.5) along large latitudinal stretches, particularly between 35°N-48°N, on decadal timescales in both historical simulations and 21st century projections. Concurrently, if extending the analysis up to year 2300, a noticeable intra-model spread is noted in the magnitude of the relationship over the four different 100-yr intervals (1900-2300), suggesting that the AMOC-CSL relationship may be non-stationary and dependent on the temporal period examined. The models generally underestimate both the observed AMOC and CSL variability. The implications of these results are discussed with a focus on the suitability of CSL-based AMOC proxies, reliability of CMIP5 projections and future CSL changes.

Acknowledgements

First and foremost, I would like to thank my supervisor, Rory Bingham, for his invaluable help and support as he has guided me from beginning to end of this project. I am very grateful for Rory's smart advise that forced me to think critically and logically as a scientist, and for his encouraging words and support in the middle of a very difficult time getting medical treatment and surgery across the Pond.

I would also like to thank my second supervisor, Paul Valdes, for the inspirational and interesting discussions about climate modelling and its many challenges.

Big thanks to Browns for being such a welcoming, friendly and fun bunch of people! I am particularly grateful to Iskra for all the chats about all or nothing, laughs and help – you are my favourite hydrologist on this planet and a dear friend! Huge thanks to Claire and Emily for all the fun times and help with small and big matters. Thanks also to Peter, Stefan, Erik, Matt, Rebeca, Alan for words of advice and rescue programming insights.

Lastly but certainly not least, my thanks go to Anders, for being my solid rock throughout everything. I could not have done it without you. I am certain you are as excited as I am, if not more so, that I finally managed to press the submit button.

Declaration of Authorship

I declare that the work in this dissertation was carried out in accordance with the requirements of the University's Regulations and Code of Practice for Research Degree Programmes and that it has not been submitted for any other academic award. Except where indicated by specific reference in the text, the work is the candidate's own work. Work done in collaboration with, or with the assistance of, others, is indicated as such. Any views expressed in the dissertation are those of the author.

Synne C. C. Brustad
17.12.2019

Table of Contents

List of Figures

List of Tables

1 Introduction

1.1 Background

The importance of the Atlantic meridional overturning circulation (AMOC) for the Earth's climate is widely recognized (Kuhlbrodt et al. 2007, Roberts and Palmer 2012, Kienert and Rahmstorf 2012, IPCC 2013). While there is broad agreement between the latest generation of state-of-the-art-models that the AMOC will weaken over the 21st century in response to elevated atmospheric greenhouse gases (Collins et al. 2013, Kirtman et al. 2013, Buckley and Marshall 2015, Srokosz et al. 2012, Cheng et al. 2013), there is still inter-model disagreement with respect to both the amplitude and frequency of AMOC change (Medhaug and Furevik 2011, Kirtman et al. 2013, Zhang and Wang 2013). In addition, there is low confidence in evaluating the ocean circulation beyond 2100 (Collins et al. 2013:1095). Since changes in the AMOC could have profound impacts on multiple aspects of the regional Atlantic and global climate system, such as on rainfall and sea level (Roberts and Palmer 2012, Levermann et al. 2012, Reintges et al. 2016), it is crucial to find the best methods that can help minimize uncertainty and detect the large-scale circulation's future behaviour.

March 2019 marked 15-years of unique continuous basin-wide measurements of the AMOC's strength and vertical structure at 26.5°N by the RAPID monitoring system. However, the observational record is still too short to adequately evaluate the AMOC predictions and if the circulation's observed decline of ~ -0.5 Sverdrup (1 Sv = 10^6 m^3 s^{-1}) per year since 2004 (Smeed et al. 2014, Srokosz and Bryden 2015) is a continuing trend caused by global warming (Robson et al. 2014), a result of natural variability (Blaker et al. 2014, Roberts et al. 2014) or a combination (Schiermeier 2014). While longer in-situ measurements are pending, the use of coastal sea level (CSL) data in detecting climatic changes in the AMOC is of special interest given how it renders the prospect of relatively low-cost monitoring; besides, tide gauge based reconstructions can provide over century-long data (Ezer 2013). Tide gauge-based dynamic sea level along the North American east coast has received particular attention (Little et al. 2017). Nevertheless, we still need to determine the robustness of Atlantic sea level-based AMOC "fingerprints".

Several studies have sought and found a strong connection between the AMOC and coastal sea level (CSL) variability along the North American east coast (NAEC), particularly on interannual (e.g. Bingham and Hughes 2009, Goddard et al. 2015), decadal (e.g. Hakkinen 2001, Ezer 1999, 2001) and/or multidecadal timescales (e.g. Kopp 2013, Ezer 2013, Little et al. 2017). In addition, the recent (~1975) observed sea level rise (SLR) acceleration in the coastal region stretching from Cape Hatteras (35.1°N) to Boston (42.4°N) (Kopp 2013) might

be driven by a slowdown in the AMOC via the geostrophic balance (Sallenger et al. 2012, Bouttes et al. 2014, Ezer 2013, 2015, McCarthy et al. 2012, 2015, Yin and Goddard 2013). Yet, it is not known whether this recent SLR acceleration reflects the onset of a predicted secular decline in the AMOC (Park and Sweet 2015), or even if it is AMOC related (see e.g. Woodworth et al. 2014, Piecuch et al. 2019).

Here I investigate the relationship between the AMOC and coastal sea level variability along the North American east coast in a large number of CMIP5 models (> 40 for historical simulations and maximum available for future scenarios) over the period 1920-2300. I assess both historical and future simulations and compare the historical runs to observational records in up to 48 models used in the latest Intergovernmental Panel Assessment Report (IPCC Fifth Assessment Report [AR5]). The focus is on maximizing model output, with the overarching aim of detecting general CMIP5 model patterns and outlying behavior. That is, the goal is not to assess the individual CMIP5 models in detail, but diagnose general patterns in model performance, detect outlying behavior and propose origins of model disagreements. The desired outcome is that the analysis can help facilitate future model development and highlight areas of poor model representation in simulations of the AMOC and North Atlantic coastal sea level.

1.2 Aim and Objectives

The overall aim of this project is to assess the robustness of the relationship between the AMOC and coastal sea level variability along the North American east coast across a large number of CMIP5 models. The focus is on interannual and decadal variability. I will also compare the AMOC and sea level simulations against available observations.

The overarching research questions of the project are:

1. *How well do the CMIP5 models represent the Atlantic meridional overturning circulation?*

2. *How well do the CMIP5 models represent sea level variability along the North American east coast?*

3. *Do the CMIP5 models indicate that coastal dynamic sea level can act as an important "fingerprint" of the AMOC?*

The following objectives were defined to meet these aims:

1. **Examine the representation of the AMOC in the CMIP5 models**, including the streamfunction, upper-layer transport and latitudinal coherence, as well as how the AMOC simulations compare to available observations.

2. **Assess the temporal and spatial representation of coastal sea level in CMIP5 models in relation to tide gauge data.**

3. **Evaluate the spatial and temporal characteristics of the AMOC-sea level relationship in CMIP5 models in historical (1850-2006) simulations.** To do this the direct relationship is assessed by correlation metrics, and an AMOC reconstruction is obtained from a linear regression model relating coastal sea level variability to AMOC strength. A sea surface height-based ocean circulation index is then developed and tested by using alongshore sea level composites.

4. **Explore the stability of the AMOC-coastal sea level relationship in future 21st-23rd century projections under the RCP2.6 and RCP8.5 forcing scenarios.**

1.3 Thesis Outline

Chapter 2 reviews the literature on the relation between the Atlantic meridional overturning circulation and coastal sea level along the North American east coast. It elaborates on why studying this relationship is important in research aimed at enhancing our understanding of the ocean circulation's past, present and future behavior.

Chapter 3 introduces the data and methods used in this study. The CMIP5 experiments and models, the CMIP5 sea surface height variable and the AMOC calculation are described. Further, it outlines the observational data used in the study and how the observational records and simulations are processed in order to obtain comparable data. Finally, the chapter details how the relationships between the AMOC and sea level are derived and the metrics applied for CMIP5 model assessment.

Chapter 4 compares the CMIP5 models with observations. It assesses the CMIP5 models abilities to represent the AMOC and both the temporal variability and spatial patterns of Atlantic sea surface height, in relation to tide gauge records.

Chapter 5 examines the AMOC-sea level relationship as captured by the CMIP5 models using two different approaches. Furthermore, the chapter compares the modelled and observed AMOC-sea level relationship and explores the stability of the relationship under global warming.

Chapter 6 discusses whether the results indicate if sea level can act as a tool to monitor the AMOC. I provide final comments on the ability of CMIP5 models to represent sea level and AMOC fields and the robustness of their connection. I also highlight what are the important implications for future sea level, and address limitations and suggest a path for future work.

Chapter 7 provides overall conclusions.

2 Literature Review

2.1 Description of the AMOC

The Atlantic meridional overturning circulation (AMOC) is a basin-wide meridional two-cell ocean current system in the Atlantic Ocean. The upper cell of the AMOC consists of a northward flow of warm, tropical, salty water moving from the South Atlantic to the North Atlantic's high latitudes via the Gulf Stream and the North Atlantic Current (Srokosz et al. 2012, Buckley and Marshall 2015 Muthers et al. 2016, see *Figure 2.1*). These waters cool in transit to and within the sub-polar North Atlantic, releasing heat to the atmosphere and increasing the density of seawater. When sufficiently dense, these waters sink and flow southward at great depths between ~1,500–4,500 m (Lecci et al. 2016). This southward flowing limb of water, termed the North Atlantic Deep Waters (NADW) (Delworth et al. 2008), flows from the Atlantic to the Southern Ocean where large parts of it upwell and rise to the surface around Antarctica. Parts of this water circulate Antarctica before joining the rest of the deep global oceans.

The AMOC's "deep" cell originates near Antarctica and is composed of the Antarctic Bottom Waters (AABW) (Orsi et al. 1999). The AABW are denser than NADW and flow northward at abyssal depths below ~ 4,500 m and gradually rise and mix onto the lower sections of the southward-flowing NADW (Brix and Gerdes 2003, Gregorio et al. 2015). The Antarctic Intermediate Waters (AAIW) move northward above the NADW. Noticeably, the NADW in the western Atlantic has a residence time of ~100 years (Broecker 1979), implying that the average parcel of NADW spends a century in the Atlantic's deep waters.

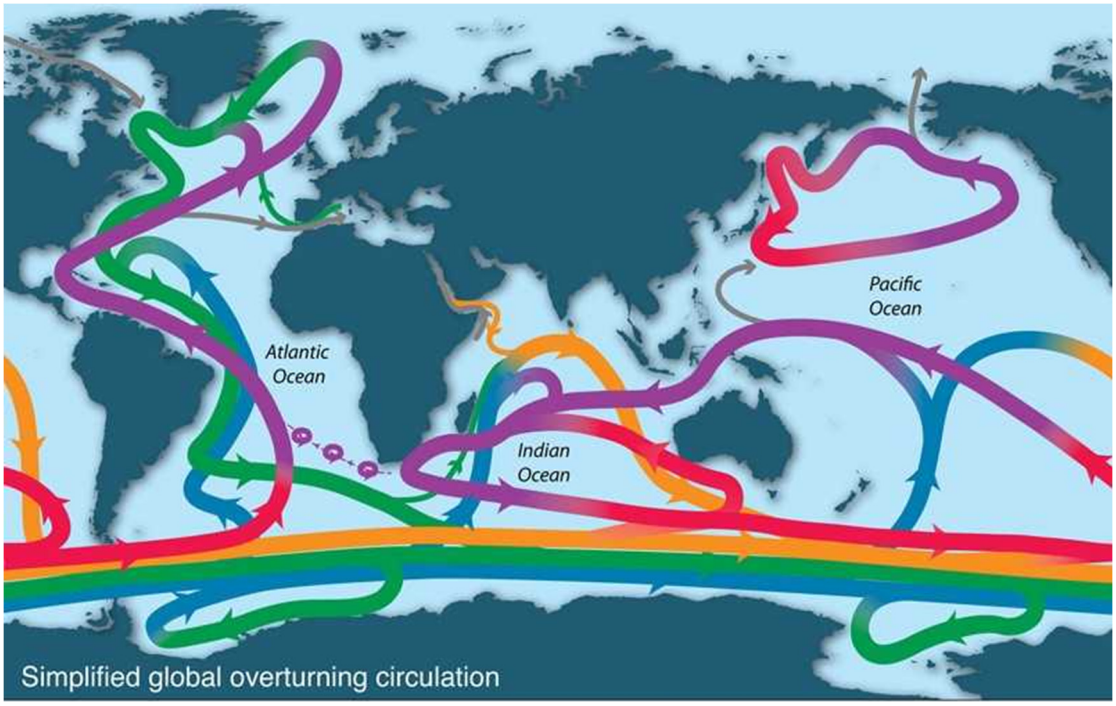

Figure 2.1. A schematic of global overturning circulation and its components. Purple = upper ocean and thermocline. Red = intermediate water and denser thermocline. Green = North Atlantic Deep Water. Orange = Indian Deep Water and Pacific Deep Water. Blue = Antarctic Bottom Water. Grey = Mediterranean and Red Sea inflows and Bering Strait components. Obtained from Talley (2013), based on Schmitz (1995). Downloaded 5 June 2017 from Talley (2013).

2.1.1 What drives the AMOC?

What drives the AMOC in the sense of returning the water back to the surface from deep depths, have often been boiled down to two mechanisms. The first mechanism was proposed by Sandstrom (1916) and Jeffreys (1925), and is often referred to as the traditional thermohaline driving mechanism. This driver involves transport of relatively warm surface waters to the deep ocean, descending across surfaces of equal density (i.e. diapycnal mixing) (Kuhlbrodt et al. 2007). Munk and Wunsch (1998) provide details on this mechanism and highlight how winds and tides create a fragmenting of internal waves, whereby these waves disperse into small-scale motion and manifest as turbulent mixing. This blending of heat makes the deep water masses less dense and they will therefore move upwards in low latitudes (Kuhlbrodt et al. 2007).

The other mechanism, wind-driven upwelling, was suggested by Toggweiler and Samuels (1993, 1995, 1998) and concerns how surface wind stress, facilitated by the Drake Passage, drive substantial upwelling in the Southern Ocean. Being a deep waterway between the South American and the Antarctic Peninsula, the Drake Passage sets the conditions for the Antarctic Circumpolar circulation, a strong zonal current and the only current to completely encircle the

Earth (Ostapoff 1960, Peterson 1988, Schewe 2007). The strong westerly winds combine with the Coriolis force to generate a northward flow of water, referred to as the Ekman transport (Ekman 1905). The Ekman divergence around Antarctica generates a pumping up of large amounts of water along the sloping density layers from the deep ocean to the surface (Toggweiler and Samuels 1995). The upwelled water is then carried northwards out of the circumpolar area with the Ekman layer, or cooled close to Antarctica's sea ice and transformed to bottom waters (Schewe 2007).

2.2 The AMOC and its role in the climate system

As the Atlantic branch of the great, global ocean "conveyor belt" (Broecker 1991), the AMOC plays a vital role in the transportation and distribution of heat, freshwater and biogeochemical properties (e.g. carbon) around the world (Boulton et al. 2014, Reintges et al. 2016). At 24°-26°N, where the maximum Atlantic Ocean heat transport occurs, the AMOC transfers approximately 1.3 petawatt (1PW = 10^{15} W) of heat northwards (Hall and Bryden 1982, Lavin et al. 1998, Johns et al. 2011), accounting for potentially 70 per cent of the net poleward heat flux moved by the global oceans at these latitudes (Hall and Bryden 1982, Johns et al. 2011). As this heat is advected towards the polar region, there is a strong oceanic heat transfer to the atmosphere at mid-latitudes, making the AMOC a major factor explaining the temperate climate of northwest Europe (Palter 2014, Yamamoto et al. 2015). Notably, AMOC heat transport is thought to play a decisive role in why, for example, Dublin (Ireland) is over 4°C warmer than Seattle (USA) in wintertime, although the latter is 6° of latitude closer to the equator (McCarthy et al. 2015).

Across the equator, the AMOC carries approximately ~0.5 petawatt of heat (Marshall et al. 2014, Buckley and Marshall 2015). There are two major impacts of this. First, as a compensation for the substantial northward ocean heat transport, the Intertropical Convergence Zone is set just north of the equator (Frierson et al. 2013) and the atmospheric heat transport is southward across the equator (Marshall et al. 2014, Buckley and Marshall 2015). Second, due to the AMOC's cross-equatorial heat transfer the ocean and atmosphere are approximately 2°C warmer in the Northern compared to the Southern Hemisphere (Feulner et al. 2013). Since the Northern Hemisphere exhibits slightly higher temperatures, it emits more outgoing infrared radiation at low energy than the Southern Hemisphere, resulting in a small asymmetry in radiation at top-of-the-atmosphere (Kang et al. 2014). Ultimately, the AMOC is bridging the hemispheres causing inter-hemispheric climate imbalances (Buckley and Marshall 2015).

Observational and modelling studies have linked a weakening of the AMOC to multiple processes, including subpolar Atlantic cooling (Caesar et al. 2018), a temporary equatorward relocation in the inter-tropical convergence zone (Broccoli et al. 2006, Kang et al. 2008, Marshall et al. 2014, Green and Marshall 2017), drying of the Sahelian and Caribbean regions (Vellinga and Wood 2008, Brayshaw et al. 2009), and weakening of the Asian summer monsoons (Zhang and Delworth 2005, Delworth et al. 2008). AMOC changes could further affect the Walker circulation (Delworth et al. 2008:316), North American drought, Atlantic hurricane activity (Vellinga and Wood 2002), the sink of Atlantic ocean CO_2 (Li et al. 2016), marine ecosystems (Schmittner 2005), and sea level changes (e.g. Levermann et al. 2005, Yin et al. 2009, Bingham and Hughes 2009, Howard et al. 2014).

Recently, research has paid more attention towards the AMOC's role in marine biogeochemistry and in the uptake and redistribution of CO_2 (e.g. Palter and Lozier 2008, Srokosz et al. 2012, Khatiwala et al. 2013, Halloran et al. 2015, Li et al. 2016). The North Atlantic is a key sink of atmospheric CO_2 (Khatiwala et al. 2013), holding approximately 40 per cent of the annual mean global air-sea flux of CO_2 (Li et al. 2016). The AMOC is thought to play a substantial role in generating this carbon sink in the North Atlantic (Perez et al. 2013). The storage of carbon at large depths in the North Atlantic is a result of the formation and bottomward diffusion of Labrador Sea waters and North Atlantic Deep Waters (Sabine et al. 2004). Thus, the deep storage of anthropogenic CO_2 in the North Atlantic is attributed to the AMOC's transportation of carbon-rich surface waters to depths where they are distributed via the overturning's lower cell. Changes in the AMOC is therefore closely linked to the carbon sequestration at ocean depths (Fontela et al. 2016).

2.2.1 Past climate

The last glacial period (~110-10ka before present), and probably also periods prior to this (Barker et al. 2011), were characterised by large, wide-ranging and often abrupt climatic changes at millennial timescales. Many of these abrupt climatic events have been connected to changes in the AMOC's northward heat transport and corresponding feedbacks (Broecker et al. 1985, Clark et al. 2002, 2007, Broecker 2006, Alley 2007, Boulton et al. 2014, Lynch-Stieglitz 2017).

The first abrupt climate change event linked to a decline or collapse of the AMOC was the Younger Dryas (Rooth 1982), characterised by a transition back to cooler conditions in the Northern Hemisphere during the deglaciation (Renssen et al. 2015). A prevailing paradigm is that there was a redirection of the melting Laurentide Ice sheet to the St. Lawrence River; this

might have provided sufficient freshwater inputs into the North Atlantic to interrupt the AMOC (Rooth 1982, Carlson 2013).

Much effort has been dedicated to understand the connection between the AMOC and Dansgaard-Oeschger (D/O) and Heinrich (H) events respectively; two types of abrupt climatic changes during last glacial period (Alvarez-Solas et al. 2013). The D/O events are characterised by decadal-scale rapid transitions between cold stadials and warm inter-stadials in the Northern Hemisphere (Bond et al. 1993). The Heinrich events specify the occurrence of anomalous discharge events from ice sheets at ~7,000-year intervals during the last glacial period (Long and Stoy 2013). Although the physical processes responsible for the D/O and Heinrich events are still disputed (Timmermann et al. 2003, Alvarez-Solas et al. 2011), there is strong evidence that changes in AMOC strength and its corresponding heat transport were involved in both events (Broecker et al. 1985, Sarnthein et al. 1994, Keigwin and Boyle 2000, Sarnthein et al. 2001, Clement and Peterson 2008, Lynch-Stieglitz 2017).

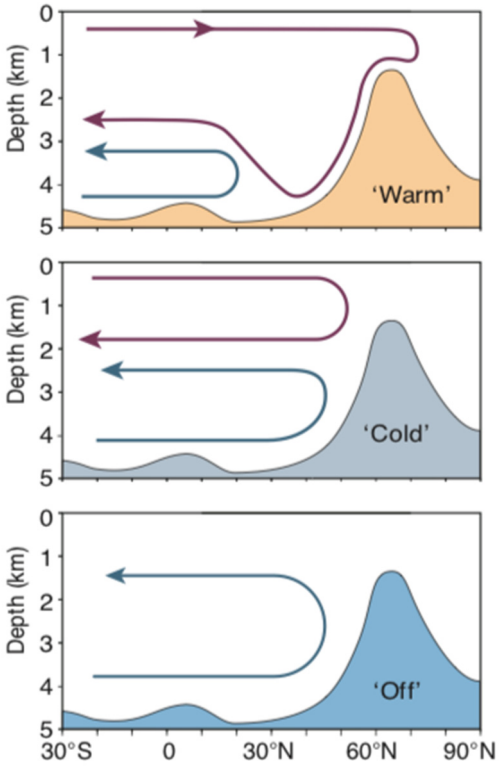

Figure 2.2. Illustration of the three conceptual modes of AMOC. Displayed is a segment of the Atlantic in the north-south direction. The elevation in bottom topography marks the sill between Scotland and Greenland. The red line marks the AMOC and the blue line marks the Antarctic bottom water. Adapted from Rahmstorf (2002).

In addition to the pioneering "on" and "off" modes conceptualised by Stommel (1961), which suggest that the AMOC might have more than one stable state, paleoclimate data indicates that the AMOC might have exhibited three different operation modes during the last glacial

period (Alley et al. 1999, Sarnthein et al. 1994). Rahmstorf (2002) characterises these as the "warm/interglacial", "cold/glacial" and "off/Heinrich" modes (*see Figure 2.2*). The "warm" mode corresponds to the AMOC configuration of today. The "cold" mode typifies the Last Glacial Maximum and in this state the AMOC existed but warm surface waters did not move as far north as the Nordic seas; the AMOC upper cell was generally shallower (Röhm et al. 2015). The "off" circulation state is thought to have dominated after large freshwater inputs, as during the Heinrich events, and marked by no warm northward water flowing at the surface and essentially a collapse of the deep water formation in the North Atlantic (Rahmstorf 2002).

2.2.2 Future climate

The AMOC is widely predicted to weaken over the 21st century in response to elevated atmospheric greenhouse gases (GHGs) and global warming (Gregory et al. 2005, Collins et al. 2012, Weaver et al. 2012, Kirtman et al. 2013, Buckley and Marshall 2015, Srokosz et al. 2012, Cheng et al. 2013). Nevertheless, there is large spread in state-of-the-art climate models' AMOC projections (Kirtman et al. 2013, Collins et al. 2013, Reintges et al. 2016), especially with respect to the circulation's magnitude of change (Liu et al. 2017). For projections over the 21st century, estimates of the AMOC decline range between 11% (1 to 24 %) in RCP2.6 and 34 % (12 to 54 %) in RCP8.5 (Collins et al. 2013:1095). The IPCC AR5 report (Collins et al. 2013:1095) deems a total collapse of the AMOC *very unlikely* by 2100, while highlighting that there is "low confidence" in evaluating the AMOC beyond 2100.

Much attention has been directed towards the melting of the Greenland ice sheet (GrIS) under global warming and its possible impacts on AMOC's future (Davini et al. 2015, Bakker et al. 2016, Yang et al. 2016). While it is clear that the recent acceleration of the GrIS melting is freshening the North Atlantic (Jiang et al. 2010, Rignot et al. 2011, Yang et al. 2013, Enderlin et al. 2014), it is less clear whether augmented freshwater flux is disturbing the AMOC (Yang et al. 2016). "Hosing experiments", studies where the freshwater balance of the North Atlantic is disrupted by imposing freshwater to the ocean basin artificially (Kageyama et al. 2013), have been applied to examine the AMOC's sensitivity to GrIS melting (Ridley et al. 2005, Swingedouw et al. 2013, Brunnabend et al. 2015). Some of these studies demonstrate that the strength of the AMOC is sensitive to melting of the GrIS (Fichefet et al. 2003, Brunnabend et al. 2015, Bakker et al. 2016, Sevellec et al. 2017), whereas other studies do not (Ridley et al. 2005, Jungclaus et al. 2006, Hu et al. 2011). It has been shown that as small additions of freshwater as 0.1 Sv (Rahmstorf et al. 2005, Hawkins et al. 2011) or even smaller amounts (Fichefet et al. 2003, Brunnabend et al. 2015), may impact the AMOC.

A major concern for future climate is whether the AMOC exhibits bistable behaviour. Recent work pinpoints that state-of-the-art climate models are subject to a critical bias in AMOC stability (Weber et al. 2007, Hofmann and Rahmstorf 2009, Huisman et al. 2010, Drijfout et al. 2011, Hawkins et al. 2011, Liu et al. 2014, Liu et al. 2017). Observational studies (e.g. Weijer et al. 1999, Bryden et al. 2011) suggest that the modern AMOC features multiple equilibria and thus unstable behaviour. This implies that the overturning might shift between "on" and "off" modes in the future, similar to its past behavior (Broecker et al. 1985, Rahmstorf 2002, Clark et al. 2002, McManus et al. 2004). Nonetheless, the latest generation of coupled climate models demonstrates a stable AMOC with single equilibrium (Stouffer et al. 2006, Hu et al. 2008, Liu et al. 2017).

Whether global warming is already slowing the AMOC is a matter of debate. Results from five repeat trans-Atlantic hydrographic sections at 25°N indicate that the AMOC has been declining ~ 30 per cent between 1957 and 2004 (Bryden et al. 2005). However, Kanzow et al. (2010) found no evidence of a 30 per cent decline and argue that Bryden et al.'s (2005) results are largely dependent on the 1957 estimate and that the observations might be misidentified by variability of higher (seasonal) frequencies. Between 2004 and 2012, the RAPID records have shown a rate of decline in the AMOC of ~ -0.54 Sv yr^{-1} (Smeed et al. 2014). Smeed et al. (2014) propose that this decline is more likely part of decadal-scale internal variability than a long-term trend induced by global warming. Recently, a handful of studies have argued that there is "no real evidence" for a persistent weakening secular trend of the AMOC in the light of global warming (Roberts et al. 2014, Buckley and Marshall 2015, Parker and Ollier 2016, Jackson et al. 2016).

2.3 The AMOC and decadal climate variability

Decadal variability is an important feature of the North Atlantic climate and adjoining land areas (Wu and Liu 2005). Most distinctly, the Atlantic multi-decadal oscillation (AMO, also called the Atlantic multidecadal variability) is a phenomenon of North Atlantic sea-surface temperatures (SSTs) with positive (negative) phases corresponding to warm (cool) SSTs anomalies across the entire subpolar North Atlantic (45° to 60° N). By controlling the subpolar gyre heat content, the AMOC is thought to be the driver of the AMO phases (McCarthy et al. 2015) and to influence SSTs (Delworth and Mann 2000). This is seen in both modelling studies (e.g. Delworth and Mann 2000) and indirect observations (e.g. McCarthy et al. 2015). However, it might also be the case that the AMOC and AMO interact with each other, with interdependent roles (Zhang and Wang 2013).

The AMO's implications for regional and global climate are many. For example, the negative/cool phase of the 1970s and 80s was marked by reduced precipitation and drought in Africa's Sahel region (Zhang and Delworth 2006) and arid summer conditions in Northwest Europe (Sutton and Dong 2012). The negative AMO phase has also been linked to the mid-1900s drop in global temperatures (Muller et al. 2013). The positive AMO phase starting in the mid-1990s, on the other hand, was associated with wet periods in the Sahel, heavy rainfall and high temperatures in Europe and substantial hurricane activity in the Caribbean (Goldenberg et al. 2001). Speculatively, the climatic impacts of a negative AMO phase might be a first indication of what we can expect in future climates in response to weakening of the AMOC (Bakker et al. 2016, McCarthy et al. 2017).

Although several studies have highlighted strong connections between the AMOC and AMO in climate models or by indirect observations, the direct observational record of the AMOC is still too short to validate this relation (McCarthy et al. 2017). It is also important to note that the role of the AMOC in driving the AMO per se has been challenged. For example, Booth et al. (2012) suggest that indirect aerosols can reproduce AMO patterns without the AMOC playing a role. At the same time, previous studies have also highlighted a connection between the AMOC, AMO and as well as the North Atlantic Oscillation (McCarthy et al. 2015, Sun et al. 2015), potentially via a multidecadal feedback loop (Yamamoto et al. 2018). Together these studies highlight the AMOC's uncertainty yet potential complex and interactive role in the climate system and possibilities of decadal climate predictability.

2.4 Monitoring the AMOC

Historically, observations of the AMOC and Atlantic Ocean heat transport (OHT) were infrequent, providing only snapshots of the overturning circulation (e.g. Bryden et al., 2005). Despite its crucial role in the climate system, and the uncertainty related to its future behaviour, the AMOC was not continuously monitored until the deployment of the RAPID monitoring system in March 2004 (Cunningham et al. 2007). Employed at 26.5°N between the Bahamas and Canary Islands, the RAPID mooring system is designed to supply continuous daily measurements of the Atlantic overturning's strength, variability and vertical structure and associated heat flux (Cunningham et al. 2007, Kanzow et al. 2007).

By design, the RAPID program combines in-situ data from "dynamic height" moorings (tall moorings with salinity, pressure and temperature recorders) on each side of the Atlantic zonally to monitor the geostrophic shear across the basin, with data from groups of moorings on the eastern (African) and western (Bahamas) boundaries (Johns and Beal 2008). Included are also current meters, pressure-equipped inverted echo sounders, cable-based flow

measurements through the Florida Straits and moorings on the flanks of the Mid-Atlantic Ridge (e.g. Baringer and Larsen 2001, Baehr et al. 2004, Cunningham et al. 2007, Delworth et al. 2008).

There are good reasons why the RAPID monitoring system is located at 26.5°N. First, at 26.5°N the northward flowing Gulf Stream moves through the Florida Straits where it can be monitored applying voltage across an already in place submarine cable (Larsen and Sanford 1985). Second, it is thought that 26.5°N is close to the latitude of maximum meridional heat transport (Bingham and Hughes 2008), which is a quantity being highly indicative of climate variability. Moreover, there exist hydrographic observations close to 26.5°N that span several decades (Bryden et al. 2005), permitting comparison between the variability detected by the RAPID array and an existing record.

The RAPID array has yielded important insights of the AMOC from 2004 to present (Srokosz and Bryden 2015). Yet, the observational record is limited in temporal length and to a single latitude. This restricts our insights of longer-timescale AMOC variability and meridional coherence of the overturning (Jackson et al. 2016). However, new monitoring systems are under way (see Ansorge et al. 2014, Lozier et al. 2017) that will expand in-situ measurements of the overturning to the RAPID's neighbouring basins.

2.5 Fingerprints of the AMOC

In lieu of longer direct observations of the AMOC, identifying fingerprints of the overturning represent an alternative that can help reveal valuable information. A fingerprint (also referred to as a proxy) is an indirect measurement that approximates or represents a phenomenon in the absence of a direct measurement of a variable, and it must be a quantity that can be derived from both observations and climate models (Mahajan et al. 2011). Establishing fingerprints of the AMOC are important, because: i) they can act as a tool to reconstruct past AMOC variations when no direct observations of the circulation are available, ii) they supplement on-going monitoring of AMOC by helping in interpreting the circulation's variability and change, and iii) they improve assessment of future AMOC impacts on the wider climate system (Mahajan et al. 2011). Thus, by establishing AMOC fingerprints, the overturning is connected to richly observed variables that can help in the interpretation of the AMOC's behaviour.

Promising AMOC fingerprints include sea surface temperatures (Latif et al. 2006, Roberts et al. 2013, Rahmstorf et al. 2015, Caesar et al. 2018), density in the Atlantic mid-ocean (Roberts et al. 2013), sea surface height from satellite altimetry (Hakkinen 2001, Lorbacher et

al. 2010, Ivchenko et al. 2011) and tide gauges (Bingham and Hughes 2009, Sallenger et al. 2012, Yin and Goddard 2013). Below I highlight some of the most recent developments in research aimed at establishing SST as an important fingerprint of the AMOC; however, sea level as an AMOC proxy is the focus for the remaining chapters of the dissertation.

Several studies have examined the extent to which Atlantic sea surface temperatures (SSTs) can be used to infer the AMOC's relative strength and variability (e.g. Latif et al. 2006, Kamykowski 2010, Rahmstorf et al. 2015). A dipole of interhemispheric sea surface temperatures, which implies seesaw changes in SSTs between the Northern and Southern Hemisphere, has been connected to AMOC variations (Latif et al. 2006, Keenlyside et al. 2008, Muir and Fedorov 2015). This Atlantic SST dipole is detected on multidecadal and longer timescales (e.g. Latif et al. 2004, Latif et al. 2006) and is distinguishable from the interannual to decadal tri-polar pattern detected in the North Atlantic (Visbeck et al. 1998).

The SST dipole is also in line with the observed signature of the Atlantic Multidecadal Variability (AMV) between the Hemispheres. Studies have applied this dipole as an index to examine changes in the AMOC, suggesting that SST can act as an AMOC proxy (Latif et al. 2004, 2006, Kamykowski 2010). Recently, a distinct region of cooling in the northern Atlantic was linked to a declining AMOC over the 1900s, particularly after 1970, whereby freshening of the North Atlantic and regional reduction in density of the surface ocean were pointed out as important factors of the weakening (Rahmstorf et al. 2015).

Notwithstanding, the Atlantic SST dipole and SST-derived AMOC proxies have been subject to criticism. One argument concerns that SST variations in the North Atlantic are disconnected from the South Atlantic (Houghton and Tourre 1992, Enfield et al. 1999). Particularly, observations indicate that the AMV SST signature is substantially larger in the Northern Hemisphere compared to the Southern counterpart (Sutton and Hodson 2005). Another is that a dipole SST index might be plagued by the bias of a large gradient in aerosol forcing between the hemispheres (Rahmstorf et al. 2015) and that North Atlantic SST might be more driven by aerosol forcing than internally generated AMOC variability (Booth et al. 2012). The opposing arguments on the reliability of SST as an indicator of AMOC variability (see Ottera et al. 2010, Roberts et al. 2013, Ortega et al. 2017) support the need for examining other AMOC proxies.

2.6 The relationship between AMOC and sea level

Using coastal sea level (CSL) data in detecting climatic changes in the ocean circulation is especially intriguing given how it renders the prospect of relatively low-cost methods of

monitoring and the fact that tide gauge records provide over century-long data records (Huthnance 2004, Ezer 2015). Several studies have sought a connection between AMOC and North American east coast (NAEC) sea level variations, whereby the utility of sea level-based AMOC "fingerprints" have been highlighted (Zhang 2008, Bingham and Hughes 2009, Yin and Goddard 2013, Ezer 2013, 2015, Frajka-Williams 2015, McCarthy et al. 2015, Little et al. 2017).

2.6.1 Spatial and temporal characteristics

Observations show that sea level rise (SLR) along the North American east coast north of Cape Hatteras (~35°N) has been accelerating at a rate 3-4 times faster than the global average (Boon 2012) over the past decades (~1975) (Ezer and Corlett 2012, Sallenger et al. 2012). The stretch from Cape Hatteras (35.1°N) to Cape Cod (41.7°N) has been labelled a "hotspot of accelerated sea level rise" (Sallenger et al. 2012). Several studies suggest that this SLR hotspot is a dynamic feedback to climatic changes in the overturning (Levermann et al. 2005, Yin and Goddard 2013) and a weakening of the AMOC, and its upper flank, the Gulf Stream (GS) (Smeed et al. 2014, Ezer 2015, Rahmstorf et al. 2015, Srokosz and Bryden 2015).

Although the processes involved in a link between large-scale ocean dynamics and CSL are complex (Ezer 2015), a strong inverse connection between AMOC strength and sea level variability along the U.S. northeastern coast has been found on various timescales; from days to weeks (Ezer and Atkinson 2014, Ezer 2016), to interannual (e.g. Bingham and Hughes 2009, Goddard et al. 2015), decadal (e.g. Hakkinen 2001, Ezer 1999, 2001, McCarthy et al. 2015) and multidecadal (e.g. Kopp 2013, Ezer 2013, Little et al. 2017) timescales. Correspondingly, some studies have advocated the utility of coastal dynamic sea levels along the North American northeast coast as an important "fingerprint" of the AMOC, with tide gauges and sea surface height altimetry being the primary diagnostic data (Zhang 2008, Bingham and Hughes 2009, Yin and Goddard 2013, Ezer 2013, 2015, Frajka-Williams 2015, McCarthy et al. 2015, Little et al. 2017).

Distinct estimates have been derived for the AMOC-CSL connection (Ezer 2001, Bingham and Hughes 2009, Yin et al. 2009, Levermann et al. 2005, Howard et al. 2014, Park and Sweet 2015). For instance, Bingham and Hughes (2009) obtain that a 2 cm drop in sea level along the US northeast coast correspond to an increase of 1 Sv in the AMOC. The linear ~2cm/Sv relationship is found in the ocean model OCCAM (eddy-permitting) and supported by data from satellite altimetry and tide gauge records (Bingham and Hughes 2009). Also Woodworth et al. (2014) and Levermann et al. (2005) find linear AMOC-CSL relationships, with magnitudes of 1.5 cm Sv^{-1} and 5 cm Sv^{-1} respectively. Recently, Little et al. (2019)

highlight that scaling coefficients of the relationship generally range between -1 to -2 Sv cm^{-1} in models. Although these estimates are not directly comparable, they give an idea of the nature of the negative AMOC-sea level relationship. Not to mention, these estimates may only apply to specific timescales. For example, Bingham and Hughes (2009) underline that the ~2 cm Sv^{-1} relation may not apply on other timescales beyond interannual variability.

2.6.2 Mechanism underlying the AMOC-sea level connection

An oceanographic theory of why the AMOC, and its upper branch, the Gulf Stream (GS), can impact sea level variability along the North American east coast on various timescales is rooted in the geostrophic balance and the associated sharp sea level gradient across the Gulf Stream (Kopp, 2013, Ezer 2015, McCarthy et al. 2015). Particularly, sea level is tilted across the Stream with lower sea levels on the GS's onshore side compared to its offshore side, with a difference of ~1-1.5 m over a ~100 km distance (Ezer 2016). This tilt is controlled by the speed of the Gulf Stream and changes in the GS's path and strength will therefore affect the sea level gradient across the Gulf Stream. Therefore a decline in the Gulf Stream or North Atlantic Current will weaken offshore sea level gradients and cause an increase in sea level along the North American east coast (Ezer and Atkinson 2014, Kopp 2013). As a result, the sea level difference between the North American east coast (onshore) and Bermuda (offshore) has been used as an approach for detecting changes in the Gulf Stream (e.g. Ezer 1999, 2001, 2015, Surges and Hong 2001).

Moreover, applying an ocean GCM over the period 1985-2004, Bingham and Hughes (2009) establish that coastal sea level changes between 40°N to 50°N along the North American east coast are anticorrelated with changes in northward upper layer AMOC volume transport at 50°N in the North Atlantic on interannual timescales. This inverse relationship is described in terms of geostrophic balance, zonally integrated across the basin. Particularly, the AMOC transport and sea level along the western North Atlantic boundary are in anti-phase if the eastern boundary condition is insignificant and western boundary CSL changes with bottom pressure on the shelf and slope, while ignoring intervening topography (Bingham and Hughes 2008). Particularly, Bingham and Hughes (2008) suggest that north of the Gulf Stream (~ 42°N), the pressure on the eastern Atlantic boundary can be ignored so that the meridional transport within a particular depth interval [$z_1 \leq z \leq z_2$] is approximated by (Bingham and Hughes 2009):

$$T \approx -\frac{1}{p_0 f_0} \int_{z_2}^{z_1} p_w dz,$$

where p_0 is the mean density of ocean water, f_0 is the Coriolis parameter and p_w is the bottom pressure anomaly on the western boundary. Bingham and Hughes (2009) find that interannual AMOC variability is well captured by bottom pressure on the western Atlantic boundary. Because the western boundary bottom pressure is closely associated with sea level along the U.S. northeast coast, the authors conclude sea level can act as an AMOC proxy on interannual timescales.

2.6.3 Cape Hatteras and alongshore sea level gradient

Along the North American east coast sea level gradually descends ~0.6 m from Florida (~ 27°N) to Maine (~ 45°N). This drop in sea level is largely due to the fact that the oceans near the coast north of Cape Hatteras consist of cold, dense and fresh subpolar water, which substantially reduces the steric height (Yin and Goddard 2013, McCarthy et al. 2015). On the other hand, south of Cape Hatteras the ocean is characterised by warm, salty and rather light water masses with subtropical origin, which cause higher coastal dynamic sea level (DSL) (Yin and Goddard 2013). Together with the general northward gradient, the coastal DSL is particularly high just around Cape Hatteras (~35°N) because of a convergence of the southward Slope Current and the northward Gulf Stream (Yin and Goddard 2013). Consequently, the alongshore DSL gradient is especially strong north of 35°N. Sea level behaviour on either side of Cape Hatteras (CH) is found to be highly correlated and alike, on timescales of years to decades (Thompson 1986, Yin et al. 2009, Sallenger et al.2012, Ezer 2013, Andres et al. 2013, Bingham and Hughes 2009, McCarthy et al. 2015, Goddard et al. 2015). Therefore, it is thought that an alongshore DSL gradient could be highly effective in representing the AMOC (McCarthy et al. 2015).

2.6.4 The AMOC strength and the Gulf Stream path

Although the path of the Gulf Stream (GS) has been demonstrated to be tightly connected to AMOC strength (Joyce and Zhang 2010), there is conflicting evidence on the nature of the relationship (Zhang et al. 2011). Some modelling analyses suggest that a stronger outflow of the North Atlantic Deep Water, and therefore a stronger AMOC, are associated with a strengthening of the cyclonic Northern Recirculation Gyre and a southward shift of the GS path (Döscher et al. 1994, Zhang 2008, Yeager and Jochum 2009, Zhang et al. 2011). These modelling results are in agreement with the Line W moored array observations off the U.S. east coast (Joyce and Zhang 2010). However, ocean hindcast models have demonstrated the opposite; a stronger North Atlantic Deep Water is related to a stronger AMOC and a northward shift of the GS path (de Coetlogon et al. 2006).

Observational data, especially the RAPID (2004-) and Oleander (1993-) arrays, have also presented varying results on the AMOC-Gulf Stream link. It is found that the Gulf Stream component of the Oleander data (Rossby and Gottlieb 1998) is not correlated with the AMOC in the RAPID data (Ezer 2015). At the same time, Rossby et al. (2014) found no significant declining trend in the Oleander's Gulf Stream that is in agreement with the declining of the AMOC and Gulf Stream seen in other data (Ezer et al. 2013, Smeed et al. 2014). It has been proposed that the disagreement between the Oleander's Gulf Stream and AMOC observations can be rooted in local dynamics, where a single Oleander line is influenced by eddies and meandering, not total AMOC transport changes (Rossby et al. 2010, Ezer 2015). Combined with modelling results, these observations underline that there may not be a one-to-one relationship between the AMOC strength and the Gulf Stream path. Caution should therefore be exercised when analysing the relationship between sea level, the AMOC, and/or the Gulf Stream.

2.7 Summary

Changes in the AMOC could have major impacts on multiple aspects of the regional Atlantic and global climate system. Climate models widely predict that the AMOC will weaken over the 21st century in response to elevated atmospheric greenhouse gases (GHGs). Yet, state-of-the-art models exhibit a rather large spread in their simulations of the amplitude and frequency of AMOC variability and there is low confidence in evaluating the circulation beyond 2100. March 2019 marked 15-years of unique continuous basin-wide measurements of the AMOC's strength and vertical structure at 26.5°N by the RAPID monitoring system. However, the observational record is still too short to adequately evaluate the AMOC. While longer in-situ measurements are pending, the use of coastal sea level and tide gauge data in detecting climatic changes in the AMOC is of special interest given how it renders the prospect of relatively low-cost monitoring and over century-long data respectively. However, we still need to determine the robustness of Atlantic coastal sea level (CSL)-based AMOC "fingerprints". It is the goal of this project to do just so on interannual and decadal timescales.

3 Data and Methods

3.1 CMIP5

This project uses climate model simulations from the World Climate Research programme's (WCRP) Coupled Model Intercomparison Project Phase 5 (CMIP5; Taylor et al. 2012) provided by the Program for Climate Model Diagnosis and Intercomparison (PCMDI, https://pcmdi.llnl.gov/mips/cmip5/). CMIP5 coordinates experiments of past and future climate change and variability and is a cornerstone in the IPCC's Fifth Assessment Report (AR5) (Taylor et al. 2012).

The CMIP5 suite of experiments includes historical simulations covering the period 1850 to 2005 and projections based on representative concentration pathways (RCPs). The historical simulations include all recognised climate forcings agents (Slangen et al. 2015), and include changes in total solar irradiance and observed changes in atmospheric composition that reflect both anthropogenic (e.g. greenhouse gases and human-made aerosols) and natural sources (e.g. solar forcing, volcanic impacts, aerosols) (Taylor et al. 2012). For the first time, the CMIP5 historical runs also include time-evolving land cover (ibid.). Each RCP is labelled based on the expected watts per square meter that each forcing scenario would produce by 2100: +2.6, +4.5, +6.0 and +8.5 watts per square meter (Wm^{-2}) (van Vuuren et al. 2011, Thomson et al. 2011, Masui et al. 2011, Riahi et al. 2011). Essentially, Wm^{-2} measures how much heat energy that is being trapped by the climate system, whereby each RCP indicates the change in radiative forcing at the tropopause by 2100 compared to preindustrial levels (Hayhoe et al. 2017). Extended concentration pathways (ECPs; with the same labelling as for the RCPs) are used to extend some projections to the year 2300.

Although the CMIP5 experiments cover the period of 1850-2300, the focus of this project is on 1920 onwards as this time period better reflects the temporal coverage of the tide gauge records considered in this study. 42 CMIP5 models are analysed for the historical sea level runs and up to 48 models for the historical AMOC data. The models are selected on the basis that a single model must provide output from both the AMOC and SSH fields, thus allowing for comparison. The exception is that a few more models are included when analysing the AMOC in isolation in *Chapter 4.2* (up to 48 compared to 42 for SSH). For future 21st-23rd century projections, the RCP2.6 and RCP8.5 forcing scenarios are used with corresponding ECPs. The number of models available under the future scenarios is limited and includes 25 model runs under RCP2.6 and 35 for RCP8.5 for the period 2006-2100, and 8 model runs for RCP2.6 and 6 for RCP8.5 for the period 2100-2300. *Table S1* in the Appendix provides a list

of model names, number of model ensembles, type of grid spacing, horizontal resolution for the ocean realm, vertical levels, model components and run lengths.

The number of ensembles per model varies across fields in historical simulations. Together there are 168 ensemble members in the analysis for the historical SSH runs and 42 ensemble members for the historical AMOC runs. For the historical AMOC data there is only one realisation (r1i1p1) per model. For SSH, a majority of models have two or more ensemble members, and for these models almost all ensembles differ with respect to initial states (i.e. they are different realisations), and the realisations available per model are averaged to obtain a single model output. Particularly, there are 12 models that exhibit the r1i1p1 ensemble only and 30 models that exhibit 2 or more ensemble members for the historical SSH data. 12 models exhibit 5 or more ensemble members, with 5 models having 10 or more ensemble members (CNRM-CM5(15), CSIRO-Mk3-6-0(16), EC-EARTH(17), GFDL-CM2p1(21), GISS-E2-R(26)). Any potential differences in output due to the selection of different number of realisations across fields are here regarded as less important than the goal of maximising model output. For future simulations, the r1i1p1 realisation only is used for both the AMOC and SSH fields.

However, it should be highlighted that the varying number of ensemble members used for the historical SSH runs in comparison with r1i1p1 only for the AMOC runs may distort the AMOC-CSL relationship. To test for this, a preliminary analysis was performed in which the absolute value of AMOC-CSL correlation coefficients for the models with two or more ensembles (*Figure 5.1*) were subtracted from the r1i1p1 ensemble only for the respective models. The preliminary analysis indicates no substantial intra-model variation in such a way as to alter the overall conclusion of this study's prevailing AMOC-CSL correlation analysis (*Figure 5.1*). In fact, a large majority of models appear not particularly sensitive to the number of ensemble members in affecting correlation output.

Particularly, out of the 30 models whose ensemble mean consists of 2 or more realisations, 23 (17) CMIP5 models obtain a difference in correlation value of <0.2 on interannual (decadal) timescales when averaging the coastal sites latitudinally. For example, CanESM2(5), consisting of 5 realisations, obtains a difference in correlation of 0.0943. Similarly, CCSM4(6), with 6 realisations, obtains a difference of 0.0028, and FGOALS-s2(19), with 3 realisations, obtains a difference of 0.0503. Even smaller variations are achieved by certain models if considering a single latitude. For instance, at New York (~40.7N) CNRM-CM5(15) obtains a correlation difference of 0.0330, compared to 0.1518 when averaging across all coastal sites. Yet, a small selection of models demonstrates large variations in correlation

results. This especially concerns CSIRO-Mk3-6-0(16), GFDL-CM2p1(21), GISS-E2-R(26), IPSL-CM5A-MR(30), NorESM1-M(42), obtaining a difference in correlation values of >0.35.

Importantly, since the large majority of models with 2 or more realisations obtain a difference in correlation result of <0.2 when compared to r1i1p1 only, the initial result (*Figure 5.1*), that about half (one-fourth) of the models on decadal (interannual) timescales generate moderate to strong anticorrelations (<-0.5) of the AMOC-CSL relationship, is maintained to a large degree. Analysing r1i1p1 only for both historical AMOC and SSH simulations results in some additional models obtaining stronger anticorrelations, which is especially the case for the models that exhibit 10 or more ensembles. Thus, the overall difference of considering r1i1p1 only for both AMOC and SSH is a small increase in inter-model agreement, supportive of stronger inverse AMOC-CSL relationships.

The historical simulations are compared to both tide gauges along the coast and AMOC in-situ observations at 26.5°N. When comparing simulations of AMOC with RAPID observations, the historical simulations are extended up to 2016 using the RCP2.6 scenario (Van vuuren et al. 2011). Over this relatively short extended period, the choice of scenario for extension is not decisive as the scenarios only start to diverge in the second half of the 21st century. For all AMOC and SSH model outputs the time mean, linear trend and seasonal cycle are removed, and a suitable boxcar filter (moving-window average) applied. The focus is on interannual and decadal variability, and 13-month and 121-month boxcar filters are applied accordingly. The seasonal cycle was removed by first calculating the average of all January months, February months, and so on until December, and then subtracting the cumulative January average from each single January month, the cumulative February average from each single February month, and so on until the December months.

The 50 CMIP5 models have varying horizontal resolution in the ocean, ranging from 1.98° to 0.28° by longitude and from 1.25° to 0.20° by latitude (see *Table 3.1*). Seven models have a resolution of 1.13° (longitude) x 0.47° (latitude). The CMCC and IPSL model families exhibit the lowest horizontal resolution (1.98°x1.21°). MIROC4h has the highest horizontal resolution of 0.28° (longitude) x 0.20° (latitude); this model is also eddy-permitting. The models have a horizontal grid system that is either irregular or distorted. A majority of the models have distorted grids (32 out of 42 models). The CMIP5 models also vary with respect to vertical resolution, ranging from 20 to 70 levels in the ocean. Most models are on z-level grids, but some are run with hybrid/isopycnal or sigma-coordinate grids.

Model	Code	Integral Period (historical)	Grid spacing	Horizontal resolution	Vertical levels
ACCESS1-0 (*1)	1	1850-2005	D	~1.00 x 0.60	50
ACCESS1-3 (*2)	2	1850-2005	D	~1.00 x 0.60	50
bcc-csm1-1 (*3)	3	1850-2012	D	~1.00 x 0.78	40
bcc-csm1-1-m **(*4)**	4	1850-2012	D	~1.00 x 0.78	40
BNU-ESM	5	1850-2005	R	~1.00 x 0.90	50
CanCM4	6	1961-2005	R	~1.41 x 0.94	40
CanESM2 **(*5)**	7	1850-2005	R	~1.41 x 0.94	40
CCSM4 **(*6)**	8	1850-2005	D	~1.13 x 0.47	60
CESM1-BGC **(*7)**	9	1850-2005	D	~1.13 x 0.47	60
CESM1-CAM5-1-FV2	10	1850-2005	D	~1.13 x 0.47	60
CESM1-CAM5 **(*8)**	11	1850-2005	D	~1.13 x 0.47	60
CESM1-FASTCHEM **(*9)**	12	1850-2005	D	~1.13 x 0.47	60
CESM1-WACCM **(*10)**	13	1850-2005	D	~1.13 x 0.47	60
CMCC-CESM **(*11)**	14	1850-2005	D	~1.98 x 1.21	31
CMCC-CM **(*12)**	15	1850-2005	D	~1.98 x 1.21	31
CMCC-CMS **(*13)**	16	1850-2005	D	~1.98 x 1.21	31
CNRM-CM5-2 **(*14)**	17	1850-2005	D	~0.99 x 0.62	42
CNRM-CM5 **(*15)**	18	1850-2005	D	~0.99 x 0.62	42
CSIRO-Mk3-6-0 **(*16)**	19	1850-2005	R	~1.88 x 0.95	31
EC-EARTH **(*17)**	20	1850-2005	D	~0.99 x 0.62	42
FGOALS-g2 **(*18)**	21	1850-2005	R	~1.00 x 0.92	30
FGOALS-s2 **(*19)**	22	1850-2005	R	~1.00 x 0.92	30
FIO-ESM **(*20)**	23	1850-2005	D	~1.13 x 0.47	40
GFDL-CM2p1 **(*21)**	24	1861-2040	D	~1.00 x 0.90	50
GFDL-CM3 **(*22)**	25	1860-2005	D	~1.00 x 0.90	50
GFDL-ESM2G **(*23)**	26	1861-2005	D	~1.00 x 0.86	50
GFDL-ESM2M **(*24)**	27	1861-2005	D	~1.00 x 0.86	50
GISS-E2-H-CC	28	1850-2010	R	~1.00 x 1.00	33
GISS-E2-H	29	1850-2005	R	~1.00 x 1.00	33
GISS-E2-R-CC **(*25)**	30	1850-2010	R	~1.25 x 1.00	32
GISS-E2-R **(*26)**	31	1850-2005	R	~1.25 x 1.00	32
HadCM3	32	1859-2005	R	~1.25 x 1.25	20
HadGEM2-AO	33	1860-2005	R	~1.00 x 0.83	40
HadGEM2-CC **(*27)**	34	1859-2005	R	~1.00 x 0.83	40
HadGEM2-ES **(*28)**	35	1859-2005	R	~1.00 x 0.83	40
inmcm4	36	1850-2005	D	~1.00 x 0.53	40
IPSL-CM5A-LR **(*29)**	37	1850-2005	D	~1.98 x 1.21	31
IPSL-CM5A-MR **(*30)**	38	1850-2005	D	~1.98 x 1.21	31
IPSL-CM5B-LR **(*31)**	39	1850-2005	D	~1.98 x 1.21	31
MIROC4h **(*32)**	40	1850-2005	D	~0.28 x 0.20	48
MIROC5 **(*33)**	41	1850-2012	D	~1.41 x 0.80	50
MIROC-ESM-CHEM **(*34)**	42	1850-2005	R	~1.41 x 0.94	44
MIROC-ESM **(*35)**	43	1850-2005	R	~1.41 x 0.94	44
MPI-ESM-LR **(*36)**	44	1850-2005	D	~1.41 x 0.82	40
MPI-ESM-MR **(*37)**	45	1850-2005	D	~0.45 x 0.45	40
MPI-ESM-P **(*38)**	46	1850-2005	D	~1.41 x 0.82	40
MRI-CGCM3 **(*39)**	47	1850-2005	D	~1.00 x 0.49	51
MRI-ESM1 **(*40)**	48	1851-2005	D	~1.00 x 0.49	51
NorESM1-ME **(*41)**	49	1850-2005	D	~1.13 x 0.47	70
NorESM1-M **(*42)**	50	1850-2005	D	~1.13 x 0.47	70

Table 3.1. Summary of the integral period, grid spacing and spatial and vertical resolution (ocean only) for the CMIP5 models used in this study. *indicates the respective model (1-42) examined in the

AMOC-sea level relationship in *Chapter 5* and SSH-tide gauge comparison in *Chapter 4.3*. If not numbered 1-42, the models are given by their model names throughout the study. *Italics* indicate models with no data available for AMOC analysis. For irregular grids the horizontal resolution is an approximate (nominal resolution).

3.1.1 CMIP5 sea level

The CMIP5 monthly output variable "zos" (i.e. sea surface height above the geoid, here denoted as η and referred to as dynamic sea level, sea surface height or modelled sea level interchangeably) is used to obtain regional changes in dynamic sea level (DSL). The CMIP5 models exhibit varying configurations (Flato et al. 2013). In a majority of CMIP5 models the ocean module is based on the Boussinseq approximation and therefore conserves volume instead of mass (Greatbatch 1994, Griffies and Greatbatch 2012). While non-Boussinesq models integrate global steric effects contributing to sea level changes, sea surface height (SSH) in Boussinesq models do not (Greatbatch 1994). The models having a mass-conserving non-Boussinesq scheme are NorESM1-M, NorESM1-ME, GISS-E2-R, GISS-E2-R-CC. However, the global ocean mean values are removed from the *zos* fields and changes in global mean sea level are not considered in this study. Thus, sea level variability from the Boussinesq and non-Boussinesq CMIP5 models are directly comparable (Losch et al. 2004).

Ocean variables in CMIP5 models are subject to residual "drift" because of inadequate spin-up of the control runs or non-closure of the energy budget (Sen Gupta et al. 2013, Hobbs et al. 2016). These spurious trends can be removed from the forced runs (Yin et al. 2010, Yin 2012). In the present study, however, the historical runs are not subject to a specific drift correction because much of the drift is mapped into the global mean sea level, which is removed from the *zos* field. In addition, all data has been linearly detrended, which is a statistical operation that has potential overlapping functions with drift correction by removing features thought to distort the relationships of interest. It is also important to underline that the non-specific correction is not equivalent to treating the climate drift as inconsequential *prima facie.*

Coastal DSL in 42 CMIP5 models are assessed at 38 (native) grid points closest to the North American east coast between 25°N (~Key West) and 48°N (~Rimouski), corresponding to the locations of relevant tide gauges in the PSMSL database (*Table 3.2*).

3.1.2 Calculating the AMOC in the CMIP5 models

In climate models, the AMOC index is often defined as the maximum meridional overturning streamfunction in a zonal band, selected at a particular latitude (e.g. 30°N) or along a latitudinal stretch (e.g. north of 30°N), measured in Sverdrup (1 Sv = 10^6 m^3 s^{-1}) (Medhaug

and Furevik 2011, Buckley and Marshall 2015). To limit the influence of surface Ekman transport, another criterion is often that the maximum streamfunction should be positioned at depths greater than 500 m. Instead of using the ocean meridional overturning mass streamfunction variable ("msftmyz", in kg s^{-1}) provided directly by the modelling centres, this study obtains the AMOC strength determined in depth coordinates by integrating velocities with depth and along the section from the western boundary (x_{west}) to the eastern boundary (x_{east}) where the transport streamfunction is (e.g. Zhang and Wang 2013, Frajka-Williams et al. 2019):

$$\Psi(z,y,t) = \int_{z}^{0} \int_{x_{west}}^{x_{east}} v(x,y,z',t)dxdz',$$

where *v(x,y,x,t)* is the meridional velocity, *y* is latitude, *z* is depth and *z'* is the dummy vertical coordinate satisfying $0 \leq z' \leq z$. To obtain the full meridional transport, the *uo* (seawater x velocity) and *vo* (seawater y velocity) CMIP5 products were used in the process of integrating along zonal paths, forming arcs on non-Cartesian grids.

The strength of the overturning (AMOC) is defined as the maximum of the overturning streamfunction (Ψ):

$$\text{AMOC} = \max(\Psi(z,y))$$

Based on the streamfunction variable, indices of the AMOC strength are computed by selecting the maximum in the vertical for a given latitude. Here, the AMOC index is defined as the maximum of the zonally integrated overturning streamfunction in the Atlantic between the equator and 70°N and below 500 m of depth.

3.2 Sea level observations

To study observed sea level variations I use monthly mean revised local reference (RLR) sea level records obtained from the Permanent Service for Mean Sea Level (Holgate et al. 2013, PSMSL 2018; www.psmsl.org) for tide gauges (TGs) stretching from Key West, Florida to Rimouski, Canada (locations 38 to 1, *Table 3.2*). The TG records are selected based on the criterion that they cover at least 25 years with 75 per cent completeness or more. The records are detrended. In addition, the time mean and seasonal cycle are removed from each record, and 13-month and 121-month boxcar filters are applied for interannual and decadal variability analysis respectively. In all comparisons between models and observations detrending is always performed over the same time periods to ensure that only the same frequencies of

variability are retained for comparison. By removing the linear trend from each tide gauge record and restricting the focus to interannual and decadal timescales, a majority of the global mean steric sea level component is also removed (Kopp 2013, Piecuch 2016).

Number	Station name	ID (PSMSL)	Latitude	Longitude	Temporal length	Completeness (%)
1	RIMOUSKI *	1597	48.48	-68.52	1984-2016	92
2	PORT-AUX-BASQUES *	392	47.57	-59.13	1959-2016	89
3	NORTH SYDNEY *	1299	46.22	-60.25	1970-2016	97
4	EASTPORT *	332	44.90	-66.98	1930-2017	93
5	HALIFAX *	96	44.67	-63.58	1920-2014	97
6	PORTLAND *	183	43.66	-70.25	1920-2017	99
7	BOSTON **	235	42.35	-71.05	1921-2017	99
8	PROVIDENCE **	430	41.81	-71.4	1938-2017	85
9	WOODS HOLE **	367	41.52	-70.67	1932-2017	94
10	NEWPORT **	351	41.51	-71.33	1930-2017	99
11	NEW LONDON **	429	41.36	-72.09	1938-2017	96
12	NANTUCKET ISLAND **	1111	41.29	-70.1	1965-2017	97
13	BRIDGEPOINT **	1068	41.17	-73.18	1965-2017	96
14	MONTAUK **	519	41.05	-71.96	1948-2017	92
15	WILLETS POINT	362	40.79	-73.78	1931-2000	97
16	NEW YORK (THE BATTERY) **	12	40.70	-74.01	1920-2017	99
17	SANDY HOOK **	366	40.47	-74.01	1933-2017	98
18	PHILADELPHIA **	135	39.93	-75.14	1920-2017	96
19	ATLANTIC CITY	180	39.36	-74.42	1920-2017	92
20	BALTIMORE **	148	39.27	-76.58	1920-2017	99
21	ANNAPOLIS **	311	38.98	-76.48	1928-2017	96
22	CAPE MAY	1153	38.97	-74.96	1966-2017	91
23	WASHINGTON DC **	360	38.87	-77.02	1931-2017	98
24	LEWES **	224	38.78	-75.12	1920-2017	75
25	CAMBRIDGE II	1295	38.57	-76.07	1971-2017	97
26	SOLOMON'S ISLAND **	412	38.32	-76.45	1938-2017	96
27	GLOUCESTER POINT	597	37.25	-76.5	1950-2003	92
28	KIPTOPEKE BEACH **	636	37.17	-75.99	1951-2017	99
29	SEWELLS POINT **	299	36.95	-79.33	1927-2017	99
30	PORTSMOUTH	399	36.82	-76.29	1935-1987	99
31	WILMINGTON	396	34.23	-77.95	1935-2017	98
32	SRINGMAID PIER	1444	33.66	-78.92	1977-2016	79
33	CHARLESTON I	234	32.78	-79.93	1921-2017	98
34	FORT PULASKI	395	32.03	-80.9	1935-2017	98
35	FERNANDINA BEACH	112	30.67	-81.47	1920-2017	82
36	MAYPORT	316	30.39	-81.43	1928-2001	99
37	MIAMI BEACH	363	25.77	-80.13	1931-1981	93
38	KEY WEST	188	24.56	-81.81	1920-2017	99

Table 3.2. Overview of the PSMSL tide gauge stations used in this study. *tide gauge stations corresponding to the "northeast composite" in Goddard et al. 2015. **tide gauge sites corresponding to the "Northeast Hotspot" (NEH) in Sallenger et al. 2012.

3.2.1 The Inverted Barometer correction

The sea surface is affected by a pressure force exerted by atmospheric loading. Since the compressibility of the ocean is small, the spatiotemporal variations in atmospheric pressure are offset by changes in sea level heights, thereby its name inverse barometer (IB) effect (Ponte 1992, Wunsch and Stammer 1997). Correcting for the IB effect could be important given that the effect of atmospheric pressure loading has been shown to explain approximately 25 per cent of the interannual sea level variance along the North American northeast coast (Piecuch 2016).

The PSMSL tide gauge records are corrected for this IB effect. To estimate the IB response (η_{ib}), I apply monthly sea level pressure (P_a) from the Hadley Centre Sea Level pressure data (HadSLP2) (Allan and Ansell 2006). The use of the HadSLP2 P_a data is in accordance with PSMSL's recommendation (Holgate et al. 2013). To estimate the IB effect the criteria for hydrostatic balance is used:

$$\frac{dp}{dz} = p_w g,$$

where p_w is the density of water and g the standard gravitational acceleration (g=980.6 cm/s^2). Assuming that the ocean response to the changes in atmospheric pressure is in isostatic equilibrium, the sea level height corrections η_{ib} from the IB effects is then given by:

$$\eta_{ib}(cm) = -\frac{1}{p_w g}(p_0 - \bar{p}),$$

where p_0 is the atmospheric pressure at sea level (obtained from HadSLP2r) and $\bar{p}$ is the global mean atmospheric pressure at sea level ($\bar{p}$ is 1013.25 mbar for the standard atmosphere). Thus, to a close approximation, an increase (decrease) in pressure by 1 mbar is accompanied by a decrease (increase) of approximately 1 cm in sea level.

3.3 AMOC observations

For the in-situ observations of the AMOC at 26.5°N I use data from the RAPID Climate Change and Meridional Overturning Circulation and Heat Transport Array (MOCHA) and Western Boundary Time Series programme (RAPID/MOCHA/WBTS). The data was downloaded from http://www.rapid.ac.uk/rapidmoc/ on the 5th of November 2016. I use the

AMOC transport and AMOC streamfunction time series covering the period 2nd April 2004 to 11th October 2015. Similar to the CMIP5 data and the tide gauge records, the linear trend, time mean and seasonal cycle are removed from the RAPID data, and a 13-month boxcar filter is applied. Given that the RAPID record barely exceeds a single decade, the modelled versus observed AMOC comparison concerns interannual variability only.

3.4 Deriving relationships between the AMOC and sea level

Two approaches are used to derive relationships between the AMOC and sea level variability along the North American east coast. First, the direct relationship between simulated AMOC and SSH for 42 CMIP5 models are examined. Here, standard correlation techniques are applied with the aim to highlight the distinct models' AMOC-SSH relationship strength at particular latitudes along the U.S. east coast. The AMOC is then reconstructed by using the slope from a linear regression model relating simulated SSH variability along the North American east coast to simulated AMOC strength. Comparing the slope-based AMOC reconstruction with the initial AMOC simulations should give an indication of the extent to which SSH can act as an AMOC proxy. Furthermore, the Taylor skill score is used to assess the skill of the SSH-based AMOC reconstructions in mimicking the AMOC simulations for the distinct CMIP5 model.

The Taylor skill score (Taylor 2001) takes into account three attributes; variance, correlation and perfect correlation, and ranges between 0 (least skilful) and 1 (perfect score). As the correlation approaches perfect correlation, and the model variance approaches the observed variance, the skill approaches 1. Likewise, the more negative the correlation is, and the closer the model variance goes towards zero or infinity, the more the skill decreases towards zero.

Second, the sea level gradient along the east coast of North America is assessed in order to diagnose the spatial sea level patterns and their relation to the AMOC. Based on the alongshore sea level gradient, a circulation index is derived. The SSH-based AMOC index is inspired by McCarthy et al. (2015) and based on using sea level estimates along the North American east coast, north and south of Cape Hatteras, instead of an onshore-offshore sea level difference, such as Bermuda (Ezer 2013). By doing the former, the goal is to avoid that spatially coherent ocean transport signals are disrupted by eddies (Wunsch 2008, Kanzow et al. 2009).

I estimate an ocean circulation index based on composites of tide gauge coordinates in modelled SSH data along the North American Atlantic coast. Since Cape Hatteras characterise the boundary between the subtropical and subpolar gyres along the U.S. east

coast (McCarthy et al. 2015), I can compose two single composites that represent the subtropical and the subpolar circulation respectively, by averaging sea level data south (TG sites/grid points 31-38 in this study) and north (TG sites/grid points 7-30 in this study, see *Table 3.2*) of Cape Hatteras. The AMOC index is then derived by subtracting the averaged-based northern composite from the southern composite. In contrast to McCarthy et al. (2015), this study establishes a SSH-based AMOC index based on simulated coastal sea level data, not on tide gauges, to test the applicability of the index in CMIP5. *Figure 3.1* shows the ocean circulation index derived from PSMSL tide gauge data.

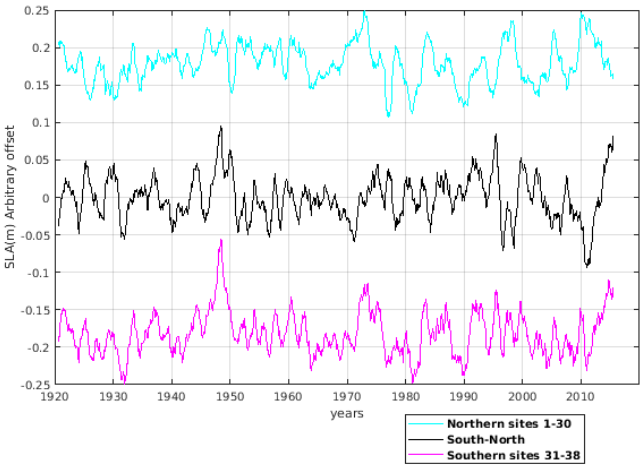

Figure 3.1. Dynamic sea level anomalies north (*turquoise*) and south (*pink*) of Cape Hatteras derived from PSMSL tide gauge records, and the difference in sea level (southern minus northern average, *black*), where the latter defines the sea level composite-based index for the ocean circulation. 1920-2016. Interannual variability.

3.5 Metrics for CMIP5 model assessment

Routine metrics are calculated to evaluate the CMIP5 models' performance in representing the AMOC and SSH, including correlation and dispersion. Spatial correlation maps are also computed in order to identify the spatial patterns of DSL variations along the North American Atlantic coast, and to reveal if this study's result is in agreement with the "north east hotspot" found in other recent studies and the distinct divide in sea level variations and coastal dynamics near 35°N (e.g. Sallenger et al. 2012, Yin and Goddard 2013, Goddard et al.2015).

4 Model-data inter-comparison

4.1 Introduction

While much attention has been given to the weakening of the AMOC transports in coupled climate and ocean models in response to global warming and high-latitude freshening (Cheng et al. 2013, Kirtman et al. 2013, Collins et al. 2013, Reintges et al. 2016), some basic characteristics of the AMOC variability in coupled models, including its magnitude and meridional coherence, need to be more fully established. Besides, few studies have evaluated the AMOC in more than 40 CMIP5 models. To the best of my knowledge, Xu et al. (2019) is the study having examined the AMOC across the largest number of CMIP5 model simulations (44 models). In comparison, Sgubin et al. (2017) studied the AMOC in 40 models, Cheng et al. (2013) studied 10 CMIP5 models, Reintges et al. (2016) examined approximately 30 models and Heuze et al. (2017) assessed 23 models. Below I examine the AMOC's mean state, vertical profile, temporal variability and spatial characteristics in up to 48 models (*Section 4.2.1*) as well as compare historical AMOC simulations with the RAPID observations in 42 models (*Section 4.2.2*).

In the second part of this chapter I evaluate the CMIP5 models' ability to reproduce observed sea level variability along the eastern North American coast over the twentieth century (*Section 4.3*). I use long-term tide gauge data from the Permanent Service for Mean Sea Level (PSMSL). The reasons why simulated SSH is evaluated against available tide gauge observations, are three-fold. First I want to identify general patterns of model behaviour and outliers. Revealing consistent model biases and performance patterns are important steps in bolstering our understanding of inadequate model physics, parameterisations and resolution. Do some models perform much better compared to others when analysed against observations? If so, why?

Second, I want to diagnose to what extent simulated SSH mimic observations in such a way as to support the relevance of sea level-based AMOC proxies. If many models simulate the observations of both SSH and AMOC well, and simulations show a strong AMOC-SSH relationship, this would add credibility to tide gauge-based "fingerprints". Third, greater insights are needed on how well simulations match tide gauge observations on interannual and decadal timescales in particular, as these are the frequency bands at which the AMOC-sea level relation is the most debated in models (see e.g. Woodworth et al. 2014 and Little et al. 2017).

4.2 The AMOC in CMIP5 models

4.2.1 General characterisations

The mean North Atlantic overturning streamfunctions averaged from 1850 to 2005 in 48 CMIP5 models are displayed in *Figure 4.1.* A large majority of the models comprises a distinct upper and lower overturning cell. While almost all of the models exhibit a maximum northward transport near 1000 m depth, the exact latitudinal location of the maximum and the magnitude of the transport strength vary more, especially with respect to the magnitude. Approximately two-thirds (~33 models) demonstrate a maximum northward transport near 1000 m and 40°N (between 35° and 45°N). Among these models there is an inter-model spread in the maximum of the northward transport from ~12 to 30 Sv. The remaining one-third typically shows their maximum south of 35°N or their maximum is not easily detectable due to a discontinuous streamfunction (which is an artefact of the general computational procedure used to calculate the AMOC for all models).

The models demonstrating the strongest maximum northward transport near 1000m and 40°N are BNU-ESM, CESM1-BGC, FGOALS-g2, MPI-ESM-LR, MPI-ESM-P, NorESM1-ME and NorESM1-M, all having transport strength values between ~26 and 30 Sv (*Figure 4.1*). GISS-E2-H exhibit a strength of 30 Sv, but has no easily detectable maximum at ~40°N due to discontinuous streamfunction. At 26.5°N, mean values across the 48 models transport strength range between 3 and 32 Sv. About one-third (~16 models) exhibits a maximum value of the streamfunction in the range between 16 and 20 Sv near 1000 m and 40°N. Compared to the conventional mean AMOC structure, with a strong northward flow in the upper ~1000 m and a slower southward flow at depth (Talley et al. 2003), IPSL-CM5B-LR deviates from this. In particular, IPSL-CM5B-LR exhibits a very weak overturning circulation and hence no clear streamfunction (*Figure 4.1)*. However, IPSL-CM5B-LR still exhibits some variability due to other processes, as indicated by the northward transport anomalies in *Figure 4.2*.

Approximately three-quarters of the models generate a distinct lower North Atlantic Deep Water (LDW) between ~3000 and 5000 m depth, with peak values ranging from ~ -2 to -6 Sv (*Figure 4.1*). A majority of these models obtain a LDW mean value between -4 Sv and -6 Sv. In comparison, the RAPID array produced a LDW mean value during 2004-2016 of -5.9 Sv (Smeed et al. 2018). The MPI-ESM model family as well as MIROC5 and GFDL-ESM2G have the strongest negative LDW peak values, peaking at ~ -10 Sv. Generally, the models having a distinct lower cell coincide with the models having a strong northward flowing cell.

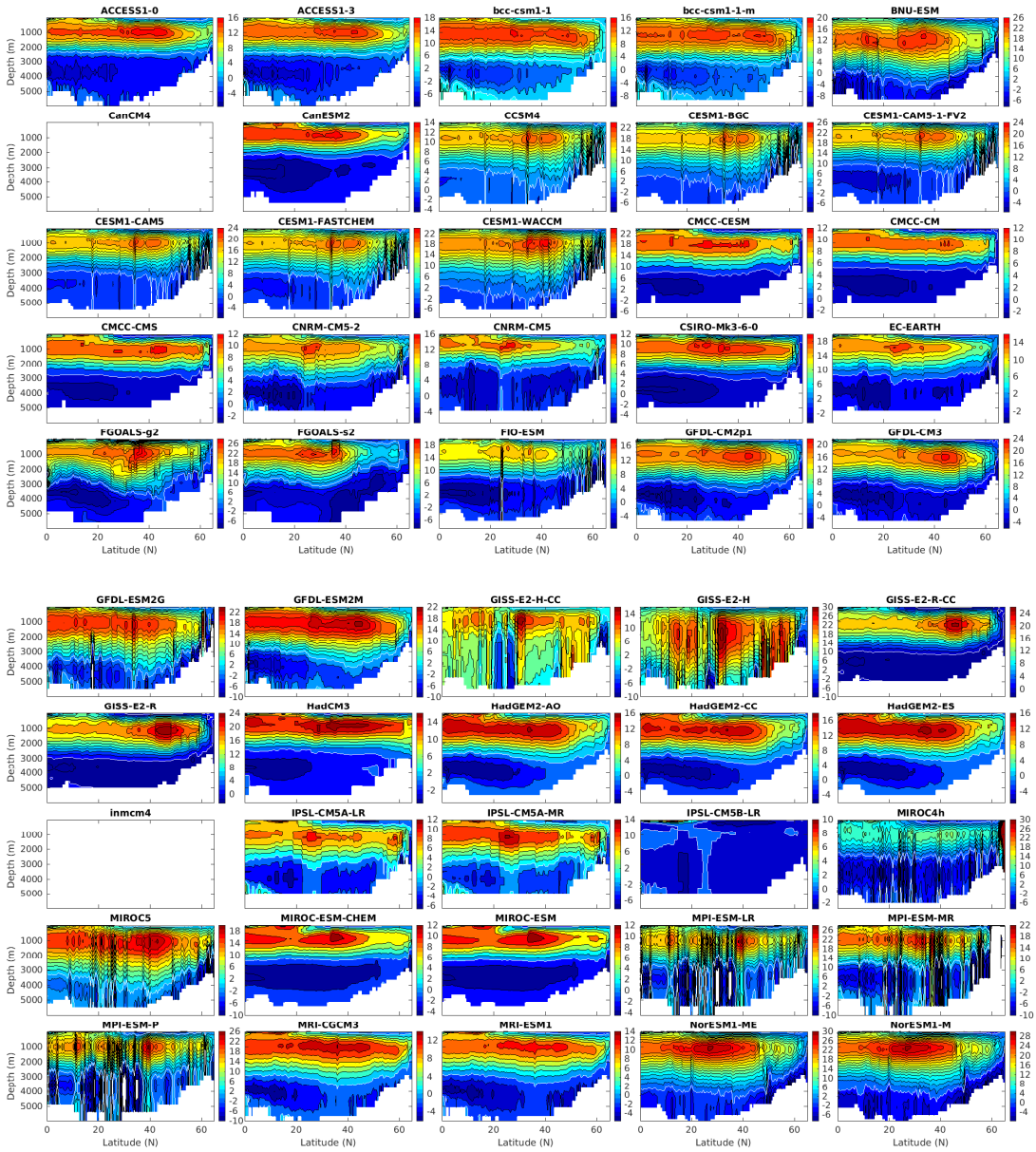

Figure 4.1. Time-averaged overturning streamfunction as a function of latitude and depth from historical (1850-2005) simulations of 48 CMIP5 models. Note that the scale (colour bar) of the streamfunction is not constant but changes across models. Units: Sverdrup (1 Sv = 10^6 m^3 s^{-1}).

Because almost all models demonstrate a close to constant depth of 1000 m of the streamfunction maximum, I characterise the AMOC as the total northward transport between 100 m and 1000 m. It follows that the Ekman transport, defined as the flow in the upper 100 m (Chereskin and Roemmich 1991:869), is not accounted for, which reflects the wind forcing component of meridional coherence. Given this characterisation of the AMOC, the temporal and latitudinal structures of the AMOC from 48 CMIP5 models are revealed in *Figures 4.2,* displaying the northward transport anomaly as a function of time and latitude.

There is a notable CMIP5 model spread in the spatiotemporal AMOC behaviour, both with respect to the dominant mode of variability and the spatial structure (*Figure 4.2*). While some models generate a strong decadal mode of variability (e.g. bcc-csm1-1-m, GFDL-CM2p1, GFDL-CM3, FGOALS-s2, MPI-ESM-LR), other models produce weaker decadal-like variability patterns or are dominated by interannual or higher frequencies signals (e.g. FIO-ESM, GISS-E2-H, IPSL-CM5A-LR). A majority of the models exhibit a decadal mode of variability with amplitudes ranging between 1.5 Sv to 2 Sv along short or long latitudinal stretches. Although the largest amplitudes, peaking at 2 Sv, tend to occur north of 40°N for some models, there is no absolute consistency in this. Rather, many models tend to have a strong signal at decadal frequency along most of the latitudinal stretch (0° to 65°N), especially north of 20°N. South of 20°N, interannual or higher frequency signals prevail. This latitudinal inconsistency stands in contrast to the clear decadal mode north of 40°N found in HadCM3 and OCCAM models in Bingham et al. (2007), with higher frequency signals found south of this latitude.

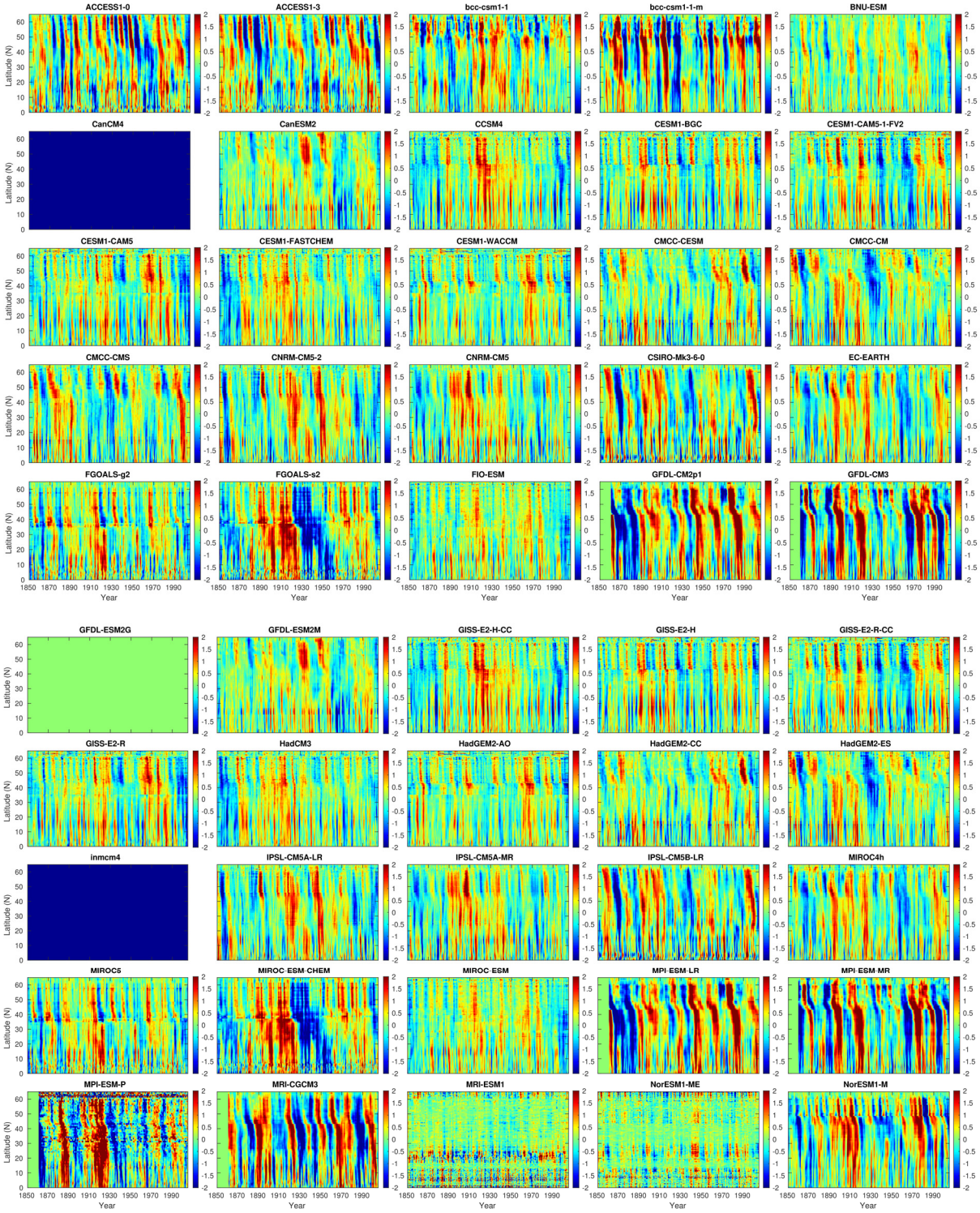

Figure 4.2. The northward transport anomaly between 100 m and 1000 m as a function of time (1850 - 2005) and latitude in 47 CMIP5 models. The time mean and linear trends are removed. Units: Sverdrup (1 Sv = 10^6 m^3 s^{-1}).

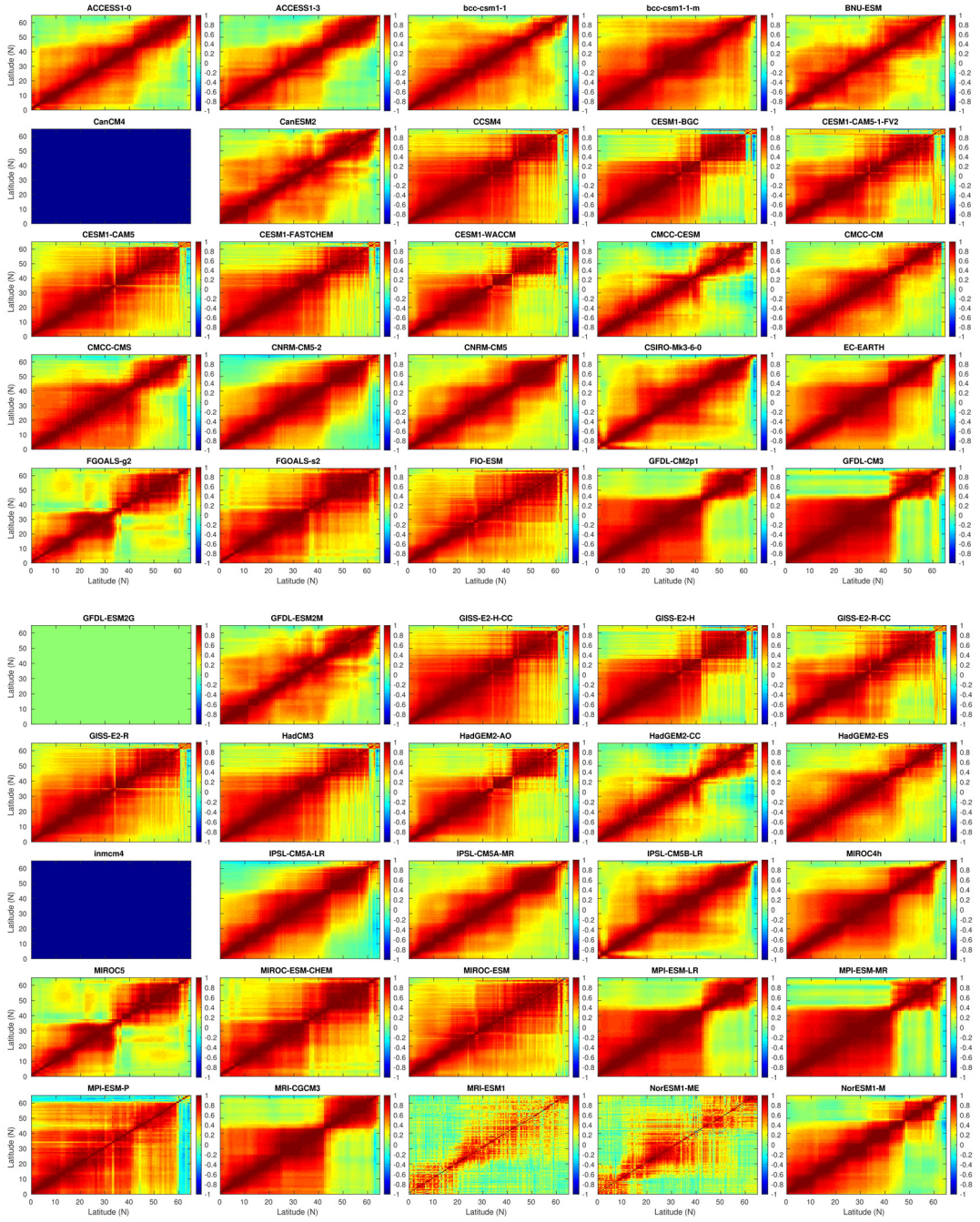

Figure 4.3. Cross-correlation arrays from upper layer 100-1000 m interannual transport. The figures show the degree to which interannual AMOC variations are correlated between latitudes (0° to 65°N).

Particularly, about three quarters of the 47 models display a clear, strong decadal mode of AMOC variability (*Figure 4.2*). Some of these models also demonstrate a noticeable multidecadal mode of variability (FGOALS-s2, GFDL-CM2p1, MIROC-ESM-CHEM, MPI-ESM-LR and NorESM-M). The remaining models typically generate a weak decadal mode or interannual variability patterns. Among the models showing decadal signals, some demonstrate stronger (e.g. GFDL-CM2p1, GFDL-CM3 and MPI-ESM-LR) decadal frequency signals than others (e.g. FIO-ESM, MIROC-ESM and MRI-ESM1).

There are substantial model-to-model differences concerning the spatiotemporal pattern (*Figure 4.2*). For example, GFDL-CM2p1, GFDL-CM3, MPI-ESM-LR, MPI-ESM-MR and MRI-CGCM3 show a decadal mode of variability with a decrease in the earlier years followed by a shift from a low to high AMOC transport regime in the 1890s, then again a low regime followed by a new high regime in the 1910s, and from here a decadal shift between high and low regimes. All of these models also show tendency of a southward "tilt" of decadal signals from high to low latitudes near 40°N. FGOALS-s2 and MIROC-ESM-CHEM show the same spatiotemporal transport pattern with a strong positive AMOC phase between ~1880 and 1920 and a strong negative phase between ~1920 and 1960, followed then by a new positive phase until late 1990s.

Decadal variability south of 40°N is lagging the variability north of 40°N in the following models: GFDL-CM2p1, GFDL-CM3, MIROC-ESM-CHEM, MRI-CGCM3, MPI-ESM-MR and MPI-ESM-LR. Generally, for about half of the models it appears that a signature of decadal AMOC variability is present along the entire North Atlantic basin, while interannual variations are less meridionally coherent and often locally confined. Other models' spatial pattern is rather inconsistent, with no distinct meridional coherence (e.g. GFDL-ESM2M, CanESM2 and BNU-ESM).

From the viewpoint of climate regulation, high-frequency variability of the AMOC is not important. Next, I therefore focus on interannual and decadal variability by removing the mean seasonal cycle and applying a low-pass (boxcar) filter of 13-month and 121-month length respectively. Modelling studies have suggested that rapidly propagating coastally trapped waves play a central role in communicating changes in the rate of deep water formation at high latitudes to lower latitudes (e.g. Kawase 1987, Johnson and Marshall 2002, Roussenov et al. 2007). Because these waves, by being transitioned into a slower flow, make sure to balance the supply of water masses to high latitudes with the rate of deep water formation, it is an intrinsic assumption that AMOC variability should be meridionally coherent even on short time-scales (Bingham and Hughes 2008). Nevertheless, Bingham et al.

(2007) demonstrated that interannual variability of the AMOC at a single latitude, being zonally integrated across the Atlantic basin, is not necessarily representative of the variability at other latitudes, therefore challenging the meridional coherence.

The extent to which interannual AMOC variations are correlated between latitudes (0° to 65°N) is displayed in *Figure 4.3*. About half of the models (~23 models) demonstrate a distinct divide in correlations near 40°N; while latitudes south of 40°N are well correlated with each other, they are not strongly correlated with latitudes north of this latitude and vice versa. All these models, with the exception of three (GISS-E2-H, MRI-CGCM3, NorESM1-M), have a z-coordinate vertical system. A majority of these models also have relatively high resolution. CMCC-CMS, GFDL-CM2p1, GFDL-CM3, MPI-ESM-LR, MPI-ESM-MR and MRI-CGCM3 stand out particularly strongly in terms of showing a clear change in correlation values near 40°N. Such a distinct change in interannual variability patterns at 40°N was also found in HadGEM3 and OCCAM in Bingham et al. (2007).

The remaining half either demonstrates a less clear divide in correlations near 40°N (e.g. EC-EARTH and HadGEM2-CC), relatively strong correlations for most of the latitudinal stretch with no distinct change in correlations near 40°N (e.g. GISS-E2-R, MPI-ESM-P), or a divide in correlations closer to 30°N (e.g. MIROC5). Some models also generate three areas of strong correlations, typically with at divide near 20°N and 40°N (e.g. CNRM-CM5-2, IPSL-CM5A-LR and IPSL-CM5A-MR). Moreover, MPI-ESM1 and NorESM1-ME show a diffuse, scattered correlation pattern.

There is no absolute consistency in model formulation and resolution for the models showing a clear distinction between variability north and south of 40°N (*Figure 4.3*). Although the models with the strongest differences north and south of 40°N tend to be among the highest resolution models and have a z-coordinate system, there are still some models with higher resolution and z-levels that do not show this distinct change at 40°N. Rather, these models show meridional coherence of interannual AMOC variability with strong correlations for almost the entire latitudinal stretch (e.g.CESM1-CAM5, bcc-csm1-1-m).

Because the lack of meridionally coherent AMOC changes does not exclusively occur in the models with the highest resolution, it is also difficult to conclude anything on the extent to which the intergyre boundary, which is better defined in high resolution models, may play a role in creating the differences north and south of 40°N, as previously noted by Bingham et al. (2007). In general, it is unclear what may be the underlying reason for the inter-model spread with regards to the meridional coherence of interannual variability or lack thereof. However, since about half of the models show latitudinal dependence, especially north and

south of 40°N, any claim of a widely meridional coherent AMOC should yet be treated with caution (see Bingham et al. 2007, Zhang 2010, Wang et al. 2019).

4.2.2 Comparison against observations

In this section I compare the RAPID observations with simulated AMOC at 26.5°N. Due to the still short RAPID record (2004 to 2015), only interannual timescales are analysed. From April 2004 to October 2015 the mean observed AMOC strength was 17.3 Sv (1 Sv = 10^6 m^3 s^{-1}), as derived from unfiltered RAPID data (*Figure 4.4*). Although the majority of the CMIP5 models exhibit AMOC strength relatively close to RAPID observations, only ten models obtain strength ranging between 16 and 18 Sv. There is a total inter-model spread from ~3 Sv (IPSL-CM5B-LR) to ~ 30 Sv (NorESM1-ME), in which half of the models obtain a mean strength ranging between ~14 to 20 Sv. CCSM4(6), CESM1-FASTCHEM(9), GFDL-ESM2G(23), GISS-E2-R-CC(25) and GISS-E2-R(26) almost accurately replicate the AMOC strength of the RAPID array (17.3 ± 0.3 Sv). Four model families (ACCESS1, CESM1, GFDL, except GFDL-CM2p1, and MPI) obtain mean AMOC strength values quite close to the RAPID 2004-2015 mean (~17.3 ±2 Sv).

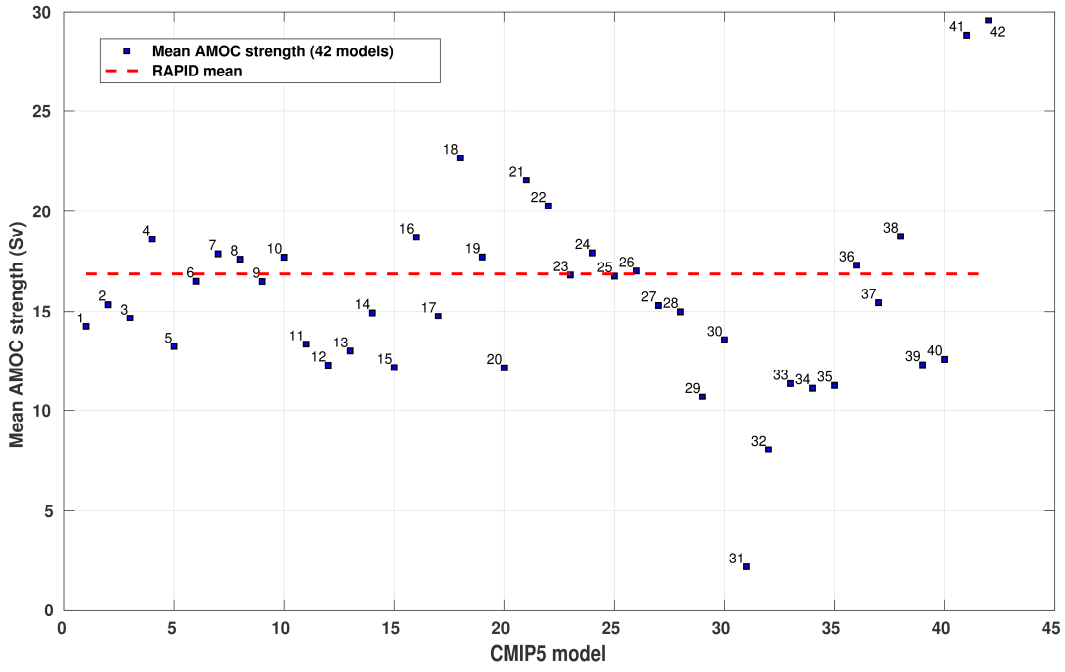

Figure 4.4. Mean AMOC strength (in Sverdrup) for simulated AMOC variability from 42 CMIP5 models and RAPID array at 26.5°N during 2004-2016. Historical simulations 2004-2006 with RCP8.5 as an extension 2006-2015. Data is not detrended, the seasonal cycle is not removed and there is no boxcar filter.

The CMIP5 models (with a mean standard deviation of ~0.71 Sv for 42 models) typically underestimate the amplitude of interannual AMOC variability in the RAPID data (~1.3 Sv

standard deviation) (*Figure 4.5*). Yet, GFDL-ESM2M(24) and MPI-ESM-MR(37) most accurately replicate the RAPID amplitude, with ~1.29 Sv and ~1.2 Sv standard deviation respectively. A majority of the models obtain a standard deviation ranging between 0.4 and 0.8 Sv. CESM1-FASTCHEM(9) and GFDL-CM2p1(21) have amplitudes farthest from the RAPID array, with ~0.27 Sv and ~0.32 Sv standard deviations respectively.

Within a single model family, there is no major performance differences, with the exception of GFDL-ESM2M which perform much better in terms of replicating the amplitude of the RAPID data (~1.3 Sv standard deviations) compared to its other model family members, which obtain values around ~0.7 Sv standard deviations.

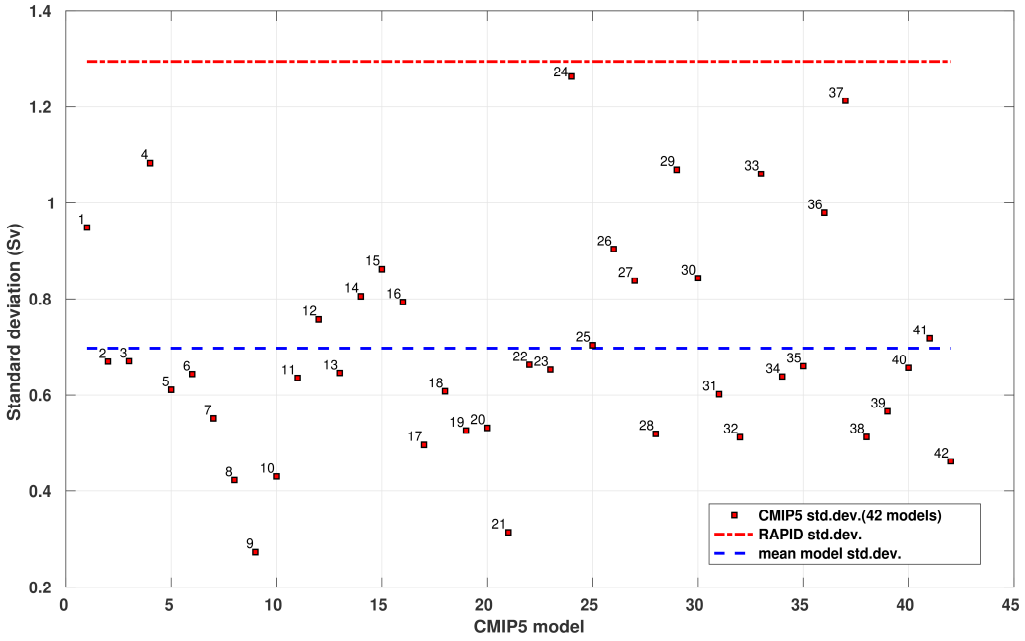

Figure 4.5. Standard deviation (in Sverdrup) for simulated interannual AMOC variability from 42 CMIP5 models and RAPID array at 26.5°N for period 2004-2016. Historical simulations 2004-2006 with RCP8.5 as an extension 2006-2015. The linear trend and seasonal cycle are removed and a 13-month boxcar filter is applied.

The RAPID data at 26.5°N shows a declining trend of ~ -0.265 Sv/yr over the 12-year period of 2004-2015 (Yan et al. 2018). The CMIP5 models generally underestimate the observed RAPID trend magnitude, as indicated by the multi-model ensemble mean estimated at ~ 0.082 Sv/yr and by the mean 12-year trend magnitude for the individual models (*Figure 4.6*). All models, except three (GFDL-CM2p1(24), GFDL-CM3(25), GFDL-ESM2M(27)), underestimate the RAPID trend magnitude if taking into account the standard deviation of the 12-year trend magnitudes. The majority of models (37 models) obtain trends magnitudes between 0.05 and 0.1 Sv/yr. Most CMIP5 models exhibit a relatively small spread in the 12-year trend magnitudes, with all, except three CMIP5 models (GFDL-CM2p1(24),

GFDL-CM3(25), GFDL-ESM2M(27)), generating a range that do not cover the observed trend magnitude. Moreover, the larger the deviation from the mean of all models, the larger the standard deviation of the 12-year magnitudes. This suggests that although the CMIP5 models generally underestimate the RAPID trend magnitude, the simulated trend magnitudes for the entire historical run do not deviate largely.

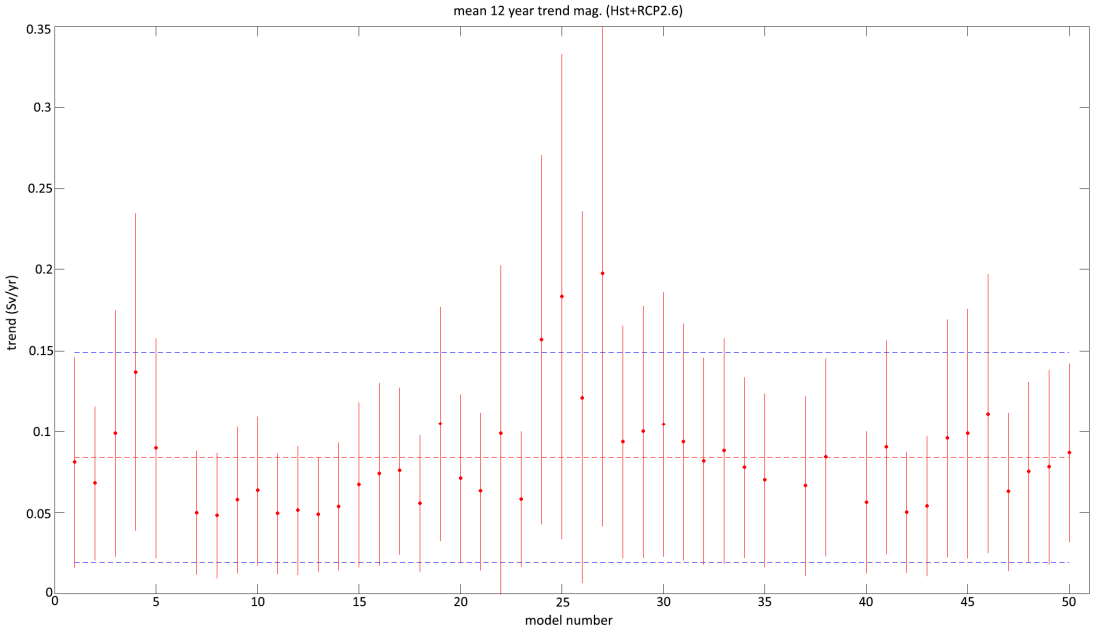

Figure 4.6. 12-year AMOC (in Sverdrup) trend magnitudes in the CMIP5 models. For each model, the red points show the mean 12-year trend magnitude, where trends are computed in a moving 12-year window over the full length of the historical run, extended, where available, with RCP2.6. Vertical bars represent plus/minus 1 standard deviation of the 12-year trend magnitudes. The red dashed line represents the multi-model mean (47 models) of the mean 12-year trend magnitudes for individual models. The blue dashed lines represent the multi-model mean of the mean 12-year trend magnitudes plus (upper) or minus (lower) 1 standard deviation. Note that the AMOC trend magnitudes are given in absolute values.

4.3 Assessment of coastal sea level in the CMIP5 models

4.3.1 Ability to represent temporal variability

I examine the variance of PSMSL tide gauges and simulated SSH from 42 models for 38 locations along the North American east coast. Results show that close to all the 42 CMIP5 models underestimate the tide gauge variance along the coast on both interannual (40 out of 42 models) and decadal timescales (38 out of 42 models) (*Figure 4.7*). The discrepancy between average model variance and tide gauge variance is larger for interannual (~4 cm^2 versus 10 cm^2) versus decadal variability (~1 cm^2 versus 2 cm^2).

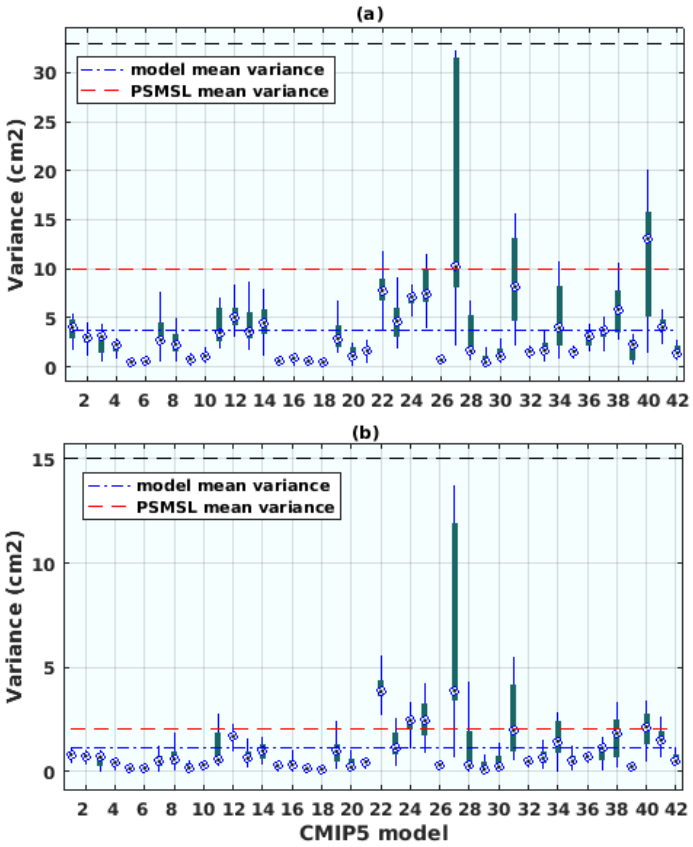

Figure 4.7. Variance distributed spatially by model for simulated SSH from 42 CMIP5 models and 38 PSMSL tide gauge locations along the U.S. east coast. Historical simulations 1920-2006. Boxplot showing variance per model (horizontal) for 38 loctions (vertically). (a) interannual variability with 13-month boxcar filter. (b) decadal variability with 121-month boxcar filter. Model mean variance (blue line) and PSMSL tide gauge mean variance (red line). Median (blue dots), 25-75th percentiles (dark green box), 9-91st percentiles (blue vertical line) and outlier maximum (black upper horzontal line). PSMSL data is corrected for the inverse barometer effect.

On interannual timescales, the majority of models show small spatial distribution in variance as well as a large underestimation of the tide gauge variance. Most models obtain a spatial median between ~ 0.05 cm^2 and 4 cm^2 (*Figure 4.7a*). Several models produce remarkably uniform variance spatially (e.g. CanESM2(5), CCSM4(6), CESM1-FASTCHEM(9), CESM1-WACCAM(10), CNRM-CM5(15), CSIRO-Mk3-6-0(16), EC-EARTH(17), FGOALS-g2(18), GISS-E2-R(26) and MIROC-ESM(35)). Yet, a few models generate a substantially large spatial spread in variance (e.g HadGEM2-CC(27), IPSL-CM5B-LR(31), MIROC-ESM-CHEM(34) and MRI-ESM1(40)). Furthermore it is important to note the particularly large spread in variance and large median (~10 cm^2) for HadGEM2-CC(27). Whilst MRI-ESM1(40) produces a larger spatial median (~14 cm^2) than any other model, its spatial spread is not close to HadGEM2-CC(27)'s on interannual timescales.

Similar patterns can be noted for decadal variability (*Figure 4.7b*), even though there are smaller differences in model behaviour on this timescale by magnitude. A large majority of the models display a median variance between ~0.04 cm^2 and 2 cm^2 as well as close to uniform variance spatially. The variance of the multi-model mean average is ~1 cm^2, which is an underestimation of the mean tide gauge variance estimated at ~2 cm^2. The models showing larger spread in varance along the coast compared to the majority of the models are CMCC-CESM(11), GFDL-CM3(22), GFDL-ESM2G(23), GFDL-ESM2M(24), GISS-E2-R-CC(25), HadGEM2-CC(27). HadGEM2-ES(28), IPSL-CM5B-LR(31), MPI-ESM-P(38) and MRI-ESM1(40). The most deviating behaviour is found in HadGEM2-CC(27) which shows a larger latitudinal spread in variance compared to the rest of the models on both interannual and decadal timescales. IPSL-CM5B-LR(31) also demonstrates large spread in variance along the coast, but does not match HadGEM2-CC(27)'s outlying behaviour. Interestingly, MRI-ESM1(40) does not exhibit particular outlying behaviour on decadal timescales, as it does on interannual timescales.

If assessing the sea level variance distribution across the 42 models for a single tide gauge location (*Figure 4.8*) instead of for each single model (*Figure 4.7*), interesting model performance characteristics are revealed. For interannual variability (*Figure 4.8a*) the 42 CMIP5 models exhibit a divide in variance at approximately 40°N (location 18), close to Philidelphia. If including both the 25^{th} to 75^{th} and 9^{th} to 91^{st} percentiles, there is larger model disagreement in variance north of ~40°N, while greater model agreement south of this latitude. Put differently, the CMIP5 models seem to agree less (more) in their simulations of the amplitude of coastal SSH variability north (south) of ~40°N. The exception of this is for a few locations north of ~44°N (location 6), which show larger spread in variance between models. Simultanously, the underestimation of the tide gauge variance is generally larger south of ~35.1°N compared to the region north of this latitude. For locations north of 35.1°N, the median model variance is larger than for the locations south of this point, above and under 2 cm^2 respectively.

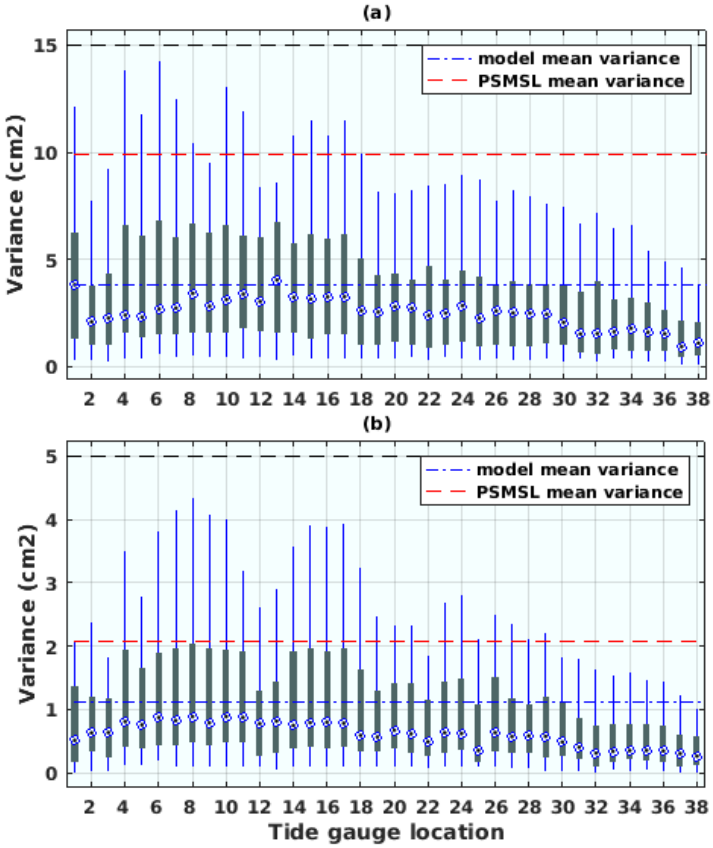

Figure 4.8. Variance distribution across models by location for simulated SSH from 42 CMIP5 models and 38 PSMSL tide gauge locations along the U.S. east coast. Historical simulations 1920-2006. Boxplot showing variance per location (horizontal) for all 42 CMIP5 models (vertically computed). (a) interannual variability with 13-month boxcar filter. (b) decadal variability with 121-month boxcar filter. Model mean variance (blue line) and PSMSL tide gauge mean variance (red line). Median (blue dots), 25-75th percentiles (dark green box), 9-91st percentiles (blue vertical line) and outlier maximum (black upper horzontal line).

Much of the same pattern is shown for decadal variability (*Figure 4.8b*). The models generally tend to underestimate the tide gauge variance and they disagree more on the SSH variance north of ~40°N (location 18) while agree more south of this location. At the same time, the 42 CMIP5 models generally have a stronger median variance north compared to the south of Cape Hatteras. Yet, if considering the 25th to 75th and 9th to 91st percentiles of models, there is less model disagreement for the locations just north of ~45°N (location 4) and for a few locations around 41°N (location 12-13) compared to the other locations north of 40°N. Also on decadal timescales, the CMIP5 models' underestimation of the tide gauge variance is generally larger south of ~35.1°N compared to north of this latitude.

Yet, it should be noted that *Figures 4.7 and 4.8* only display the average value of the tide gauge variance for the 38 stations along the North American east coast. In fact, the variance for the PSMSL stations varies with latitude from 3.9 cm^2 (station 5, ~44.7°N) to 20.5 cm^2 (station 32, ~33.7°N) on interannual timescales and from ~0.8 cm^2 (station 1, ~48.5°N) to

~8.9 cm^2 (station 32, ~33.7°N) on decadal timescales. There is also a noticeable change in variance on either side adjacent to Cape Hatteras, especially between location 30 (~36.8°N) and 32 (~33.7°N), where the variance drops from ~20.5 (~8.9) cm^2 at site 32 to ~9.4 (~1.0) cm^2 at site 30 on interannual (decadal) timescales. One possible reason for this is that tide gauge 32 (Springmaid Pier) is only covering 39 years (1977-2016) with 79 % completeness, implying that this record is subject to substantial uncertainty due to the extent of missing values and short continuous data. Nevertheless, it has already been established in literature (e.g. Ezer 2013, Yin and Goddard 2013) that there exists a difference in coastal sea level variability near these latitudes of Cape Hatteras (35.1°N), and thus the variance differences detected in the tide gauge records may also be reflective of this region's physical dynamics. Importantly, although the PSMSL variance changes along the coast latitudinally, the majority of CMIP5 models still underestimate the variance at a majority of tide gauge locations. Particularly, 20 out of 38 tide gauge sites exhibit variance of >10 cm^2 (>2 cm^2) on interannual (decadal) timescales, by which the majority of models obtain variance values lower than ~10 cm^2 (~2 cm^2) on interannual (decadal) timescales.

4.3.2 Ability to represent spatial patterns

Previous work (e.g. Sallenger et al. 2012, Ezer et al. 2013, Yin and Goddard 2013, McCarthy et al. 2015, Ezer 2015, Goddard et al. 2015) has highlighted that tide gauge data and different ocean and general circulation models have indicated a clear divide in sea level regimes on either side of Cape Hatteras (~35.1°N), whereby different dynamics may drive these sea level regimes (Yin and Goddard 2013, Ezer 2016). Do the 42 CMIP5 models exhibit any distinct divide in spatial coherence in interannual and decadal SSH variability along the North American east coast? How do the models compare to the observed spatial sea level pattern by tide gauges?

Figure 4.9 shows the spatial cross-correlation for the 38 PSMSL tide gauges in relation to one another along the eastern coast of North America for the 1920-2006 period. On interannual timescales it is clear that the tide gauges exhibit a distinct divide at Cape Hatteras (*Figure 4.9a*). The sea level regimes north and south of Cape Hatteras (~location 31, 35.1°N) are highly correlated and alike. A highly coherent sea level regime north of Cape Hatteras that stretches between Cape Hatteras (~location 31, 35.1°N) and Cape Cod, near Boston (~location 7, 42.4°N), is in agreement with previous studies (e.g. Sallenger et al. 2012, Ezer 2013, McCarthy et al. 2015).

The PSMSL tide gauge records do not, however, show such a clear spatial pattern on decadal timescales (*Figure 4.9b*). Although a weak pattern and divide can be detected at Cape

Hatteras on decadal timescales, it is far from as distinct as the regime-divide shown for interannual variability.

It should be noted that tide gauge sites 30 (Portsmouth, ~36.8°N) and 32 (Springmaid Pier, ~33.7°N) in *Figure 4.9* show deviating behaviour, obtaining no clear positive cross-correlation values. One possible reason for this is that both tide gauge records are subject to relatively short observational records. While site 32 covers the period 1977-2016 (39 years), site 30 covers 1987-1935 (52 years), which make these tide gauge among the temporally shortest included in this study. In addition, tide gauge site 32 is subject to a substantial number of missing values, obtaining only 79% completeness. This decreases this record's ability to capture some important interannual-to-decadal fluctuations. Moreover, site 30 is located in the Elisabeth River several miles (10-15 miles) from the open Atlantic Ocean, thereby possibly distorting large-scale dynamics. Together, these factors may alter the cross-correlation result at these sites.

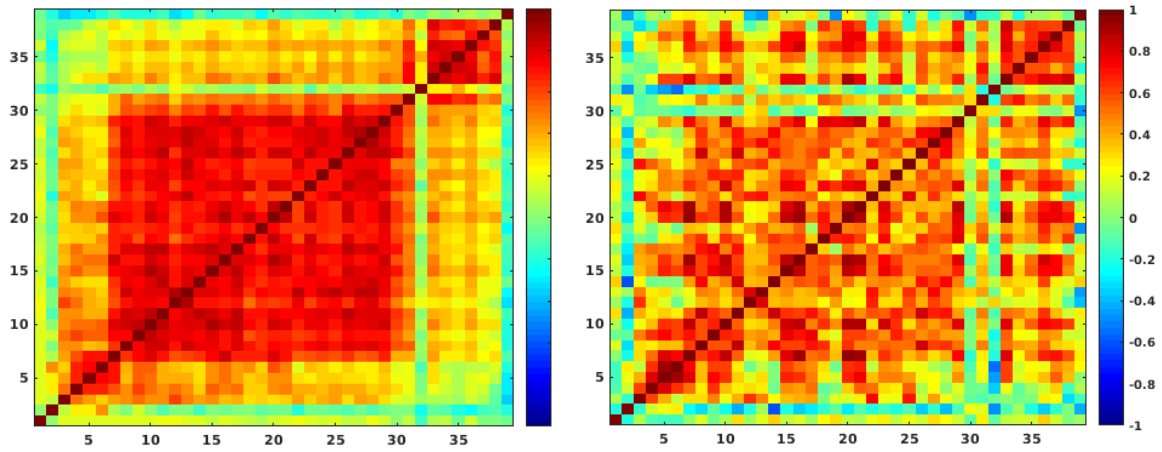

Figure 4.9a (left) and 4.9b (right). Spatial cross-correlation for 38 tide gauges in relation to one another for 1920-2006. Interannual (a) and decadal (b) variability, with lowpass filter 13-month and 121-month respectively. Location 31 corresponds to the latitude of Cape Hatteras (35.1°N) and location 7 to Boston.

Several CMIP5 models produce close to identical spatial correlation patterns to the PSMSL tide gauge records with a divide at Boston (~location 7, 42.4°N) and Cape Hatteras (~ location 31, 35.1°N) (*Figure 4.10 and 4.11*). On both timescales, about half of the models capture the distinct spatial characteristic of CSL variability on either side of Cape Hatteras, as seen in interannual tide gauges (*Figure 4.9a*). The models showing CSL patterns closest to the observations are; bcc-csm1-1(3), bcc-csm1-1-m(4), CNRM-CM5-2(14), CNRM-CM5(15), CSIRO-Mk3-6-0(16), GFDL-CM2p1(21), GISS-E2-R(26), MIROC4h(32), MPI-ESM-MR(37), MPI-ESM-P(38), MRI-CGCM3(39), MRI-ESM1(40), NorESM1-ME(41) and NorESM1-M(42) for interannual variability (*Figure 4.10*), and bcc-csm1-1(3), bcc-csm1-1-

m(4), CESM1-CAM5(8), CNRM-CM5-2(14), CNRM-CM5(15), CSIRO-Mk3-6-0(16), GFDL-CM2p1(21), GFDL-ESM2M(24), GISS-E2-R-CC(25), MIROC4h(32), MPI-ESM-MR(37), MPI-ESM-P(38), MRI-CGCM3(39), MRI-ESM1(40), NorESM1-ME(41) and NorESM1-M(42) for decadal variability (*Figure 4.11)*. Noticeably, while strong spatial correlations are found between Cape Hatteras and Boston on interannual timescales in observations, this area is highly correlated in several models on both interannual and decadal timescales.

There are also several models that display three regions of high spatial SSH correlation with separations close to Boston (location 7, 42.4°N), Baltimore (location 20, 39.3°N) and Cape Hatteras (location 31, 35.1°N). For interannual variability (*Figure 4.10*), these models are: CCSM4(6), CESM1-BGC(7), CESM1-CAM5(8), CESM1-FASTCHEM(9), CESM1-WACCM(10), GFDL-CM3(22), GFDL-ESM2G(23), GFDL-ESM2M(24), GISS-E2-R-CC(25), GISS-E2-R(26), HadGEM2-CC(27), HadGEM2-ES(28), MIROC5(33), MIROC-ESM-CHEM(34), MIROC-ESM(35), MPI-ESM-LR(36), MPI-ESM-MR(37), NorESM1-ME(41) and NorESM1-M(42). For decadal variability (*Figure 4.11*): CanESM2(5), CCSM4(6), CESM1-BGC(7), CESM1-CAM5(8), CESM1-FASTCHEM(9), CESM1-WACCM(10), FIO-ESM(20), GFDL-CM2p1(21), GFDL-CM3(22), GFDL-ESM2M(24), GISS-E2-R-CC(25), GISS-E2-R(26), HadGEM2-ES(28), MIROC5(33), MIROC-ESM-CHEM(34), MIROC-ESM(35) and MPI-ESM-LR(36). Yet, the division into two versus three spatially coherent regimes is not clear-cut.

Moreover, there are some models that show clear outlying behaviour or no specific detectable spatial correlation pattern. For interannual variability (*Figure 4.10*) these models are: CanESM2(5), CMCC-CM(12), CMCC-CMS(13), EC-EARTH(17), FGOALS-s2(19). CanESM2(5) displays a coastal division into three sections of high correlation, CMCC-CM(12) and CMCC-CMS(13) show diffuse patterns with several coastal divisions, EC-EARTH(17) also shows very diffuse patterns as does FGOALS-s2(19). For decadal variability (*Figure 4.11*), the most outlying models are ACCESS1-3(2), CMCC-CESM(11), EC-EARTH(17), FGOALS-s2(19) and HadGEM2-CC(27), all showing unspecific patterns of spatial sea level coherence.

Interestingly, comparing the overall CMIP5 model performance between interannual (*Figure 4.10*) and decadal timescales (*Figure 4.11*), there is a tendency that CSL anomalies become more meridionally coherent on longer (decadal) timescales in several models (~17 models), spanning the oceanographic boundary of the Gulf Stream separation and Cape Hatteras. For example, CCSM4(6), CSIRO-Mk3-6-0(16), GFDL-ESM2M(24), HadGEM2-CC(27), MPI-

ESM-MR(37), MPI-ESM-P(38), NorESM1-ME(41), NorESM1-M(42) are among the models exhibiting greater meridionally coherence on decadal compared to interannual timescales.

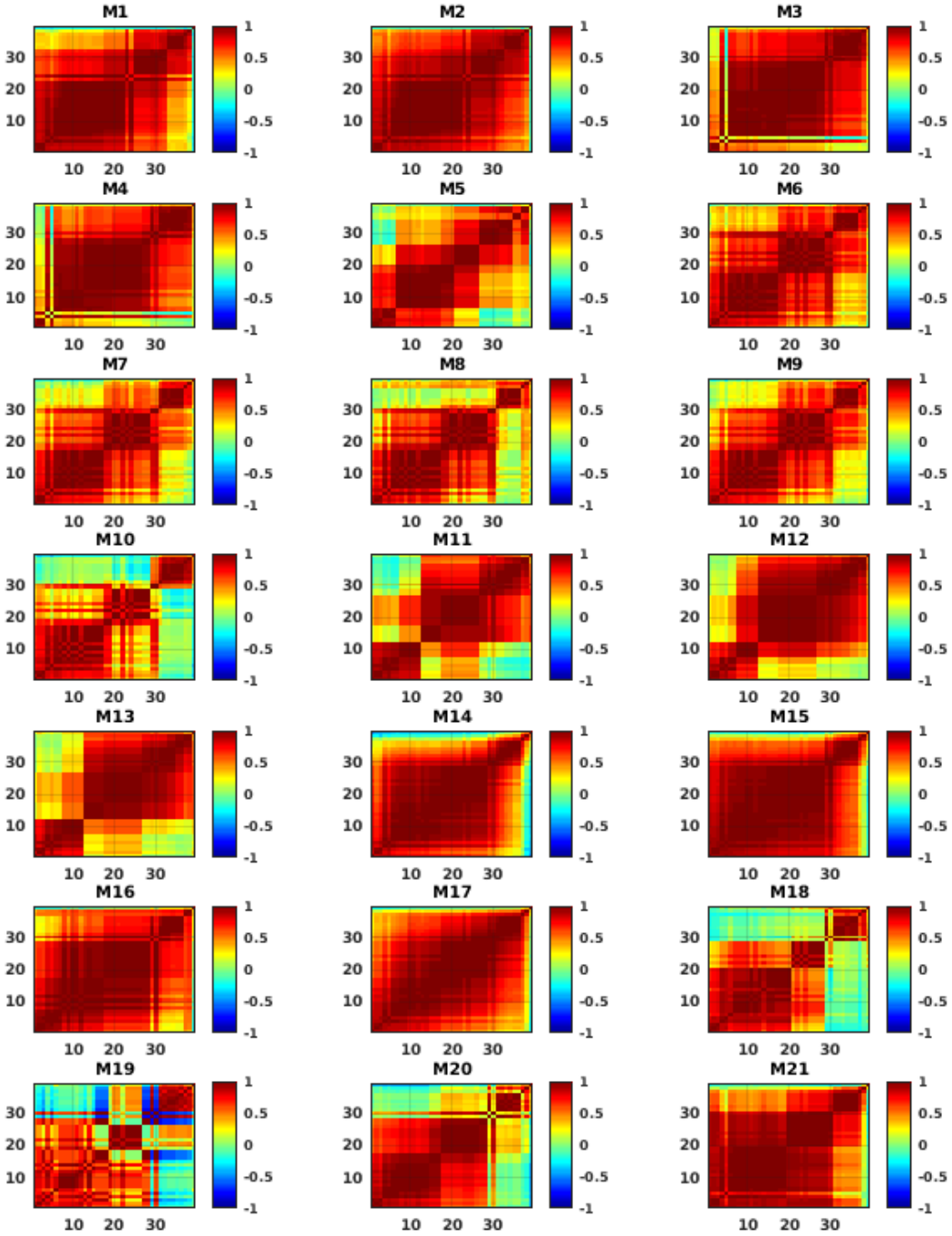

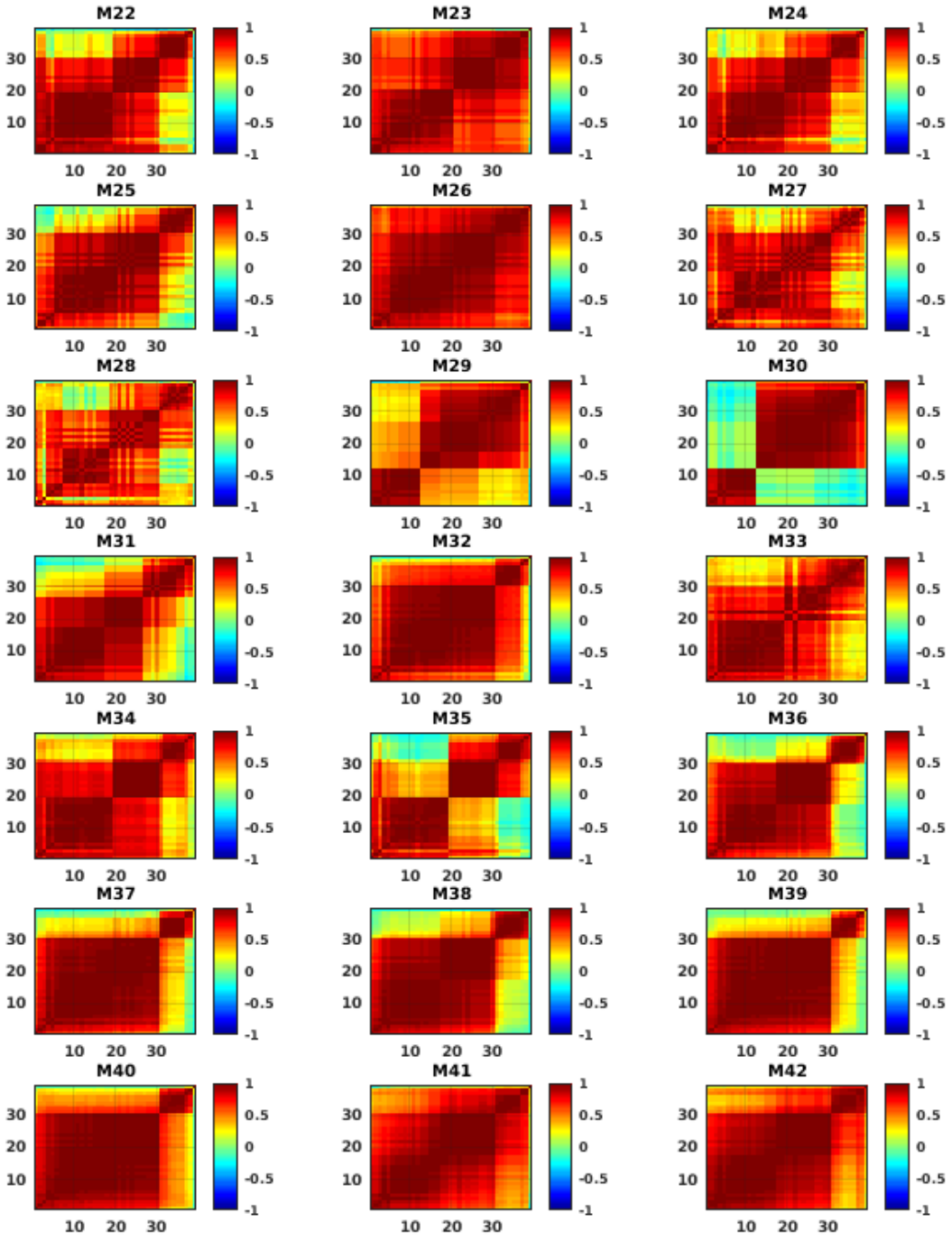

Figure 4.10. Spatial cross-correlation for simulated SSH between 38 grid points along the North American east coast relative one another. Historical runs (1920-2006) and interannual variability for 42 CMIP5 models. Location 30 corresponds to the latitude of Cape Hatteras (35.1°N). Location 20 is Baltimore and location 10 is Newport.

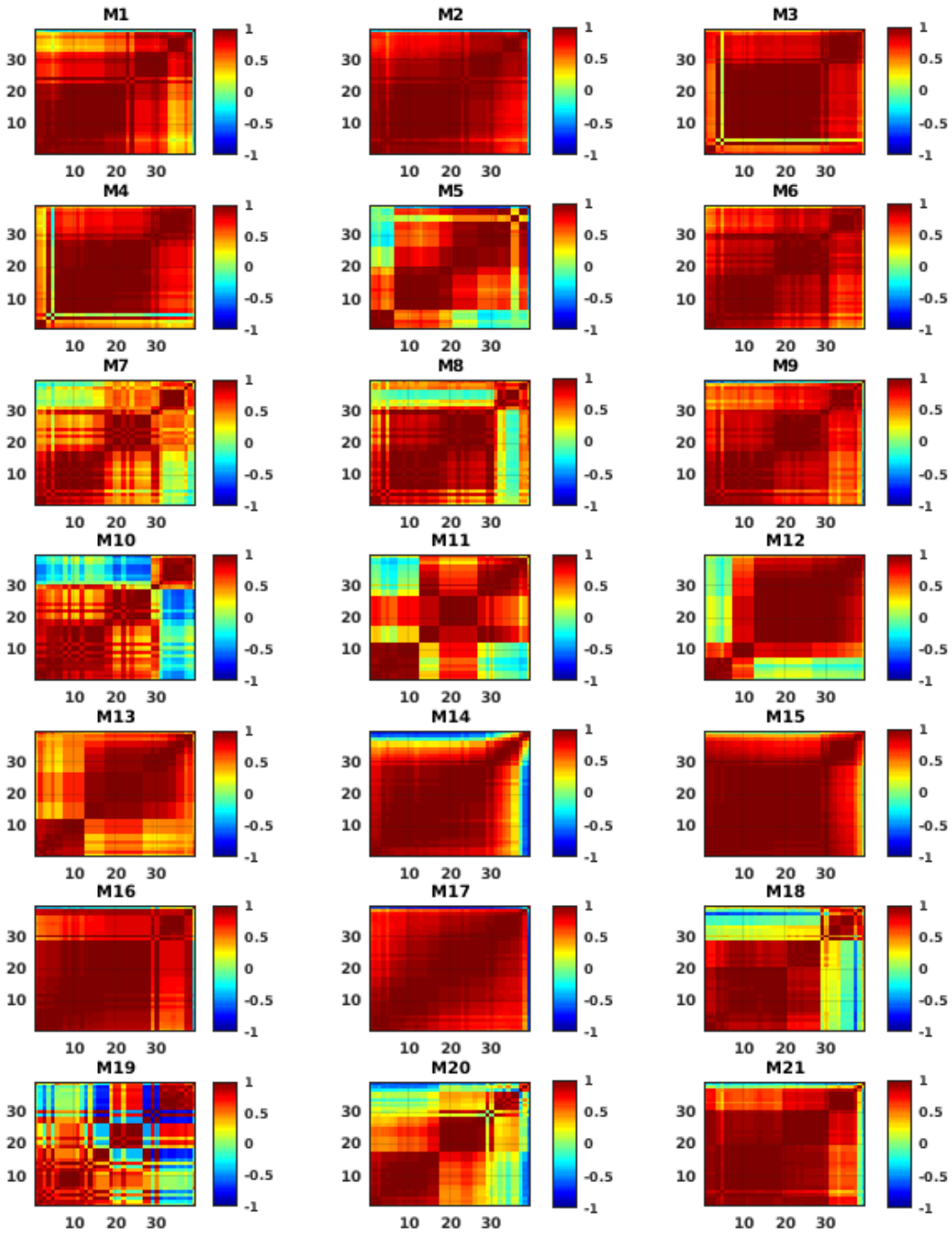
M1
M2
M3
M4
M5
M6
M7
M8
M9
M10
M11
M12
M13
M14
M15
M16
M17
M18
M19
M20
M21
10 20 30
1 0.5 0 -0.5 -1

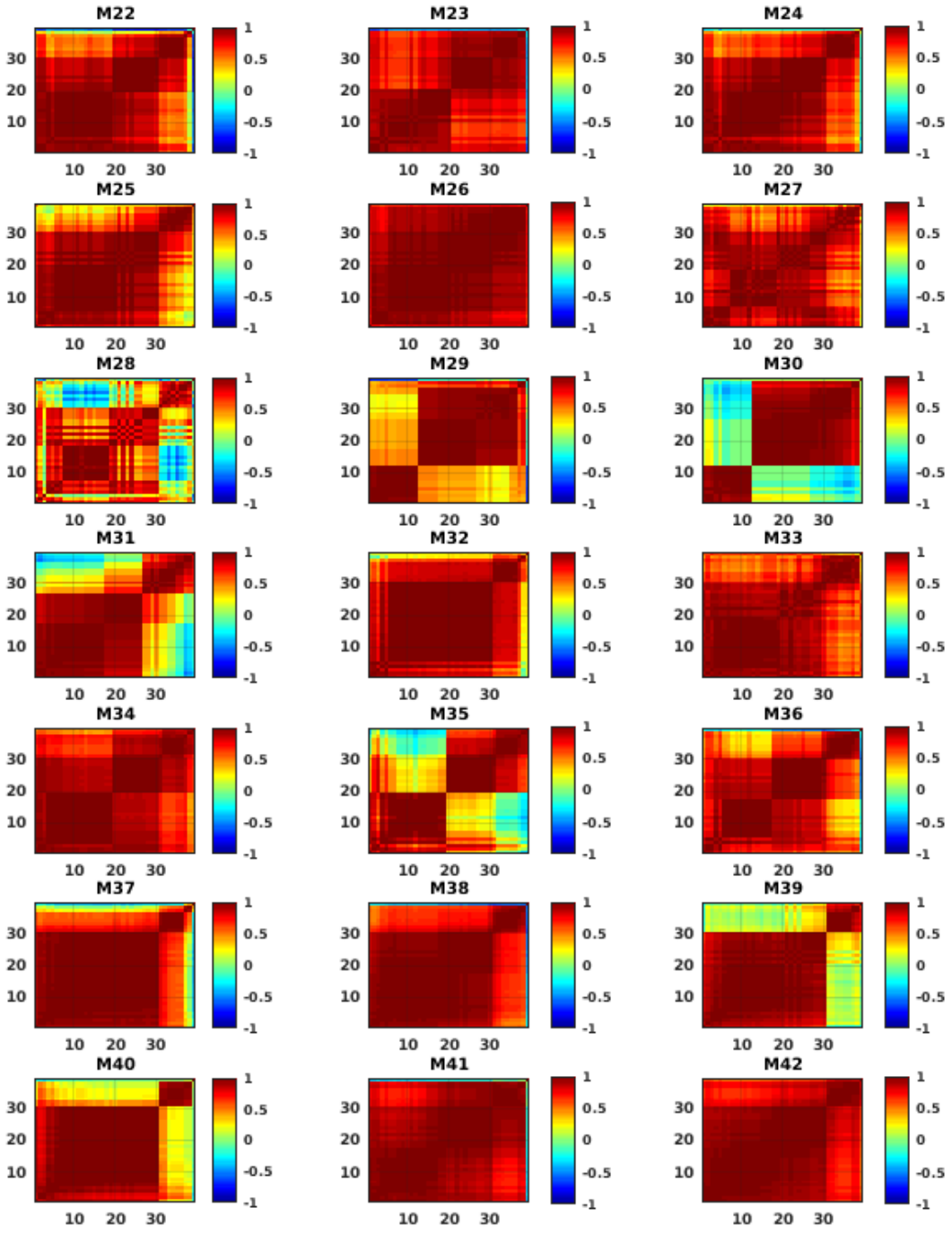

Figure 4.11. Spatial cross-correlation for simulated SSH between 38 grid points along the North American east coast relative one another. Historical runs (1920-2006) and decadal variability for 42 CMIP5 models. Location 30 corresponds to the latitude of Cape Hatteras (35.1°N). Location 20 is Baltimore and location 10 is Newport.

4.4 Summary

Although many models agree on several features of the spatiotemporal characteristics of the AMOC, there is still substantial inter-model spread, especially in relation to the magnitude of transport strength and dominant mode of temporal variability. Moreover, about half of the models exhibit a similar spatial pattern with discontinuity in interannual AMOC variations at ~40°N as in Bingham et al. (2007). Comparing the AMOC simulations with RAPID observations, relatively large model disagreement dominates the mean AMOC strength and standard deviation for interannual variability, with a general CMIP5 model underestimation of the observed magnitude of variability and the RAPID trend magnitude.

In terms of spatial CSL characteristics, it is clear that about half of the CMIP5 models (*Figure 4.10 and 4.11*) very closely mimic the observed distinct divide in spatial correlation patterns where sea levels are highly correlated on either side of Cape Hatteras (35.1°N), as seen in the PSMSL tide gauge data (*Figure 4.9*). Temporally, close to all CMIP5 models underestimate the observed tide gauge variance along the North American east coast on both interannual and decadal timescales, with the largest underestimation south of 35°N. This suggests that the AOGCMs may not reproduce the full range of potential CSL changes.

5 The Relationship between AMOC and sea level

5.1 Introduction

In this chapter I examine the relationship between the AMOC and dynamic sea level along the North American east coast. While both historical (1900-2006) and future simulations (2006-2300) are examined, the main focus is on the 20th century. The goal is to identify whether there are robust patterns of dynamic coastal sea level (CSL) along the western North Atlantic associated with variability of the AMOC across the CMIP5 models and in observations on interannual and decadal timescales.

The signature of the AMOC in sea level variability along the North American east coast is examined from two different approaches: 1) the direct relationship, including a comparison between initial AMOC simulations and a sea surface height-based reconstruction of the AMOC derived from linear regression (*Section 5.2 and 5.3*), and 2) calculating and testing a circulation index based on alongshore coastal sea level composites on either side of Cape Hatteras (*Section 5.4*). Furthermore, I compare the modelled and observed AMOC-sea level relationship (*Section 5.5*) and assess the stability of the relationship under global warming by analysing the RCP2.6 and RCP8.5 forcing scenarios (*Section 5.6*).

5.2 The direct relationship with sea level

I calculate the Pearson product-moment correlation coefficients to evaluate the direct relationship between simulated AMOC and sea surface height along the North American east coast at 38 grid points (grid points closest to the tide gauge locations, see *Table 3.2*) for 42 CMIP5 models during 1920-2006 for interannual and decadal timescales.

It should be emphasised that the latitude scale in the figures in *Chapter 5* (except *Figure 5.10, 5.11, 5.12 and 5.13*) is very non-linear due to the concentration of tide gauges at certain latitudes. This implies that the AMOC-CSL relationships are not sampled at all latitudes and that the relationships therefore are not representative of an average of all latitudes.

The analysis demonstrates that there is a large spread in the 42 CMIP5 models' historical simulations (1920-2006) of the AMOC-sea level relationship along the North American east coast (*Figure 5.1*). A majority of the models simulate a negative relationship, but the strength and spatial characteristics of the relationship vary, especially with respect to interannual variability (*Figure 5.1a*). A larger number of CMIP5 models produce moderate to strong anticorrelations (<-0.5) between AMOC and CSL for decadal variability (about half of the

models) (*Figure 5.1b*) compared to interannual timescales (about one-fourth of models) (*Figure 5.1a*). Moreover, a larger number of models exhibit positive correlations on interannual (~8 models) than decadal timescales (~4 models), with positive correlations being weak for many models (<0.25). The mean AMOC-CSL correlation on decadal timescales, averaged across all models and coastal sites, is -0.3966, with 21 CMIP5 models exhibiting a mean (spatial) anticorrelation of <-0.5. On interannual timescales, the mean correlation is -0.2357, with only three models obtaining mean (spatial) anticorrelations of <-0.5.

For both interannual and decadal correlation analysis, there are three model families that stand out and produce particularly strong negative correlations along most of the latitudinal stretch (*Figure 5.1*): ACCESS, GFDL (except GFDL-CM2p1) and NorESM1. Specifically, the models showing the strongest negative correlations are ACCESS1-0(1), ACCESS1-3(2), GFDL-CM3(22), GFDL-ESM2G(23), GFDL-ESM2M(24), NorESM1-ME(41), and NorESM1-M(42). For decadal variability GISS-E2-R-CC(25) also displays particularly strong negative correlations (<-0.8) for large stretches along the North American Atlantic coast.

On interannual timescales (*Figure 5.1a)* there are several CMIP5 models that present positive correlations or very weak negative coefficients in the range between -0.25 and 0.25. The models that tend to have positive correlations or weak negative correlations for interannual variability along the coast are: CCSM4(6), CESM1-FASTCHEM(9), CNRM-CM5-2(14), CSIRO-Mk3-6-0(16), FGOALS-g2(18), GFDL-CM2p1(21), GISS-E2-R(26), HadGEM2-ES(28), IPSL-CM5A-MR(29), IPSL-CM5B-LR(31), MIROC5(33), MIROC-ESM-CHEM(34), MPI-ESM-LR(36), MPI-ESM-MR(37) and MRI-CGCM3(39). The strongest positive correlations for these models tend to occur north of ~38°N. Combined, the model families IPSL, MIROC and MPI appear to have the weakest negative and most positive AMOC-SSH correlations.

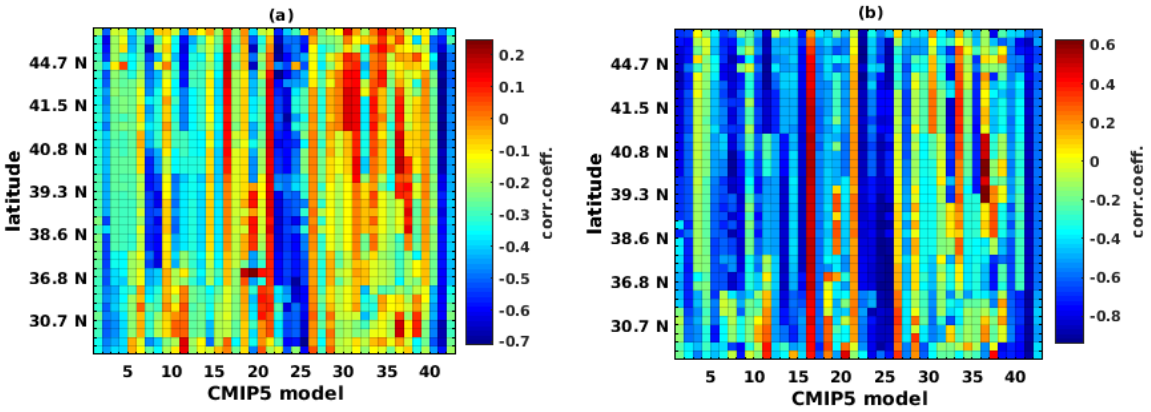

Figure 5.1. Correlations (42 models) simulated AMOC against SSH for historical runs 1920-2006 for 38 locations along the North American east coast (Kew West, Florida to Rimouski, Canada). (a) interannual variability with 13-month boxcar filter, (b) decadal variability with 121-month boxcar filter. Note that figures (a) and (b) use different colour scales. The 12 models that exhibit the r1i1p1 ensemble only are: 7, 11, 12, 13, 14, 23, 24, 25, 31, 34, 40, 41, and these models should have fully consistent correlation relationships.

Furthermore, CSIRO-Mk3-6-0(16) and GFDL-CM2p1(21) stand out by producing positive correlations for larger coastal stretches than any other of the 42 AOGCMs. Noticeably, GFDL-CM2p1(21) is greatly deviating from the other model versions in the GFDL family, as GFDL-CM3(22), GFDL-ESM2G(23) and GFDL-ESM2M(24) all generate strong negative correlations along the entire North American east coast.

On decadal timescales (*Figure 5.1b*) the models producing the weakest negative or positive correlations are CSIRO-Mk3-6-0(16), GFDL-CM2p1(21), GISS-E2-R(26), HadGEM2-ES(28), IPSL-CM5A-MR(30), MIROC5(33), MPI-ESM-LR(36) and MPI-ESM-MR(37). Similar to interannual variability, CSIRO-Mk3-6-0(16) and GFDL-CM2p1(21) stick out also on decadal timescales, generating strong positive correlations along the entire coastal stretch. CSIRO-Mk3-6-0(16) displays the strongest positive correlations (~0.6) for decadal variability, while GFDL-CM2p1(21) produces the strongest positive correlations (~0.2) for interannual variability.

Displaying the distribution of AMOC-SSH correlations across the 42 CMIP5 models for each single tide gauge site (*Figure 5.2a and 5.2b*), the 9-91st percentiles of models exhibit correlations in the range between ~ -0.78 and 0.23 on interannual timescales, and on decadal timescales between ~ -0.97 and 0.6. For both interannual and decadal variability, there is no specific location or region where it is clear that the models perform in a similar manner, although there is a tendency towards that the median of the 42 models exhibit slightly stronger anticorrelations for locations north of approximately 39°N (location 20). However, if including the 25-75 and 9-91 percentiles of models, this pattern dissolves.

Moreover it should be noted that all models included in the 25th to 75th percentiles generate negative AMOC-SSH correlations for both interannual and decadal timescales. If considering the models included in the 9th to 91st percentiles, it should be noted that decadal variability produces both stronger negative and stronger positive correlations, compared to interannual variability, which is expected to some extent due to reduced degrees of freedom. In addition, for the median model, the region with the strongest anticorrelations is between Atlantic City (location 19, 39.4°N) and Portland (location 6, 43.7°N). Moreover it appears to be a change in correlations just in the region north and south of 35°N (location 30). Thus, several models tend to agree that the AMOC and sea level exhibit an inverse relationship for long stretches along the North American east coast but with differences in the exact correlation strength latitudinally.

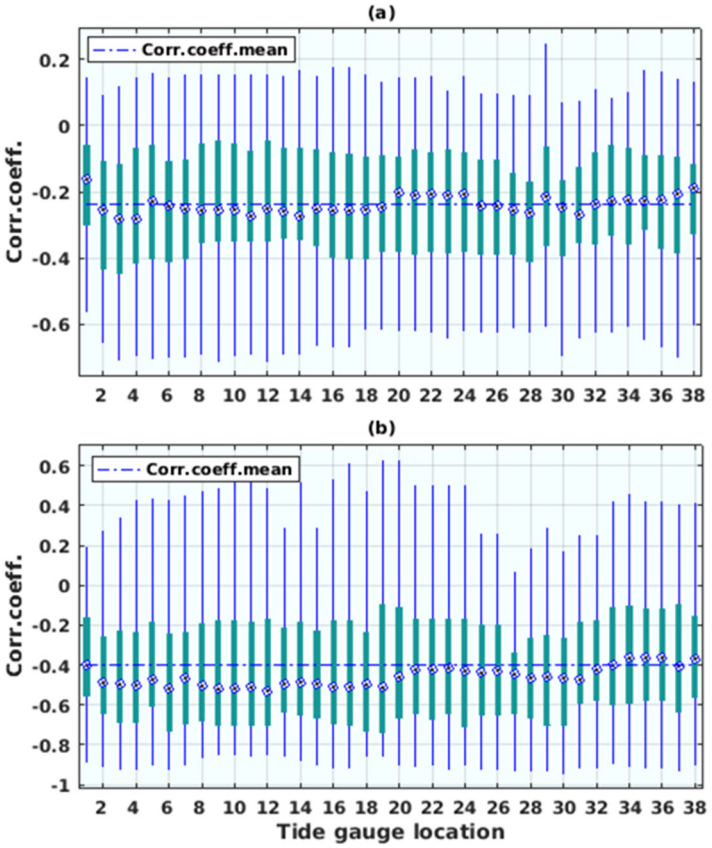

Figure 5.2. Correlations simulated AMOC against simulated SSH for historical runs 1920-2006. Correlation shown as boxplot for 38 tide gauge locations with correlation distributed across 42 CMIP5 models. (a) interannual variability with 13-month boxcar filter, (b) decadal variability with 121-month boxcar filter. Mean correlation (blue line). Median (blue dots), 25-75th percentiles (green box), and 9-91st percentiles (blue vertical line). Note that figures (a) and (b) use different coefficient scales on the y-axis. The 12 models that exhibit the r1i1p1 ensemble only are: 7, 11, 12, 13, 14, 23, 24, 25, 31, 34, 40, 41, and these models should have fully consistent correlation relationships.

In summary, analysis of the direct relationship between the AMOC and dynamic CSL along the North American east coast demonstrates that a majority of models generate AMOC-CSL anticorrelations for a large or the entire stretch from Key West (24.6°N) to Rimouski (48.5°N), although the exact strength of the relationship varies across models. Strong to moderate anticorrelations (<-0.5) are obtained in about half of the models on decadal timescales and about one-fourth of models on interannual timescales. Some models (about one-fourth) also exhibit stronger anticorrelations north of 35.1°N, compared to the region south of this latitude.

5.3 AMOC reconstruction by linear regression model

So far I have established moderate to strong anticorrelations between the AMOC and CSL variations in about half of the models on decadal timescales, as demonstrated by direct correlations. However, correlation analysis still shows a substantial inter-model spread, and there are fewer models obtaining a strong anti-phase nature between AMOC and CSL variations on interannual compared to decadal timescales. Here, AMOC-sea level connection is evaluated in CMIP5 models by reconstructing the AMOC from a linear regression model, linking simulated sea surface height variability along the North American coast with simulated AMOC.

Along the North American east coast from Key West, Florida to Rimouski, Canada, the 42 CMIP5 models demonstrate a relatively large spread in the linear regression slopes between AMOC and SSH for interannual variability (*Figure 5.3a*). At the same time there is greater model agreement between slopes from decadal linear regression, with a majority of CMIP5 models suggesting a slope between -0.3 and -0.8 Sv/cm (*Figure 5.3b*). It is notable that on interannual timescales, several models (e.g. CESM1-CAM5(8), CESM1-FASTCHEM(9), FGOALS-s2(19), FIO-ESM(20), GFDL-CM3(22), GFDL-ESM2M(24), NorESM1-ME(41), NorESM1-M(42)) show a marked divide at ~35°N, with generally weaker slopes for latitudes south of Cape Hatteras and stronger slopes northward of this latitude; this feature is less prominent for decadal regression analysis.

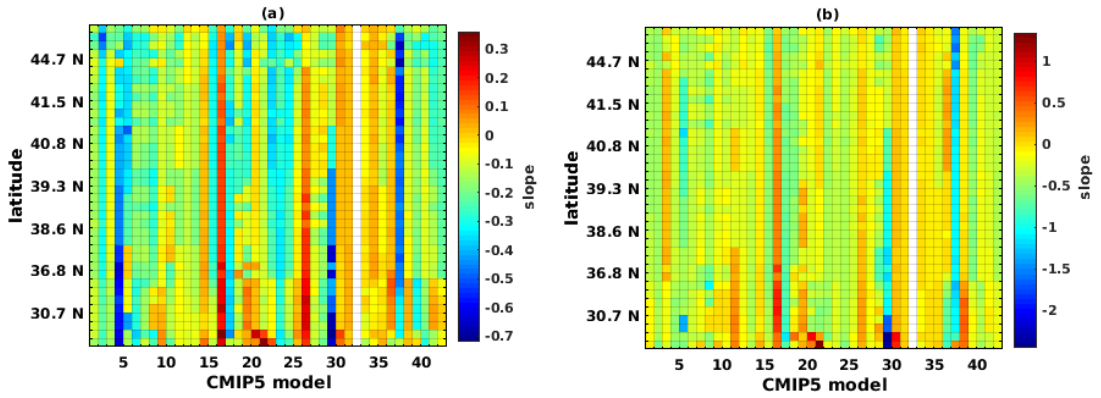

Figure 5.3a and 5.3b. Slope (Sv/cm) from linear regression model relating simulated SSH along the U.S. east coast to simulated AMOC. Historical runs 1920-2006. (a) interannual variability with 13-month boxcar filter. (b) decadal variability with 121-month boxcar filter. Note that figures (a) and (b) use different colour scales. The 12 models that exhibit the r1i1p1 ensemble only are: 7, 11, 12, 13, 14, 23, 24, 25, 31, 34, 40, 41, and these models should have fully consistent regression relationships.

For interannual variability, the majority of models (~three-quarters) display scaling coefficients between -0.1 to -0.35 Sv/cm. Three models demonstrate especially strong negative slopes (-0.5 to -0.7 Sv/cm): bcc-csm1-1-m(4), IPSL-CM5A-LR(29) and MPI-ESM-LR(36). Contrary, there are two models producing positive slopes (~0.3 Sv/cm) for large coastal stretches: CSIRO-Mk3-6-0(16) and GISS-E2-R(26). The IPSL and MIROC model families show no significant AMOC-CSL relationship. The GDFL models, except GFDL-CM2p1(21), show negative slopes of ~ -0.35 Sv/cm, as do the ACCESS and NorESM1 models. Thus, as seen in the previous analysis (*Section 5.2*), these model families again present as top performing models in terms of generating the strongest inverse relationships between the AMOC strength and SSH variability along the North American east coast.

For decadal variability a majority of models (~three-quarters) show negative slopes between -0.3 to -0.8 Sv/cm, whereby about one-third produce a relationship close to -0.5 Sv/cm (*Figure 5.3b*), which is not too different from Bingham and Hughes'(2009) slope of ~0.59 Sv/cm. Approximately two-fifths of AOGCMs exhibit decadal slope values that are in line with the scaling coefficients of order -1 to -2 cm/Sv recently noted in Little et al. (2019) as a diagnostic of the geostrophic AMOC-CSL relation. Noticeably, some AOGCMs (~11 models) show weaker negative slopes for the coastal coordinates south of 35°N compared to the northern counterpart. There are three models that show particularly strong negative slopes (<-0.6) for large stretches along the coast; CanESM2(5), HadGEM2-CC(27) and MPI-ESM-MR(37). CSIRO-Mk3-6-0(16) is the only model that produce a clear positive slope. The GDFL, ACCESS and NorESM model families (except GFDL-CM2p1(21)) also here generate a clear anti-phase AMOC-CSL nature with slopes of ~ -0.5 Sv/cm.

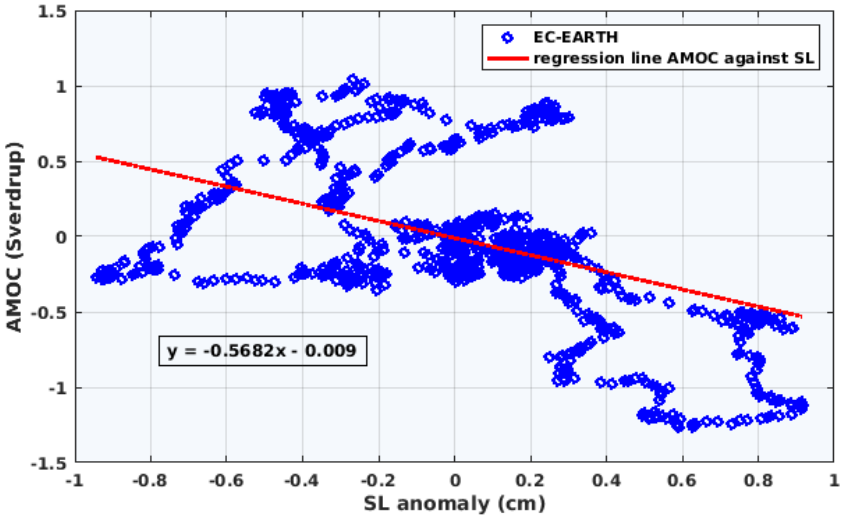

Figure 5.4. Scatter plot of simulated decadal coastal sea level variability against AMOC transport at 40.7°N (New York City) for EC-EARTH(17) 1920-2006. Linear regression line by least squares (red). Time mean, linear trend and seasonal cycle removed, and 121-month lowpass filter applied.

For each model, the slope from linear regression between simulated AMOC and sea surface height (see *Figure 5.4* for EC-EARTH(17)) was used in a linear regression equation to reconstruct AMOC variability from sea level. The AMOC reconstruction was then, for each model, correlated by Pearson's r with initial simulations of AMOC variability to test the suitability of a SSH-based AMOC reconstruction (*Figure 5.5 and 5.6*). Results show that the same models obtaining strong anticorrelations (*Figure 5.1*) also tend to exhibit a reconstruction that mimics the initial AMOC simulations well. A larger number of models do so on decadal compared to interannual timescales. The ACCESS1, CESM1 (except CESM1-FASTCHEM), CMCC, GFDL (except GFDL-CM2p1) and NorESM1 model families provide particular strong positive correlations between the reconstruction and initial AMOC simulations.

The potential uncertainty of the regression analysis should be highlighted. As *Figure 5.4* displays, the linear regression model of the AMOC-CSL link for EC-EARTH is subject to outliers. The visual outliers, depicted as the points on the upper left and bottom right corner of the scatter plot in *Figure 5.4* effectively alter the AMOC-CSL relationship, challenging the validity of the regression and any clear linear dependence of the connection. The presence of outliers indicates that the decadal variability pattern is not monotonic, but with "uneven" highs and lows in the decadal AMOC/SL relationship. However, even if the scatterplot of the decadal AMOC-CSL connection is subject to outliers and clustering or systematic arrangements of low-pass filtered data points reflective of the non-monotonic variability, the performance of a linear regression analysis in itself is an interesting attribution as it highlights the extent to which the models agree on previous attempts (e.g. Levermann et al. 2005,

Bingham and Hughes 2009) to establish a clear linear AMOC-CSL dependency. *Figure S1* in the Appendix, displaying the linear regression model, r square and residual plot of NorESM1-ME, emphasises that some CMIP5 models also obtain clearer negative linear relationships compared to that depicted by EC-EARTH in *Figure 5.4*. In any case, further work should test the validity of each respective regression model for the CMIP5 models, including analysis of R squared (coefficient of determination) and a residuals versus fits plot.

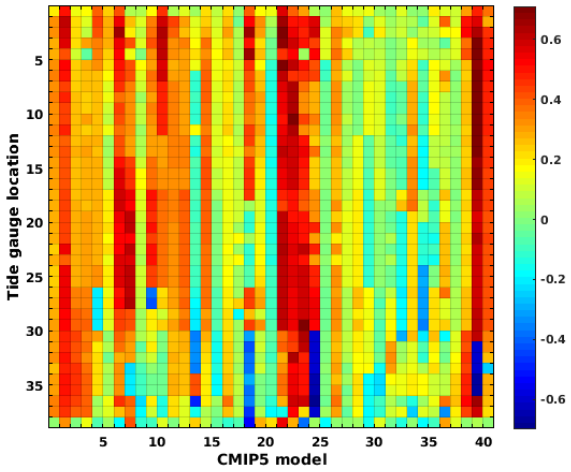

Figure 5.5. Correlation simulated AMOC against SSH-based AMOC reconstruction by linear regression model. 41 CMIP5 models and 39 tide gauge locations (39=Bermuda) 1920-2006.. 13-month lowpass filter, interannual variability. MIROC4h is omitted from analysis. The 12 models that exhibit the r1i1p1 ensemble only are: 7, 11, 12, 13, 14, 23, 24, 25, 31, 34, 40, 41, and these models should have fully consistent regression relationships.

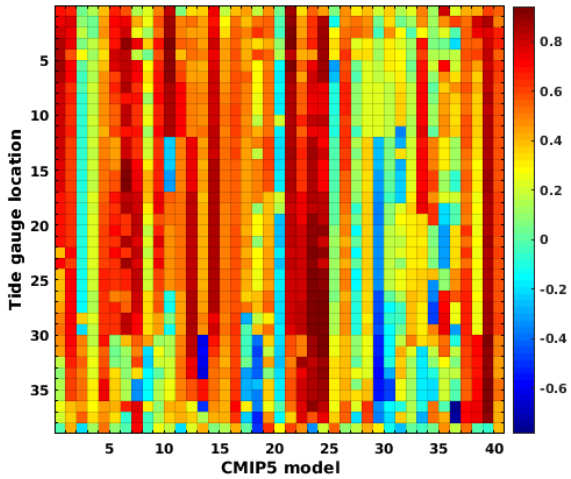

Figure 5.6. Correlation simulated AMOC against SSH-based AMOC reconstruction by linear regression model 1920-2006. 41 CMIP5 models and 39 tide gauge locations (39=Bermuda). 121-month lowpass filter, decadal variability. MIROC4h is omitted from analysis. The 12 models that exhibit the r1i1p1 ensemble only are: 7, 11, 12, 13, 14, 23, 24, 25, 31, 34, 40, 41, and these models should have fully consistent regression relationships.

Figure 5.7 shows the Taylor skill score for simulated AMOC along the North American east coast against the reconstructed AMOC. With 1 being the perfect score, with equal variance and perfect correlation, there is a larger number of CMIP5 models that obtain high skill scores for decadal variability (*Figure 5.7b*) compared to interannual (*Figure 5.7a*) variability, with mean skill scores of ~0.38 and ~0.16 respectively. On interannual timescales, the AOGCMs obtaining the highest Taylor skill score are ACCESS1-3(2), bcc-csm1-1-m(4), CESM1-BGC(7), GFDL-CM3(22), GFDL-ESM2G(23), GFDL-ESM2M(24), and NorESM1-ME(41) (*Figure 5.7a*). On decadal timescales, the models that achieve the highest skill scores are ACCESS1-3(2), CCSM4(6), CMCC-CMS(13), CNRM-CM5(15), GFDL-CM3(22), GFDL-ESM2M(24), GISS-E2-R-CC(25), MPI-ESM-MR(37) and MRI-CGCM3(39) (*Figure 5.7b*).

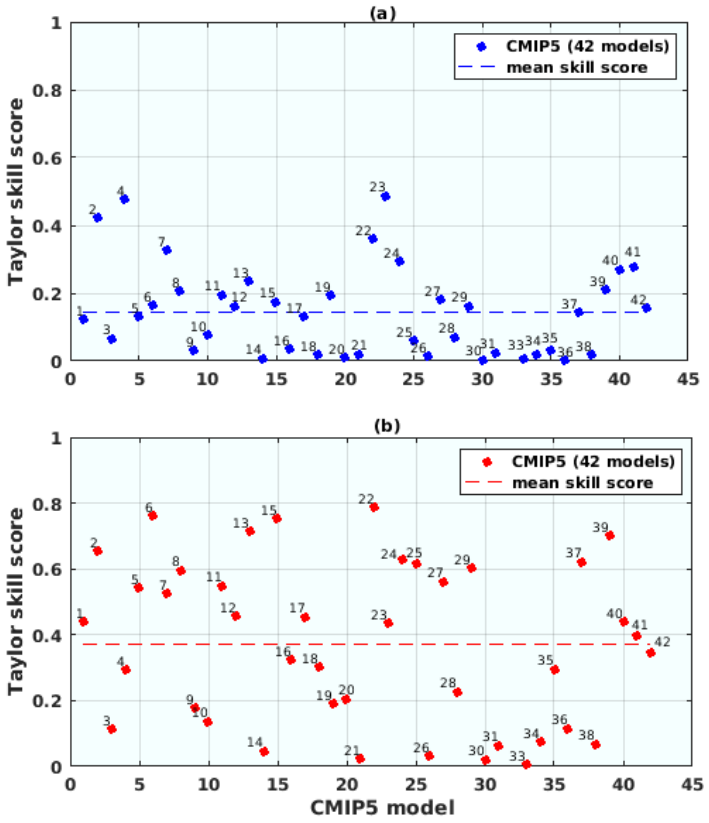

Figure 5.7a and 5.7b. Taylor skill score (Taylor 2001) simulated AMOC against reconstructed AMOC from linear regression model relating SSH along the U.S. east coast to the AMOC. Historical runs 1920-2006. Skill score for 38 grid points along the U.S. east coast and 42 CMIP5 models. (a) interannual variability with 13-month boxcar filter. (b) decadal variability with 121-month boxcar filter. Mean skill score (blue/red line). The 12 models that exhibit the r1i1p1 ensemble only are: 7, 11, 12, 13, 14, 23, 24, 25, 31, 34, 40, 41, and these models should have fully consistent regression relationships.

5.4 Alongshore sea level gradient and AMOC-index

Previous attempts to estimate the Gulf Stream from tide gauges have focused primarily on the east coast of North America, applying an offshore estimate of sea level from a reconstructed sea level or an island gauge (e.g. Levermann et al. 2005, Ezer 2013), such as Bermuda. Nevertheless, a major limitation of this approach is that the offshore measurement is in the eddy-filled ocean interior where mesoscale variations affect sea level fluctuation from short to long timescales (Wunsch 2008), making it difficult to obtain spatially-coherent signals of the ocean circulation (McCarthy et al. 2015).

Instead of using an offshore estimate, I here follow McCarthy et al.'s (2015) footsteps, using sea level estimates south and north of Cape Hatteras to bolster our understanding of spatial sea level dynamics along the coast and its relation to the AMOC. However, different from McCarthy et al.'s (2015) application of tide gauge records, I here calculate a sea surface height-based ocean circulation index based on simulations from CMIP5 SSH data. Particularly, I calculate sea level composites for locations north and south of Cape Hatteras respectively from simulated SSH. Compared to McCarthy et al. (2015), an additional 8 tide gauge locations are included in the analysis, and the northern (southern) composites are calculated by averaging SSH timeseries from CMIP5 at the same tide gauge equivalent locations 1-30(31-38) in *Table 3.2*. The index is then defined as the southern minus the northern composite (*Figure 5.8, 5.9*).

The objective of using simulated SSH instead of tide gauge records as the basis for the circulation index is to test the validity of the McCarthy et al. (2015) index in the CMIP5 models, examining the applicability of such an index in CMIP5. This is achieved by correlating simulated AMOC between 0.5°-70°N at 0.5 degree resolution (141 grid points) in the North Atlantic (north of equator) with the SSH composite-based ocean circulation index in all respective models, and then quantifying the potential added value of including both the Southern and Northern CSL composites in an index (*Figure 5.10, 5.12*).

Figure 5.8 and 5.9 present the timeseries of the northern and southern composites obtained from SSH simulations along with the SSH composite-based circulation index. An inverse relationship is obtained between the circulation index and Northeast sea level variations, indicating that sea level variability North of Cape Hatteras dominates sea level south of this point in the ocean circulation index.

Next, the SSH-based ocean circulation index is correlated with initial AMOC simulations for each single model between 0.5° and 70°N in the North Atlantic, testing the validity on the

McCarthy et al. (2015) index in the CMIP5 models. The most striking finding is that the McCarthy et al. index performs particularly well in many models considering decadal variability (*Figure 5.10b*). Initially, the positive correlations between the AMOC and the index obtained by multiple models indicate the applicability of a SSH-based circulation index that accounts for the alongshore sea level gradient. Approximately half of the models display strong positive correlations between modelled AMOC and the circulation index along large latitudinal stretches, especially north of 35°N, with a large majority of models (~32 models) generating positive correlations to some degree, either by a limited latitudinal stretch or by weaker positive correlation values on decadal timescales.

The models demonstrating the moderate to strong positive correlations (>0.5) along partial or long latitudinal stretches on decadal timescales are ACCESS1-0(1), ACCESS1-3(2), CCSM4(6), CESM1-BGC(7), CESM1-CAM5(8), CESM1-FASTCHEM(9), CMCC-CESM(11), CNRM-CM5(15), FGOALS-s2(19), GFDL-CM3(22), GFDL-ESM2M(24), GISS-E2-R-CC(25), GISS-E2-R(26), HadGEM2-CC(27), IPSL-CM5B-LR(31), MIROC-ESM-CHEM(34), MRI-CGCM3(39), NorESM1-ME(41) and NorESM1-M(42) (*Figure 5.10b*). There are only seven models showing moderate to strong positive correlations (>0.5) on interannual timescales, namely CESM1-CAM5(8), CMCC-CESM(11), FGOALS-s2(19), GFDL-CM3(22), MRI-CGCM3(39), NorESM1-ME(41) and NorESM1-M(42) (*Figure 5.10a*). It should also be noted that, on decadal timescales, four models stand out by producing negative correlations along most of or the entire latitudinal stretch: bcc-csm1-1(3), bcc-csm1-1-m(4), CSIRO-Mk3-6-0(16) and MPI-ESM-LR(36). That CSIRO-Mk3-6-0(16) shows outlying behaviour has also been noted in previous analyses (*see Chapter 5.2*).

Although the strong positive relationship between the AMOC and the circulation index in multiple models suggests the usefulness of a sea level composite-derived circulation index in CMIP5 models on decadal timescales, it should be noted that the moderate to strong correlation (>0.5) between AMOC strength and the index could to some extent be interpreted as a case of confirmation bias. Particularly, given that the Northern composite timeseries dominate the Southern-Northern difference (the SSH-based circulation index) (*Figure 5.8 and 5.9*), *Figure 5.10* is not too different from -1 the relationship shown in *Figure 5.1*, of direct correlations between simulated AMOC and simulated SSH along 38 tide gauge locations. Because of this, I therefore want to quantity the added value of including the Southern sea level component into the SSHcomposite-based circulation index versus focusing on sea levels north of Cape Hatteras alone as a potential AMOC proxy. As a first step towards understanding the potential added value of the Southern component (S), the calculations in *Figure 5.10* are repeated but with S=0 and N=0 separately, implying that simulated AMOC is

correlated with the Northeast sea level composite (N) and Southern composite respectively, and not the circulation index (*Figure 5.11*).

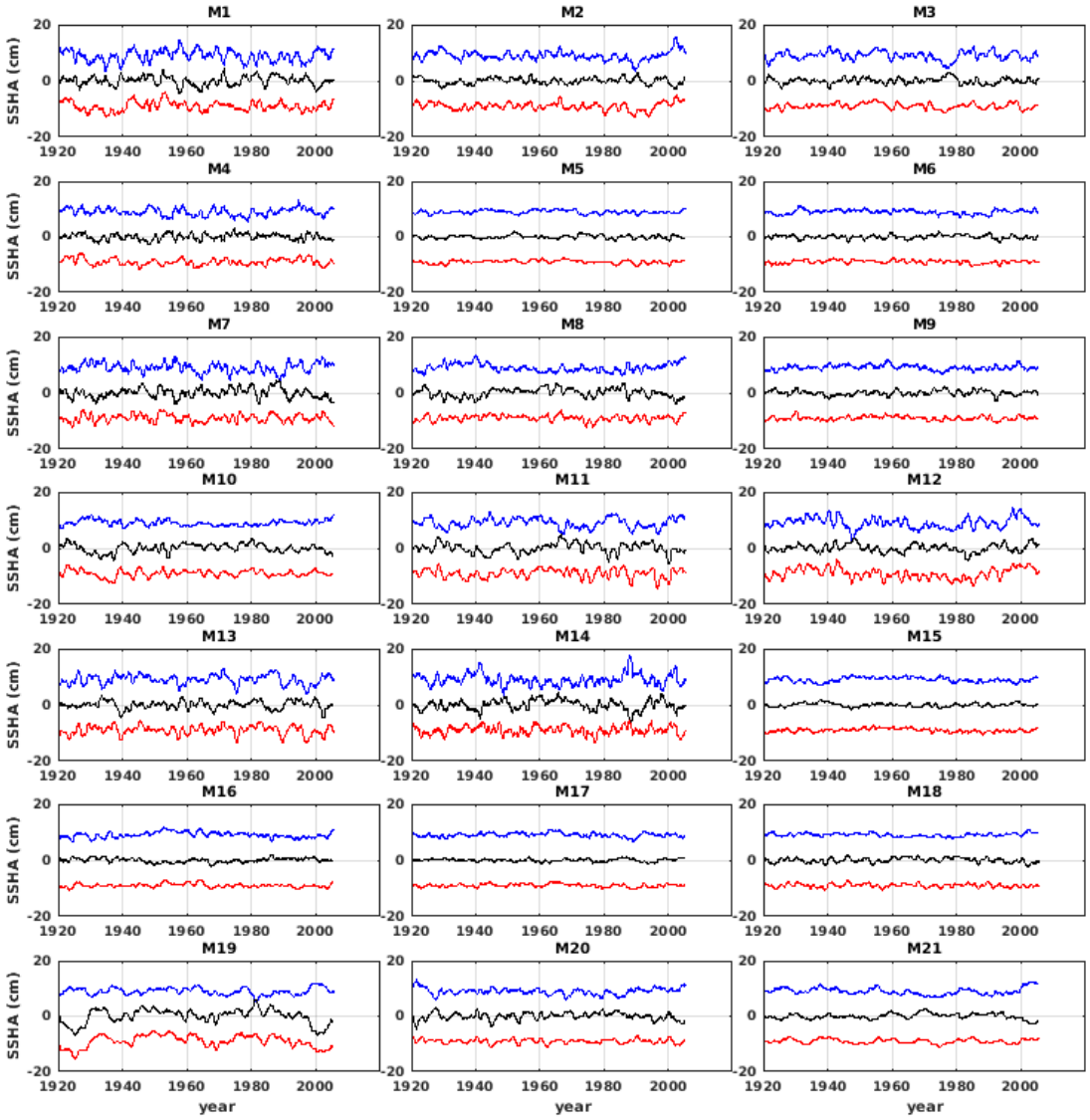

Figure 5.8a. Historical simulations of SSH for the Northeast (blue), SSH composite-based AMOC index (black) and Southeast (red) region along the North American east coast. Interannual variability during 1920-2006 for 42 CMIP5 models. The AMOC-index is defined as Southern minus Northern composite.

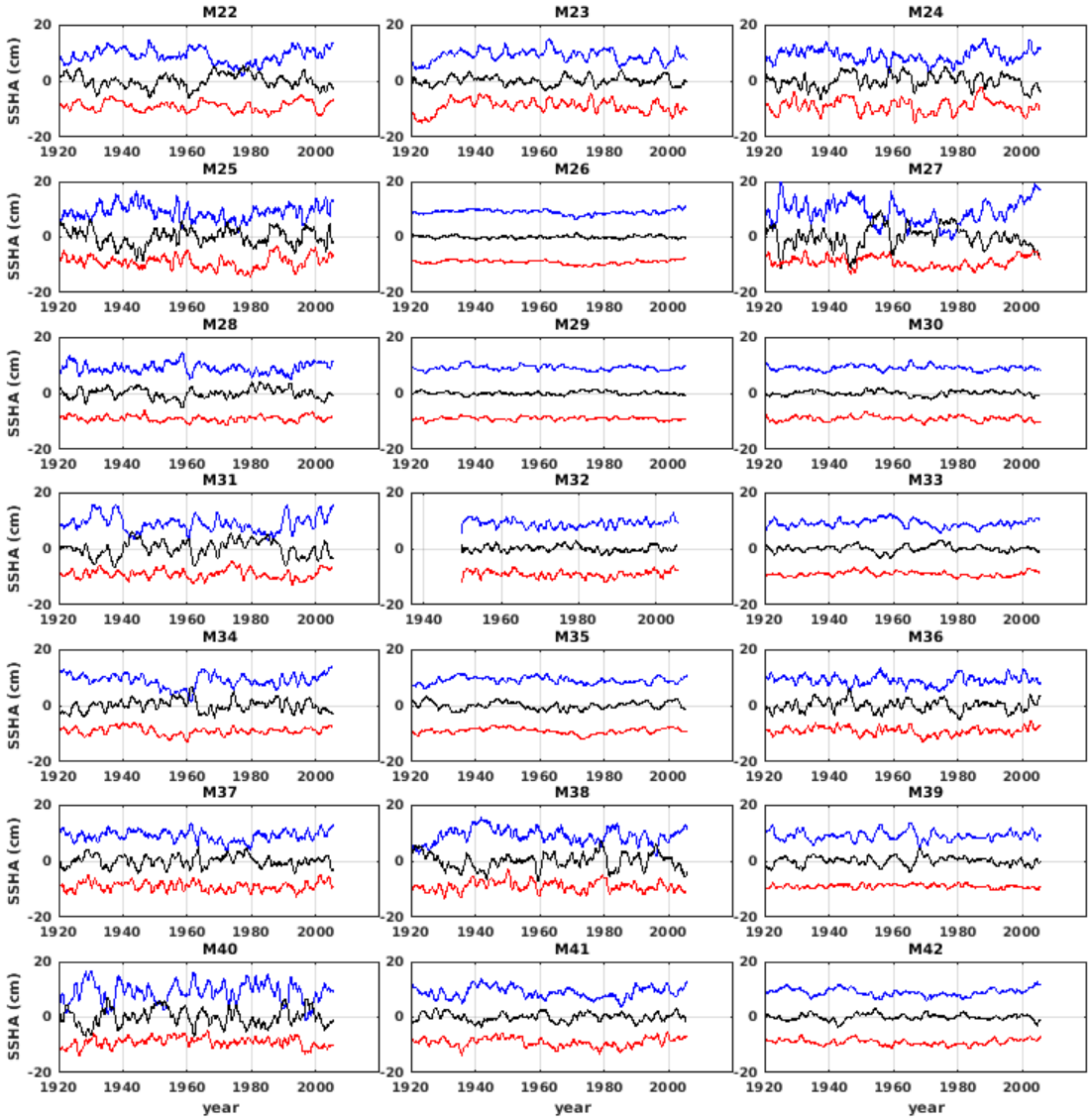

Figure 5.8b. Historical simulations of SSH for the Northeast (blue), SSH composite-based AMOC index (black) and Southeast (red) region along the North American east coast. Interannual variability during 1920-2006 for 42 CMIP5 models. The AMOC-index is defined as Southern minus Northern composite.

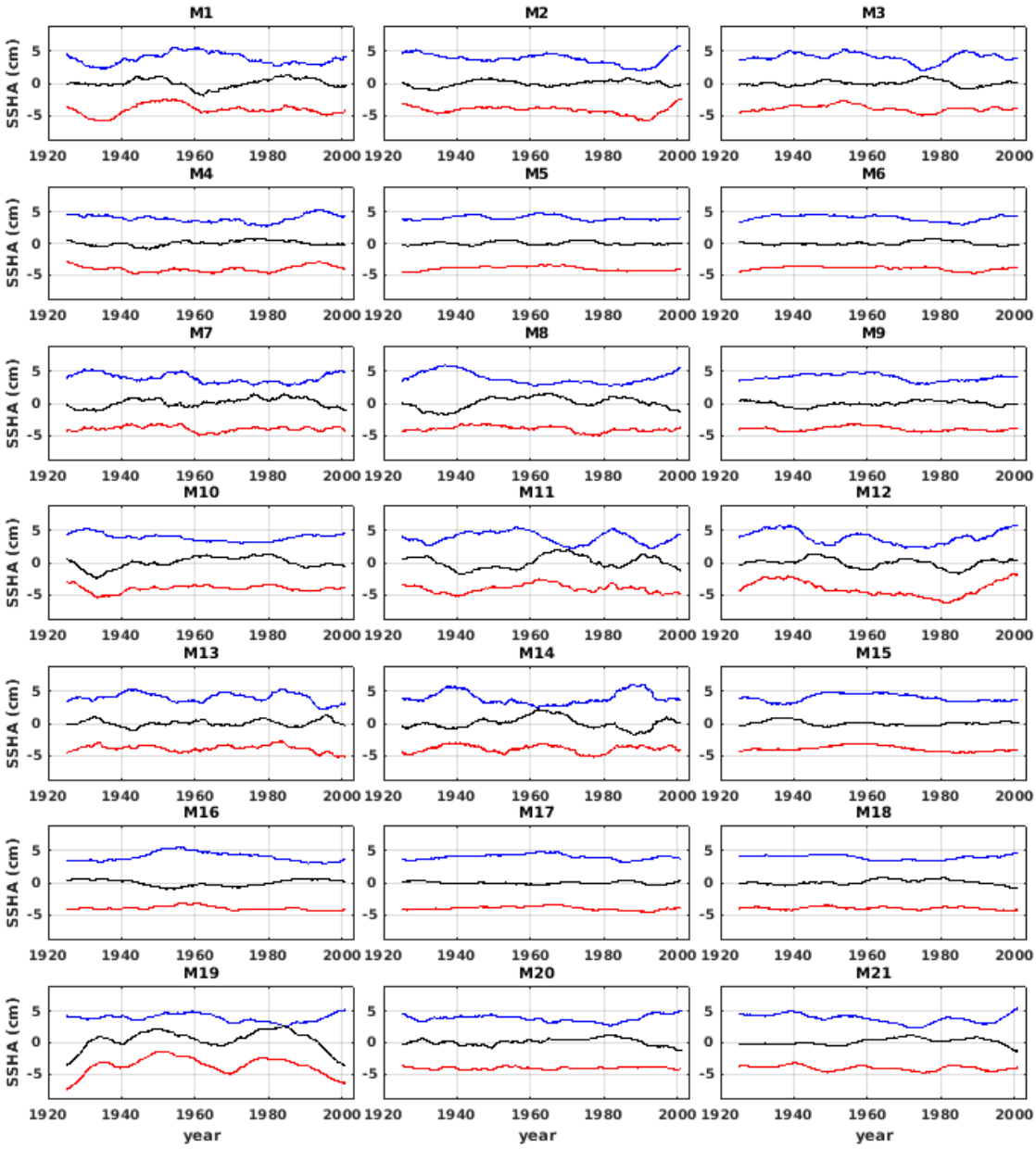

Figure 5.9a. Historical simulations of SSH for the Northeast (blue), SSH composite-based AMOC index (black) and Southeast (red) region along the North American east coast. Decadal variability during 1920-2006 for 42 CMIP5 models. The AMOC-index is defined as Southern minus Northern composite.

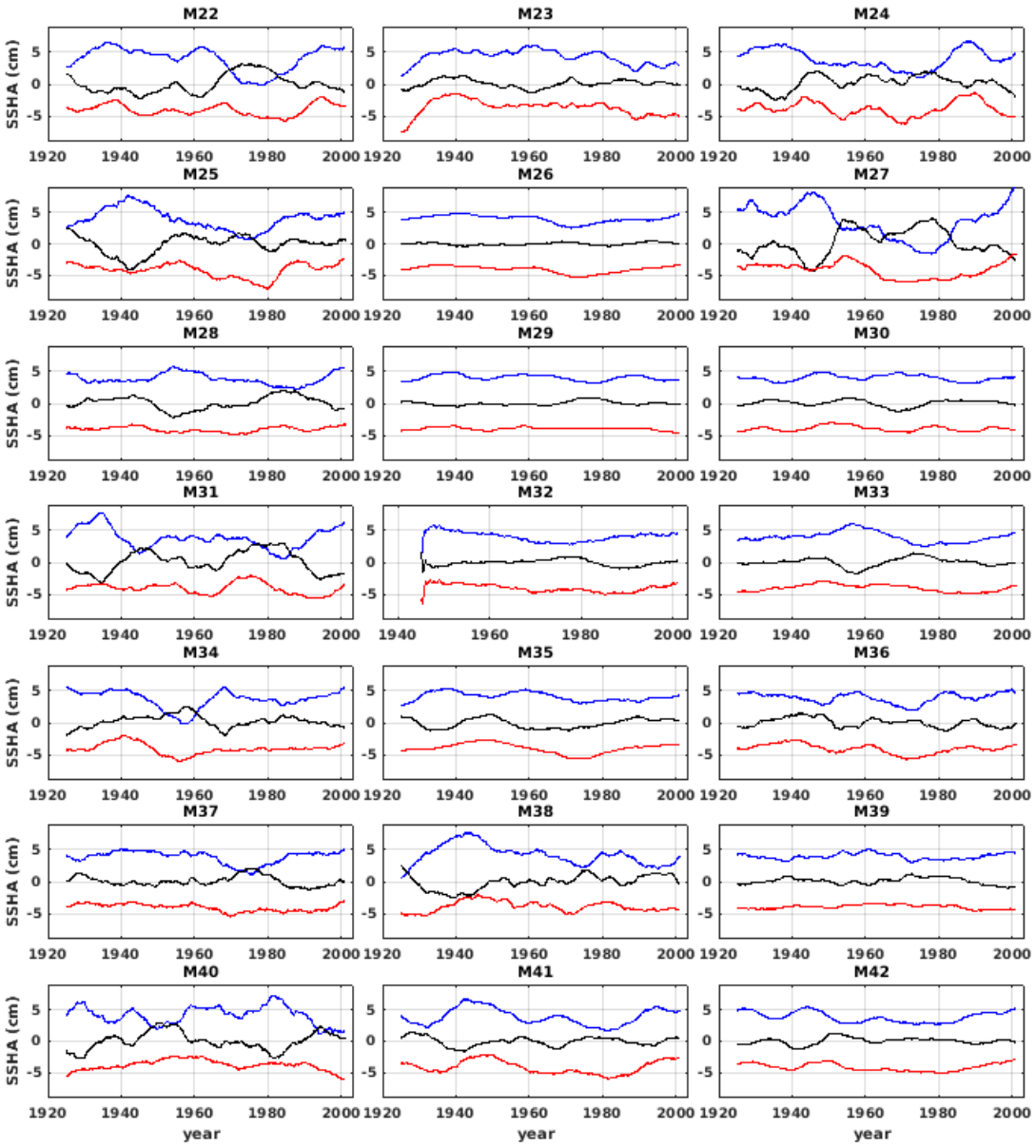

Figure 5.9b. Historical simulations of SSH for the Northeast (blue), SSH composite-based AMOC index (black) and Southeast (red) region along the North American east coast. Decadal variability during 1920-2006 for 42 CMIP5 models. The AMOC-index is defined as Southern minus Northern composite.

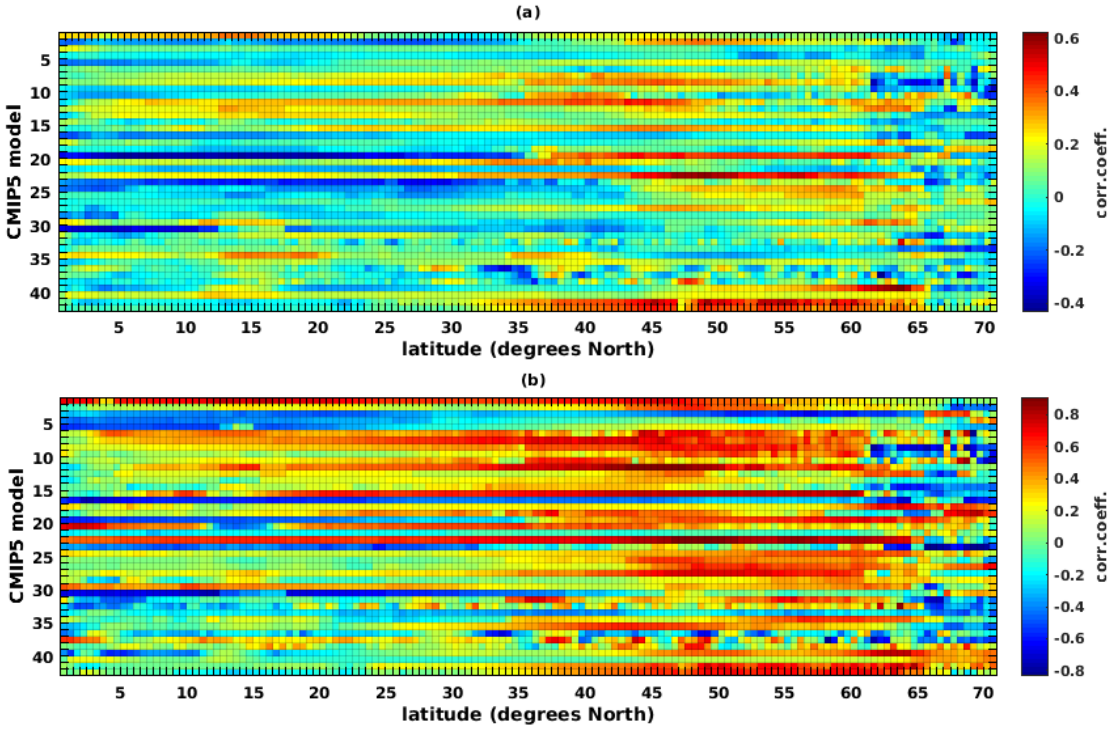

Figure 5.10. Correlation simulated AMOC against SSH-based AMOC index for historical runs 1920-2006. Correlation for 141 grid point locations in the North Atlantic (equator to 70°N) and 42 CMIP5 models. (a) interannual variability with 13-month boxcar filter. (b) decadal variability with 121-month boxcar filter. Note that figures (a) and (b) use different colour scales. The 12 models that exhibit the r1i1p1 ensemble only are: 7, 11, 12, 13, 14, 23, 24, 25, 31, 34, 40, 41, and these models should have fully consistent correlation relationships.

Examining the relationship between modelled AMOC and the Northern and Southern sea level composites respectively model by model (*Figure 5.11*), it is clear that a majority of models (~25 models) display negative correlations from the equator to ~ 60°N on decadal timescales for Northeast sea levels (*Figure 5.11b*). On interannual timescales in the Northeast (*Figure 5.11a*) there are several models generating anticorrelations, but the correlation strength is substantially weaker for many models compared to decadal timescales. For the Southeast, the AOGCMs generally produce weaker correlations and less spatially coherent negative correlations for the North Atlantic latitudinal stretch, although anticorrelations are generally stronger and present in a larger number of models on decadal (*Figure 5.11d*) compared to interannual variability (*Figure 5.11c*). The models obtaining moderate to strong anticorrelations (<-0.5) on decadal timescales for Southeast sea levels tend to be the same models obtaining strong anticorrelations for Northeast sea levels. Again, the model families ACCESS1-, GFDL (except GFDL-CM2p1(21)) and NorESM1 exhibit noticeably strong coherent anticorrelations on both timescales for both the Northeast and Southeast coast of North America.

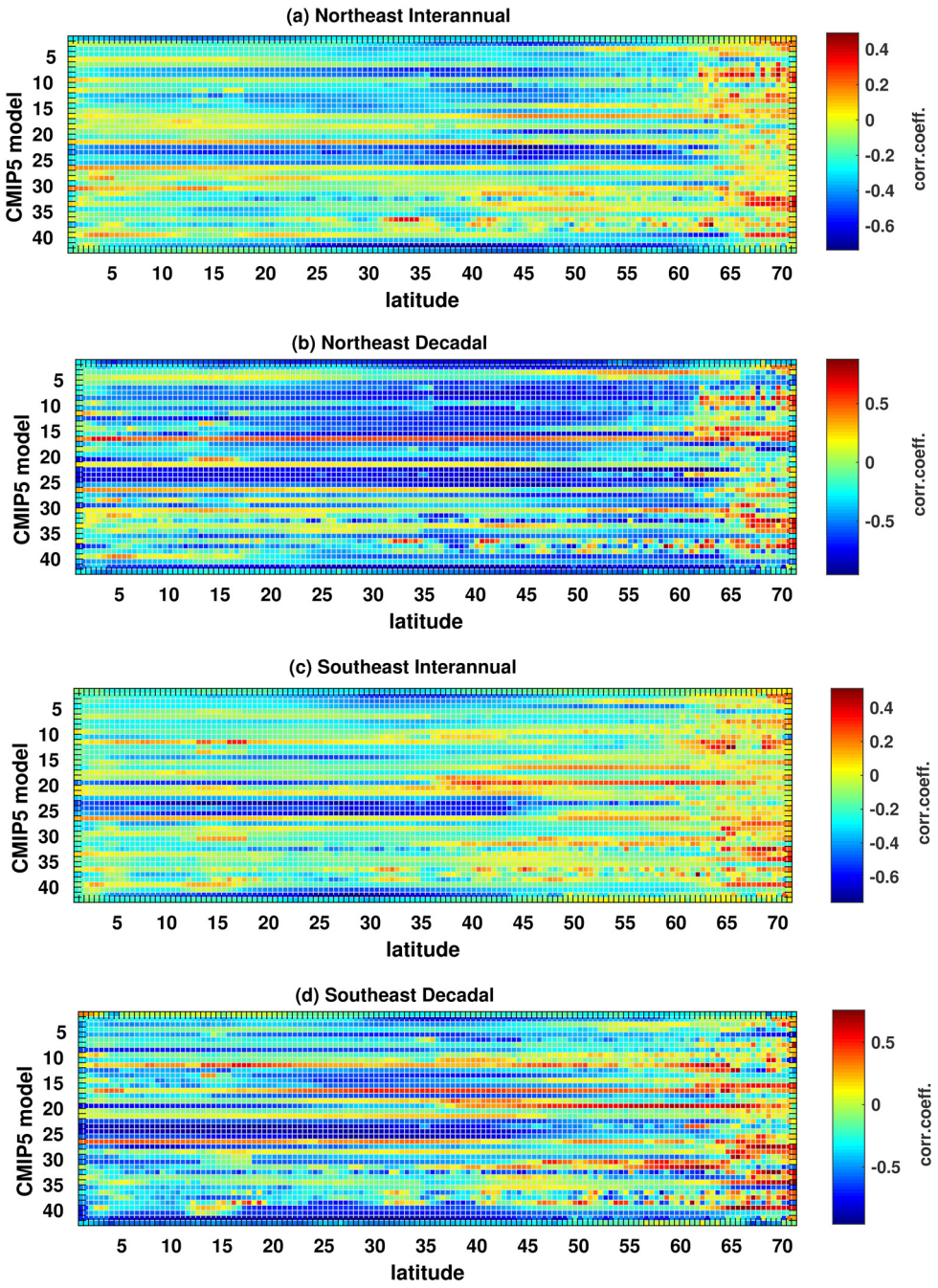

Figure 5.11. Correlation simulated AMOC against Northeast and Southeast sea level composites along the U.S. east coast. Historical runs 1920-2006. Correlation for 141 grid point locations in North Atlantic (equator to 70°N) and 42 CMIP5 models. Northeast composite is defined as locations north of Cape Hatteras (35.1°N). Southeast composite is defined as locations south of Cape Hatteras (35.1°N). Correlation between AMOC variability and sea level composites for (a) interannual variability for the Northeast, (b) decadal variability for the Northeast (c) interannual variability for the Southeast, and (d) decadal variability for the Southeast. Note that figures (a), (b), (c) and (d) use different colour scales. The 12 models that exhibit the r1i1p1 ensemble only are: 7, 11, 12, 13, 14, 23, 24, 25, 31, 34, 40, 41, and these models should have fully consistent correlation relationships.

Yet, because the sign of the AMOC-sea level relationship is generally negative, though magnitude varying, for both the northeastern and southeastern coasts in a majority of models, especially on decadal timescales *(Figure 5.11),* it is not clear why the SSH-based circulation index (Southern minus Northern sea level composite) should add predictive value as an AMOC proxy over just the Northern composite. To account for this and quantify the potential added value of including the Southern composite in a Southern-Northern circulation index, the absolute value of the correlation between simulated AMOC and the Northeast sea level composite (*Figure 5.11b*) is subtracted from the absolute value of the correlation between simulated AMOC and the SSH-based circulation index (*Figure 5.10b*) on decadal timescales. The same is done for the Southeast composite (absolute value of *Figure 5.10b* minus absolute value of *Figure 5.11d*), and for interannual variability (*Figure 5.10a minus 5.11a* and *Figure 5.10a minus 5.11c* for Northeast and Southeast composites respectively). The result is shown in *Figure 5.12,* which indicates at which latitudes, if any, the circulation index is out-performing either the Northern and/or Southern sea level composites in its predictive ability as an AMOC proxy.

Examining both interannual and decadal timescales, the most striking finding is that there is no predictive ability to be gained from the inclusion of the Southern component in the SSH composite-based circulation index on decadal timescales, where the predictive power is largely derived from the Northern component (*Figure 5.12c*). However, some predictive ability may be gained from the inclusion of sea levels south of 35°N on interannual timescales at certain latitudinal stretches in particular models (*Figure 5.12a*).

Particularly, on interannual timescales, the inclusion of the Southern component in the Southern-Northern circulation index tends to outperform the Northern composite alone, as indicated by the positive values (yellow to redness) generated by several models along certain latitudinal stretches in *Figure 5.12a*. The greater predictive ability of the index over the Northern composite is especially the case north of ~60°N, where a large majority of models show positive values (~34 models), and south of ~20°N (as seen in ~10 models) (*Figure 5.12a*). For some models (e.g. CSIRO-Mk3-6-0(16), FGOALS-g2(18), FGOALS-s2(19), FIO-ESM(20), GFDL-CM2p1(21) and IPSL-CM5A-MR(30)), the index outperforms the Northern sea levels along large latitudinal stretches from the equator to 70°N. Moreover, the index tends to add some predictive value over just the Southern composite in several models, especially north of ~45°N, as indicated by the positive values (yellow to redness) at these latitudes in *Figure 5.12b.*

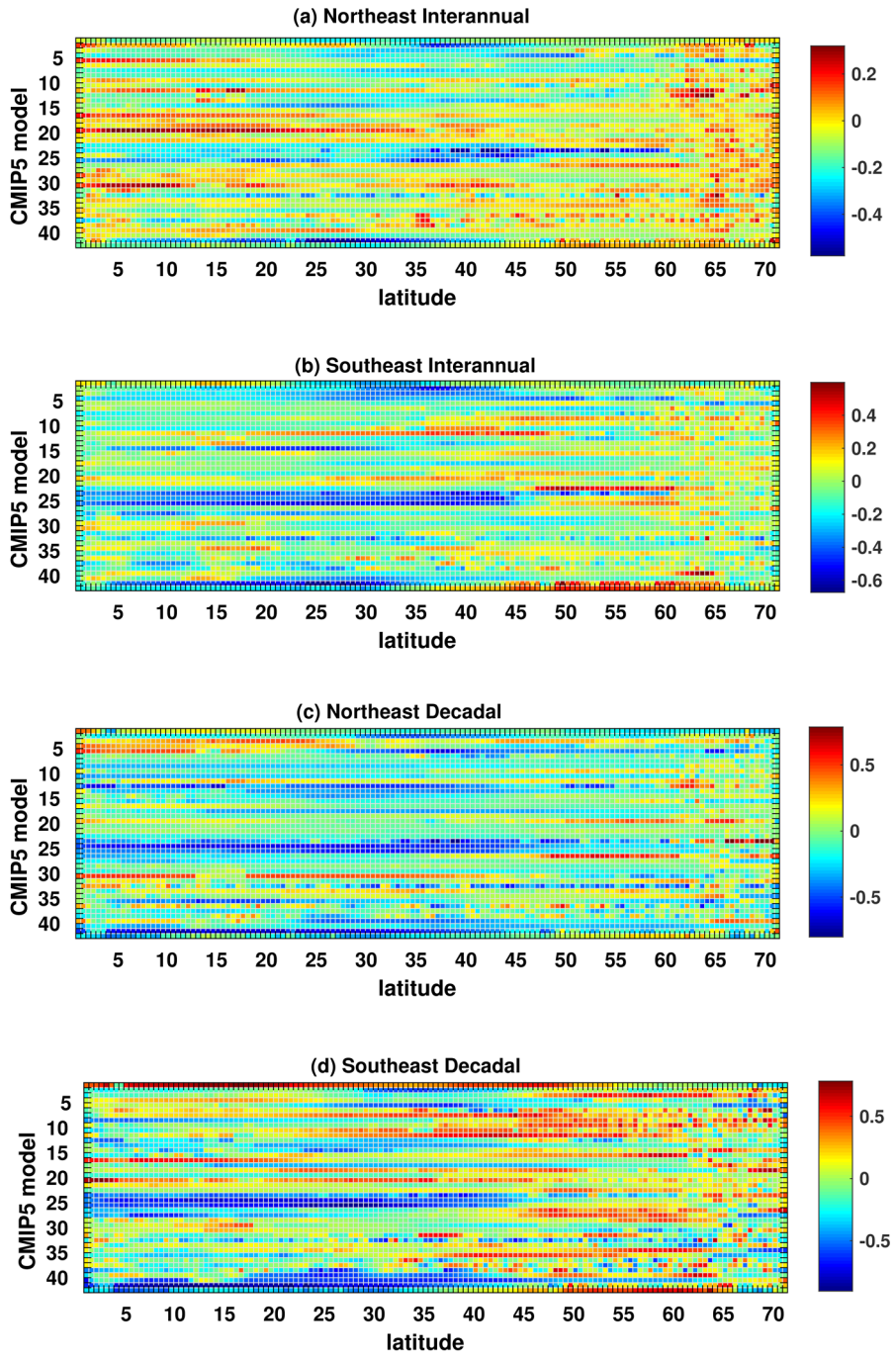

Figure 5.12. Predictive power of the SSH-based ocean circulation index (Southern minus Northern sea level composite) versus the Northeast or Southeast sea level composites as an AMOC proxy. The colour bar values indicate the added value to be gained from the inclusion of the Southern and Northern sea level composite respectively in the circulation index. The added value of the AMOC index is calculated by subtracting the absolute value of the correlation between simulated AMOC and the Northeast/Southeast sea level composite from the absolute value of the correlation between simulated AMOC and circulation index on decadal and interannual timescales respectively, for (a) the Northeast on interannual timescales, (b) the Southeast on interannual timescales, (c) the Northeast on decadal timescales, and (d) the Southeast on decadal timescales. Note that figures (a), (b), (c) and (d) use different colour scales. The 12 models that exhibit the r1i1p1 ensemble only are: 7, 11, 12, 13, 14, 23, 24, 25, 31, 34, 40, 41, and these models should have fully consistent correlation relationships.

On decadal timescales, most of the predictive power comes from the Northern component, as suggested by the negative values (green to blueness) shown in a large majority of models along large meridionally coherent stretches from the equator to ~65°N in *Figure 5.12c*. In fact, for some models (e.g. CMCC-CM(12), CMCC-CMS(13), GFDL-ESM2G(23), GFDL-ESM2M(24), GISS-E2-R-CC(25), MRI-CGCM3(39), MRI-ESM1(40), NorESM1-ME(41) and NorESM1-M(42)) the Southern-Northern index performs less well than either the Northern or Southern component alone on decadal timescales, as shown by the strong negative values in *Figure 5.12c* and *Figure 5.12d* respectively. While several models suggest that the index performs better than the Southern composite alone north of ~45°N for decadal variability (*Figure 5.12d*), the overall pattern on decadal timescales is still the superior predictive power of the Northern composite (*Figure 5.12c*).

Noticeably, some models (e.g. GFDL-ESM2G(23), GFDL-ESM2M(24), GISS-E2-R-CC(25), MRI-CGCM3(39), MRI-ESM1(40), NorESM1-ME(41) and NorESM1-M(42)) generate strong negative values on both interannual and decadal timescales (*Figure 5.12a-d*). A majority of these models show strong negative values between ~0°-50°N, indicating that either the Northern or Southern composites alone outperform the predictive ability of the index as an AMOC proxy on these latitudes.

Ignoring the latitudinal differences, by averaging across the latitudes in *Figure 5.12*, the overall pattern is that the Southern-Northern circulation index tends to perform less well than either the Northern (*Figure 5.13a and 5.13c*) or Southern (*Figure 5.13b and 5.13d*) components alone, as indicated by the negative values obtained by a slight majority of models. This applies to both interannual and decadal timescales. However, the relatively large inter-model spread and the weak negative values demonstrated by many models, if averaging latitudinally (*Figure 5.13a-d*), highlight that there is no absolute consistency in overall CMIP5 model behaviour on the predictive ability of the index and that the relevance of the index must be considered in the light of any latitudinal differences and timescale (as shown in *Figure 5.12a-d*).

In sum, a majority of CMIP5 models suggests that the inclusion of the Southern component in the Southern-Northern circulation index adds predictive value as an AMOC proxy on interannual timescales only at certain latitudinal stretches, but not on decadal timescales, where most of the predictive power comes from the Northern sea level component. Since the Northern composite's outperforming of the index on decadal timescales closely mimics the moderate to strong AMOC-CSL anticorrelations revealed in direct correlations (*Figure 5.1*), the McCarthy et al. (2015)-inspired index exhibit no clear usefulness in the CMIP5 ensemble.

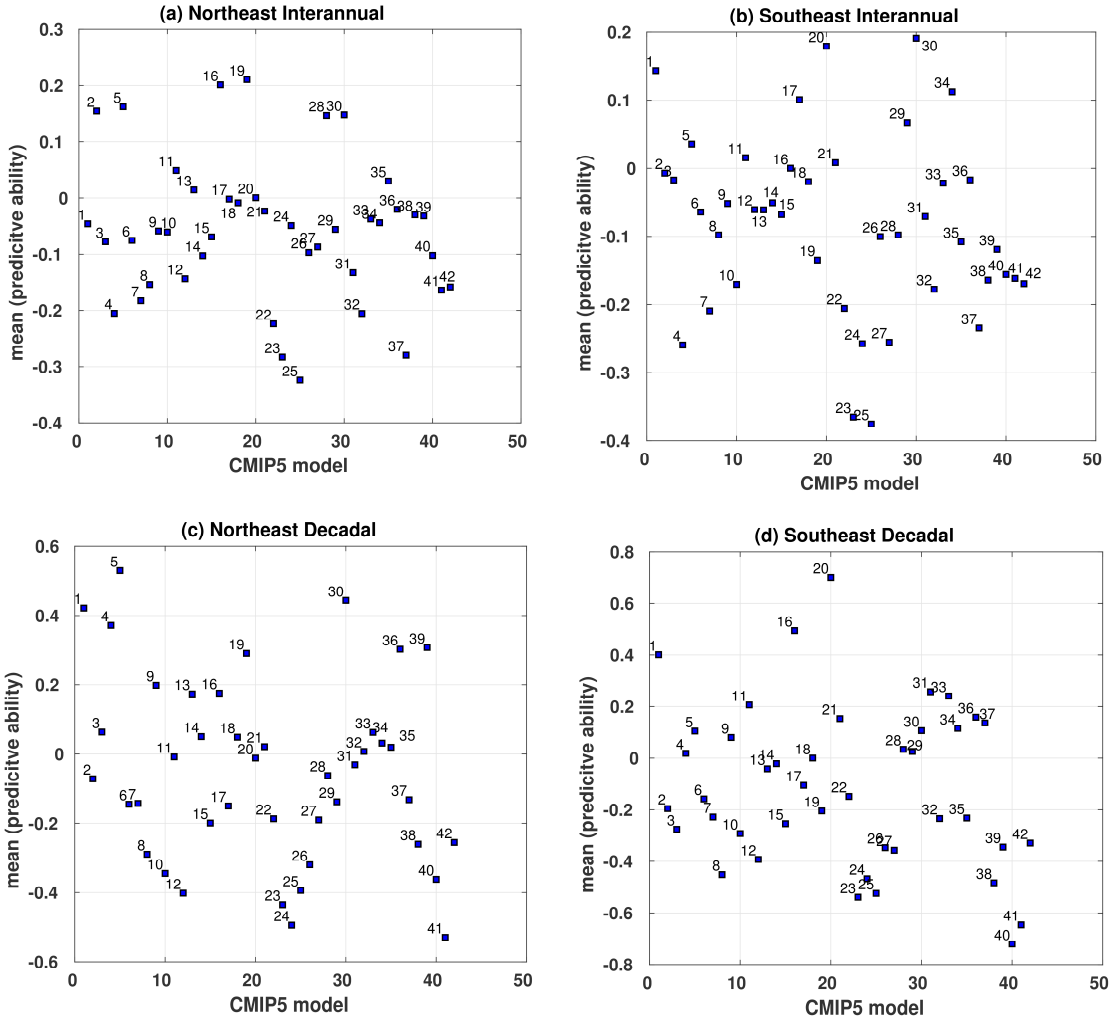

Figure 5.13. Predictive ability of the SSH-based ocean circulation index presented as the mean values across latitudes 0° to 70°N as a function of model. The added value of the AMOC index is calculated by subtracting the absolute value of the correlation between simulated AMOC and the Northeast/Southeast sea level composite from the absolute value of the correlation between simulated AMOC and circulation index on decadal and interannual timescales respectively, for (a) the Northeast on interannual timescales, (b) the Southeast on interannual timescales, (c) the Northeast on decadal timescales, and (d) the Southeast on decadal timescales. Note that figures (a), (b), (c) and (d) use different scales (predictive ability) on the y-axis.

The quite large consensus among the 42 CMIP5 models in producing a clear negative relationship between the North American northeast CSL variations and the AMOC along large latitudinal stretches of the North Atlantic on decadal timescales is important to highlight (*Figure 5.1b, 5.2b, 5.11b, 5.12c*). Strong AMOC-sea level connections are also found, but to a lesser degree, in Northeast sea levels on interannual timescales and in Southeast sea levels on decadal timescales. With this, however, it becomes vital to discuss why some models deviate from this pattern, what causes the differences in the Northeast versus Southeast AMOC correlations and to what extent observations agree with the CMIP5 output in that

decadal SSH variability in the Northeast region in particular is suited as a "proxy" for AMOC variability (*see discussion in Chapter 6*).

5.5 Comparison of modelled and observed AMOC/SL relationship

Next, I assess the observed relationship between the RAPID array at 26.5°N and 38 tide gauge records along the North American Atlantic coast, stretching from Key West, Florida to Rimouski, Canada, and discuss these results in relation to the simulated AMOC-CSL relationship examined in *Chapter 5.2-5.4*. On interannual timescales, correlation between RAPID and tide gauge data (*Figure 5.14a*) exhibits a distinct divide near Cape Hatteras (~tide gauge location 31, 35.1°N), with substantially stronger anticorrelations in the region between Cape Hatteras and Portland (location 6, 43.7°N), and very weak positive correlations for the region south of Cape Hatteras. There are also weak negative correlations in the region north of Portland. Similar pattern is detectable in the slopes from linear regression between RAPID and tide gauges, with a marked divide for locations north and south of Cape Hatteras (*Figure 5.14b*). A divide in slope magnitudes were also seen in several CMIP5 models (see *Figure 5.3a and 5.3b*).

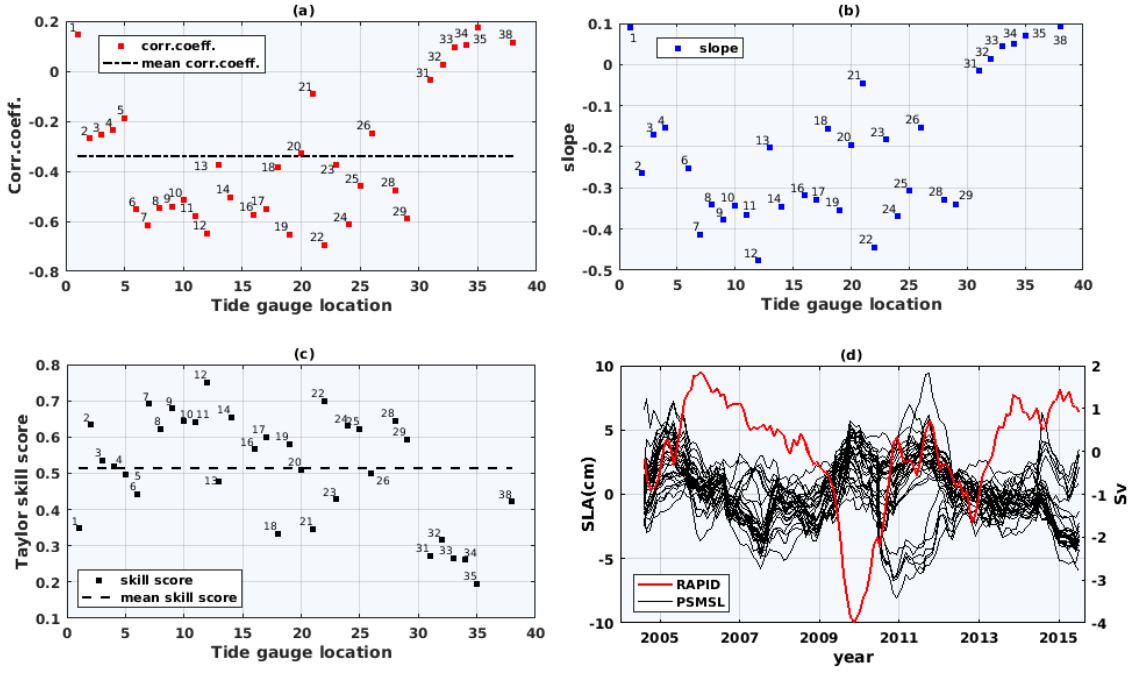

Figure 5.14. Comparison PSMSL tide gauge and RAPID observations 2004-2015 for 38 tide gauge locations along the U.S. east coast. Interannual variability. (a) correlation, (b) slope from linear regression (Sv/cm), (c) Taylor skill score, for RAPID observations at 26.5°N against 38 tide gauge sites, (d) actual time-series RAPID observations 26.5°N (red) and PSMSL tide gauges (black).

Taylor skill score further emphasises the divide in the nature of the RAPID-tide gauge relationship at Cape Hatteras, with larger agreement between the AMOC and sea level observations north of Cape Hatteras than south by the means of correlation and standard deviation. Moreover, timeseries of the RAPID and PSMSL data (*Figure 5.14d and 5.15*) directly display the inverse nature of the relationship. Notably, the tide gauge and RAPID data mimic the finding of a strong AMOC-coastal sea level antiphase during 2009-2010 in Goddard et al. (2015). The extreme 2009-2010 interannual event of sea level rise has been linked to an observed 30 per cent decline in the AMOC and to a strong negative North Atlantic Oscillation index (Goddard et al. 2015).

It should be noted that the sources of errors in *Figure 5.14* are not graphically represented in the plot, however, there is uncertainty associated with the experimentally determined values. Important sources of uncertainty with respect to the representation of the observed AMOC-CSL connection include different temporal length of the tide gauge records, non-uniform distribution of tide gauge sites latitudinally, the underrepresentation of tide gauge stations south compared to north of Cape Hatteras (~35°N), and the extent of missing values in the tide gauge records. In addition, the RAPID data only covers 15-years (at the time of analysis), which is a limited temporal period compared to that available for the tide gauge records (~100 years). Of particular concern is the fact that the tide gauges with shorter length or with many missing values may not register some important anomalies over the last decades, and therefore their correlation values may be non-comparable in relation to those with longer periods of record.

Whilst the linear regression analysis for the simulated data covers a much longer historical period (1920-2006) compared to the observational records (2004-2015), it is notable that some CMIP5 models produce a divide in behaviour near Cape Hatteras similar to observations, both with respect to slopes from linear regression (*Figure 5.3*) and correlation analyses (*Figure 5.1*). Importantly, however, comparing the observed versus the simulated AMOC-sea level correlation directly is not necessarily reliable, as the temporal dimensions differ. Not to mention, the observational record of the AMOC is too short to evaluate decadal variability, and it is for decadal variability that the AMOC-sea level antiphase is the strongest for a majority of models.

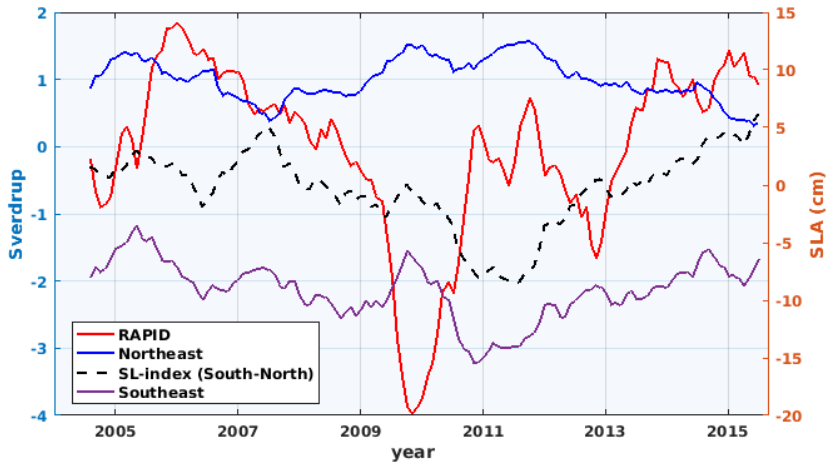

Figure 5.15. Interannual variability 2004-2015 for RAPID observations at 26.5°N (red line), Northeast composite (blue line), Southeast composite (purple line) and tide gauge-based AMOC-index (black dotted line). The Northeast composite is defined as 30 tide gauge locations north of Cape Hatteras (35.1°N). The Southeast composite is defined as tide gauge locations south of Cape Hatteras. The tide gauge-based AMOC index is defined as the Southern minus the Northern composite.

Interestingly, the modelled versus observed AMOC-sea level relationships exhibit contrasting behaviour with respect to the SSH-based circulation index based on coastal sea level composites on either side of 35°N. Particularly, while the index is more dominated by the Southern component than the Northern in the tide gauge data (*Figure 5.15*), the opposite is the case for the CMIP5 models, where the Northern sea level component dominates (*Figure 5.8 and 5.9*). At a glance and at least from the limited observational record available, this indicates that the CMIP5 models tend to overestimate the amplitude of sea level variability north of 35°N and the Northern dominance in a sea level index, as compared to observations. Correspondingly, the CMIP5 models tend to underestimate the amplitude of Southeast sea level variations and its dominance in the alongshore index. Yet, given the short RAPID record, caution should still be exercised when comparing the index behaviour in models against observations.

5.6 Stability of relationship during global warming

This chapter aims to explore the stability of the AMOC-dynamic sea level relationship during global warming with respect to interannual and decadal timescales along the North American east coast from year 2000 to 2300. In this context, "stability" refers to the extent to which the projections indicate an antiphase nature of the AMOC-sea level relationship that is spatially and temporally coherent, as seen in several CMIP5 models for historical runs (see *Figure 5.1 and 5.11*). For projections over the period 2006-2300, the r1i1p1 experiment is analysed for each CMIP5 model forced under RCP2.6 and RCP8.5. The maximum available model runs are selected. Moreover, when the four centuries (1900-2300) are compared, each 100-year period is detrended separately so that only variability within one century is considered.

The 21st century projections of the AMOC-sea level relationship under both RCP2.6 (*Figure 5.16a and 5.17a*) and RCP8.5 forcing scenarios (*Figure 5.16b and 5.17b*) show that the majority of models agree on the anti-phase nature of the AMOC-CSL relationship, although the magnitude of the inverse relationship varies between models, on both interannual and decadal timescales. About half of the available models exhibit moderate to strong anticorrelations (<-0.5) between the AMOC and dynamic CSL, for both RCP2.6 and RCP8.5 on decadal timescales (*Figure 5.17a and 5.17b*), while approximately one-fourth of the models generate such strength of the relationship on interannual timescales (*Figure 5.16a and 5.16b*). The mean correlations, averaged across all models and spatially, are -0.5578 under RCP2.6 and -0.3814 under RCP8.5 for decadal variability, with positive correlations obtained by only one model under RCP2.6 and three models under RCP8.5.

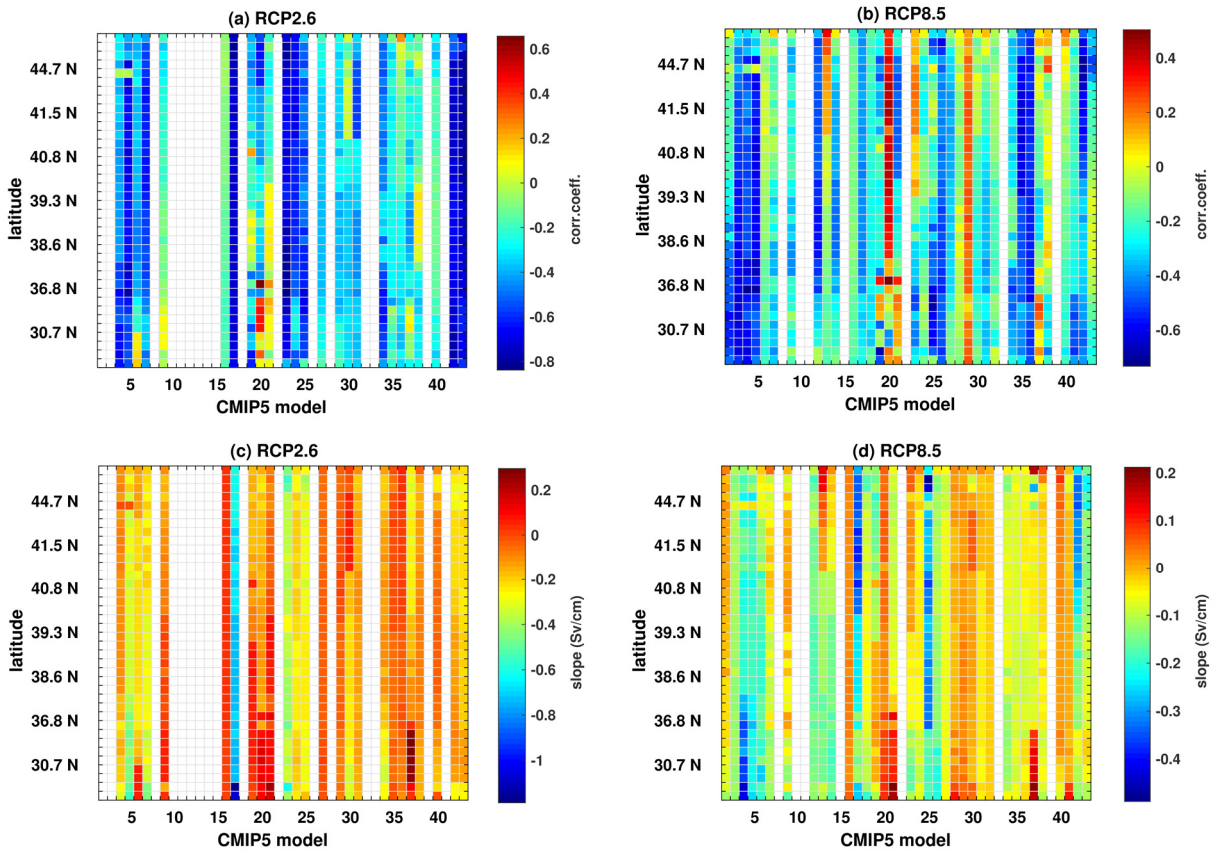

Figure 5.16. Simulations (2000-2100) of the relation between AMOC and coastal sea level, interannual variability. Future runs are merged with historical runs for the period 2000-2006. Grey columns indicate unavailable model simulations. Correlation between simulated AMOC against SSH for (a) RCP2.6, and (b) RCP8.5. Slope from linear regression model relating simulated AMOC to coastal sea level variability for (a) RCP2.6, and (d) RCP8.5. Note that figures (a), (b), (c) and (d) use different colour scales.

Noticeably, a similar overall CMIP5 model pattern is seen in the historical simulations of the relationship (*see Figure 5.1 and 5.3*). The models generating anticorrelations in historical simulations tend to be the same models obtaining an inverse AMOC-CSL relationship in the 21st projections, despite some exceptions. For example, CSIRO-Mk3-6-0(16) exhibits a negative nature of the relationship in the 21st century projections, but a positive nature that deviates from the large majority of models in the 20th century simulations. Not to mention, similar to historical simulations, moderate to strong AMOC-CSL anticorrelations (<-0.5) are present in a larger number of models on decadal compared to interannual timescales.

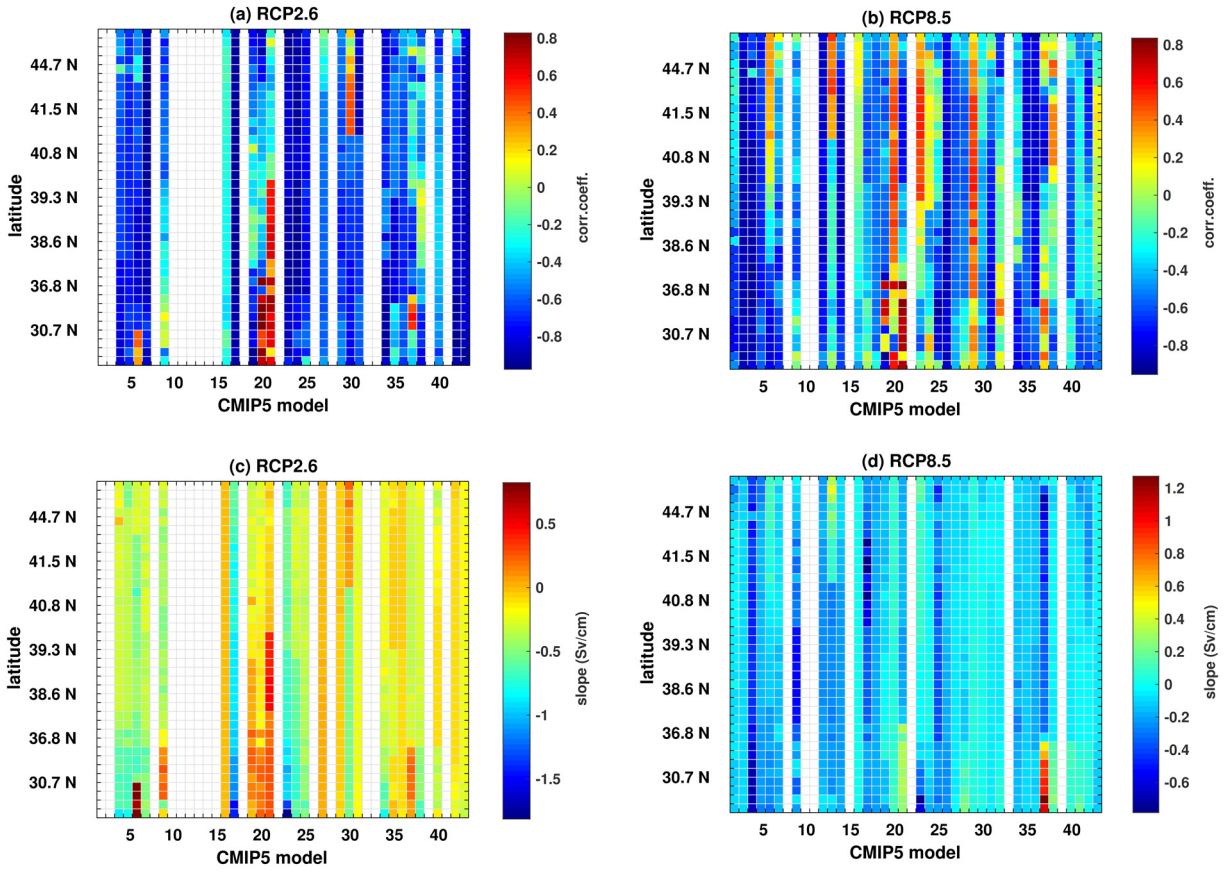

Figure 5.17. Simulations (2000-2100) of the relation between AMOC and coastal sea level, decadal variability. Future runs are merged with historical runs for the period 2000-2006. Grey columns indicate unavailable model simulations. Correlation between simulated AMOC against SSH for (a) RCP2.6, and (b) RCP8.5. Slope from linear regression model relating simulated AMOC to coastal sea level variability for (a) RCP2.6, and (d) RCP8.5. Note that figures (a), (b), (c) and (d) use different colour scales.

About half of the models generate weak negative scaling coefficients from linear regression (*Figure 5.16c, 5.16d, 5.17c, 5.17d*), with about one-fourth of models obtaining scaling coefficients between ~-0.5 and -0.2 Sv/cm, regardless of timescale and forcing scenario. The number of models obtaining negative scaling coefficients is quite similar to the historical simulations (*Figure 5.3*). While five AOGCMs produce negative slopes of ~-0.5 Sv/cm along some or large coastal stretches for RCP2.6 (CanESM2(5), CESM1-CAM5(8), CSIRO-Mk3-6-0(16), GFDL-CM3(22) and IPSL-CM5A-LR(29)) and RCP8.5 (bcc-csm1-1(3), CESM1-CAM5(8), CSIRO-Mk3-6-0(16), GFDL-ESM2M(24) and MPI-ESM-LR(36)) on decadal timescales, only CSIRO-Mk3-6-0(16) and GFDL-ESM2M(24) do the same on interannual timescales. These models indicate that a positive (negative) sea level anomaly of 2 cm corresponds to a 1 Sv reduction (increase) in AMOC transport. This quantified relationship quite closely coincides with the AMOC-CSL connection detected in the OCCAM ocean model in Bingham and Hughes (2009) for the historical period 1986-2004 (see *Figure 2* in

Bingham and Hughes 2009) as well as in some models for historical simulations (1920-2006) (*Figure 5.3*).

There are generally few differences in model behaviour between RCP2.6 and RCP8.5 for a single timescale (interannual or decadal) over the 21st century. The models that exhibit moderate to strong anticorrelations tend to be the same across the RCP2.6 and RCP8.5 pathways. The same applies for the models obtaining negative scaling coefficients from linear regression between ~-0.5 and -0.2 Sv/cm. Yet, it should be noted that some additional models (~4 models) under RCP8.5 (*Figure 5.17d*) exhibit no significant relationship compared to under RCP2.5 on decadal timescales (*Figure 5.17c*).

While the majority of models agree on the anti-phase nature of the AMOC-sea level relationship over the 21st century under both forcing scenarios and on both timescales, with particularly strong anticorrelations noted on decadal timescales (*Figure 5.16 and 5.17*), an interesting pattern emerges if extending the analysis up to year 2300. Particularly, if dividing the period 1900-2300 into four 100-yr intervals, it is clear that the models exhibit a relatively large intra- and inter-model spread in correlation and linear regression values over the four different centuries (*Figure 5.18 and 5.19*). That is, even though a large majority of models show negative correlations and regression slopes for both RCP2.6 and RCP8.5 and for both interannual (*Figure 5.18*) and decadal (*Figure 5.19*) variability, the magnitudes vary considerably among models within a century as well as for a single model between the different 100-yr periods. The largest intra-model spread noted for a single model (CSIRO-Mk3-6-0(16)) ranges from ~0.37 (interval 1900-1999) to -0.95 (interval 2000-2099). Noticeably, these initial results indicate that the AMOC-sea level relationship may not be stationary, and very dependent on the temporal period examined. Nevertheless, the overall mean (mean of model means) for each 100-yr period does not vary considerably (*Table 5.1 and 5.2*), thus questioning why the CMIP5 models show such differences.

For some models, the intra-model spread across centuries is quite profound. For example, on interannual timescales under RCP2.6, CCSM4(6) produces an AMOC-CSL correlation of ~-0.14 for the 20th century and ~-0.55 for the 21st century, and CSIRO-MK3-6-0(16) generates a correlation of ~0 (no significant relationship) for the 20th century and ~-0.75 for the 21st century (*Figure 5.18a*). On decadal timescales under RCP8.5, bcc-csm1-1(3) obtains no significant correlation for the 20th century, but a correlation of ~-0.5 for the 23rd century (*Figure 5.19b*). Large intra-model differences are also present for several models in slopes from linear regression (*Figure 5.18c-d, 5.19c-d*). Yet, it should be noted that the degree of intra-model spread over the 20th-23rd centuries varies between CMIP5 models.

The largest inter-model spread in correlations on both interannual and decadal timescales are found during 2000-2099 for both forcing scenarios, with values ranging from -0.75(CSIRO-Mk3-6-0(16)) to -0.05(FIO-ESM(20)) for RCP2.6 and -0.57(MIROC-ESM(35)) to 0.23(FGOALS-s2(19)) for RCP8.5 for interannual variability, and from -0.94 (CSIRO-Mk3-6-0(16)) to 0.2(FIO-ESM(20)) for RCP2.6, and -0.85(ACCESS1-3(2)) to 0.38(HadGEM2-ES(28)) for RCP8.5. The inter-model spread is also large for the historical period. For the limited number of models available for the 22nd and 23rd centuries, the inter-model differences do not appear as large compared to the 20th and 21st centuries, especially if considering interannual timescales.

There is a larger number of models that exhibit strong anticorrelations (<-0.5) on decadal compared to interannual timescales for all four centuries. Several models show anticorrelations equal to or stronger than -0.75 for decadal variability (17 models for RCP2.6 and 19 models for RCP8.5), which is a substantially larger number than for interannual variability, whereby 4 models show such magnitudes for RCP2.6 only. The inter-model spread is generally smaller for slopes from linear regression compared to correlations on interannual timescales (*Figure 5.18c, 5.18d)*.

Ignoring individual model differences, an unweighted mean of model means shows that, accumulated, the CMIP5 models generate negative correlations for all four centuries. The strongest negative AMOC-CSL relationships are obtained by decadal correlation values under RCP2.6 (*Table 5.1*). The mean regression slope values are weak negative across all centuries (*Table 5.2*). Importantly, although the mean values in *Table 5.1 and 5.2* emphasise that the CMIP5 models aggregately project an inverse nature of the AMOC-CSL relationship over the next centuries, such averaging ignores any spatial and intra- and inter-model differences, and should be interpreted with caution.

Overall, given the absolute dominance of negative values (though with varying strength) in the mean of model means (*Table 5.1 and 5.2*) as well as the fact that a large majority of individual models produce anticorrelations for all four centuries (1900-2300), it seems plausible to argue that the CMIP5 models generally agree on the anti-phase nature of the AMOC-sea level relationship in future projections along the North American east coast. Still, the models disagree on the exact magnitude of the relationship, for which relatively large intra- and inter-model differences prevail. While recognising the speculative nature of these preliminary results, the differences between models and for a single model between different centuries suggest a potential non-stationary AMOC-CSL relationship that is very dependent on the temporal period examined. While it would be interesting to examine the potential

underlying causes behind these inter-model and intra-model differences, it is beyond the scope of this project to do so, leaving this question open for future research.

Yet, it should be underlined that the potential non-stationary AMOC-CSL relationship presented here under RCP2.6 and RCP8.5 scenarios accounts for the r1i1p1 ensemble only. Since both AMOC and CSL considers just the first realisation, it is not possible to compare the potential existence of different AMOC-CSL relationships that might be occurring in different ensemble members run over the same century. In fact, the extent to which the AMOC-CSL linkage is non-stationary in other ensemble members cannot be tested without having both AMOC and CSL from all members. In addition, to improve our knowledge of the potential non-stationary nature of the relationship, more sophisticated statistical methods should be applied, for example wavelet analysis. Any further analysis may also investigate the relationship under RCP4.5 and RCP6.0 scenarios. Importantly, ignoring any time-variant behaviour in future the AMOC-CSL relationship could result in poor coastal planning, and socioeconomic consequences for coastal communities affected by changing sea levels.

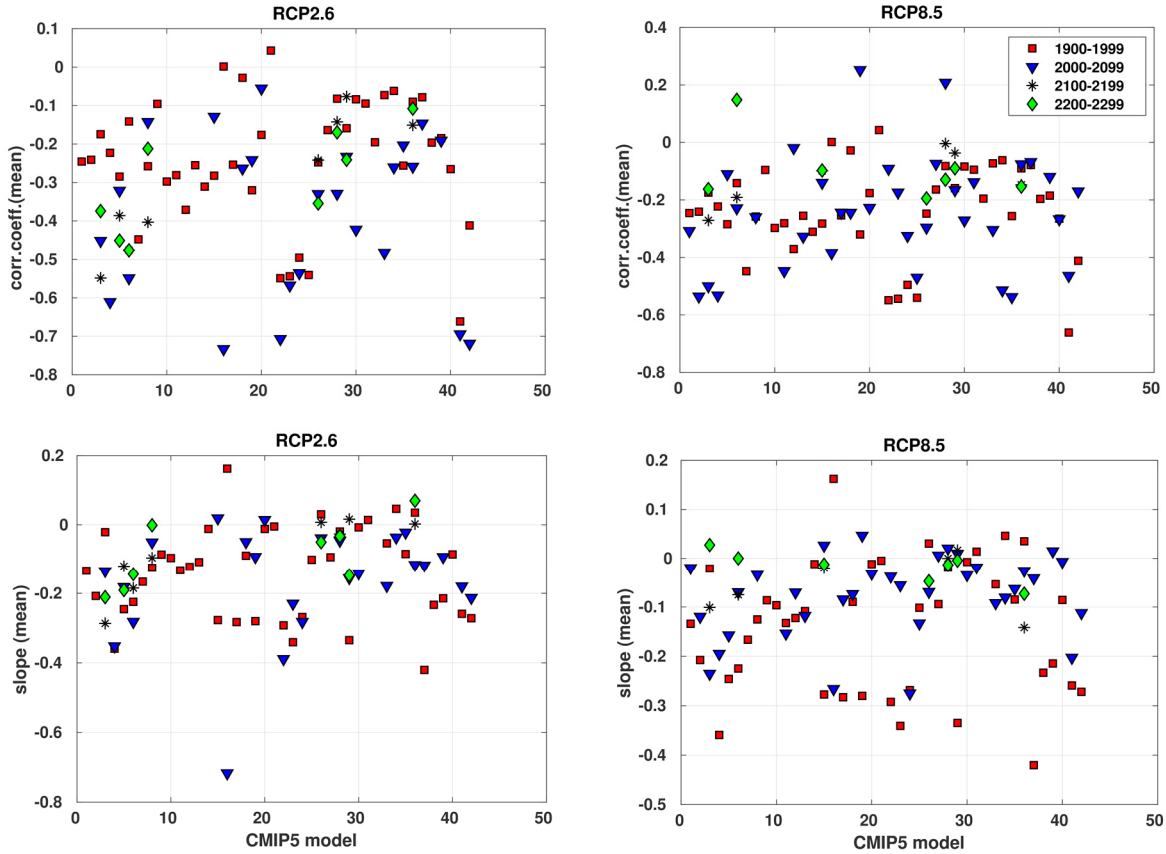

Figure 5.18. Simulations of the AMOC-sea level relation in CMIP5 for interannual variability during 1900-2300 for 100-yr intervals (1900-1999, 2000-2099, 2100-2099 and 2200-2299) under RCP2.6 (left) and RCP8.5 (right). Correlation AMOC against SSH for (a) RCP2.6 and (b) RCP8.5. Slope (Sv/cm) from linear regression for (c) RCP2.6 and (d) RCP8.5. Note that figures (a), (b), (c) and (d) use different scales on the y-axis.

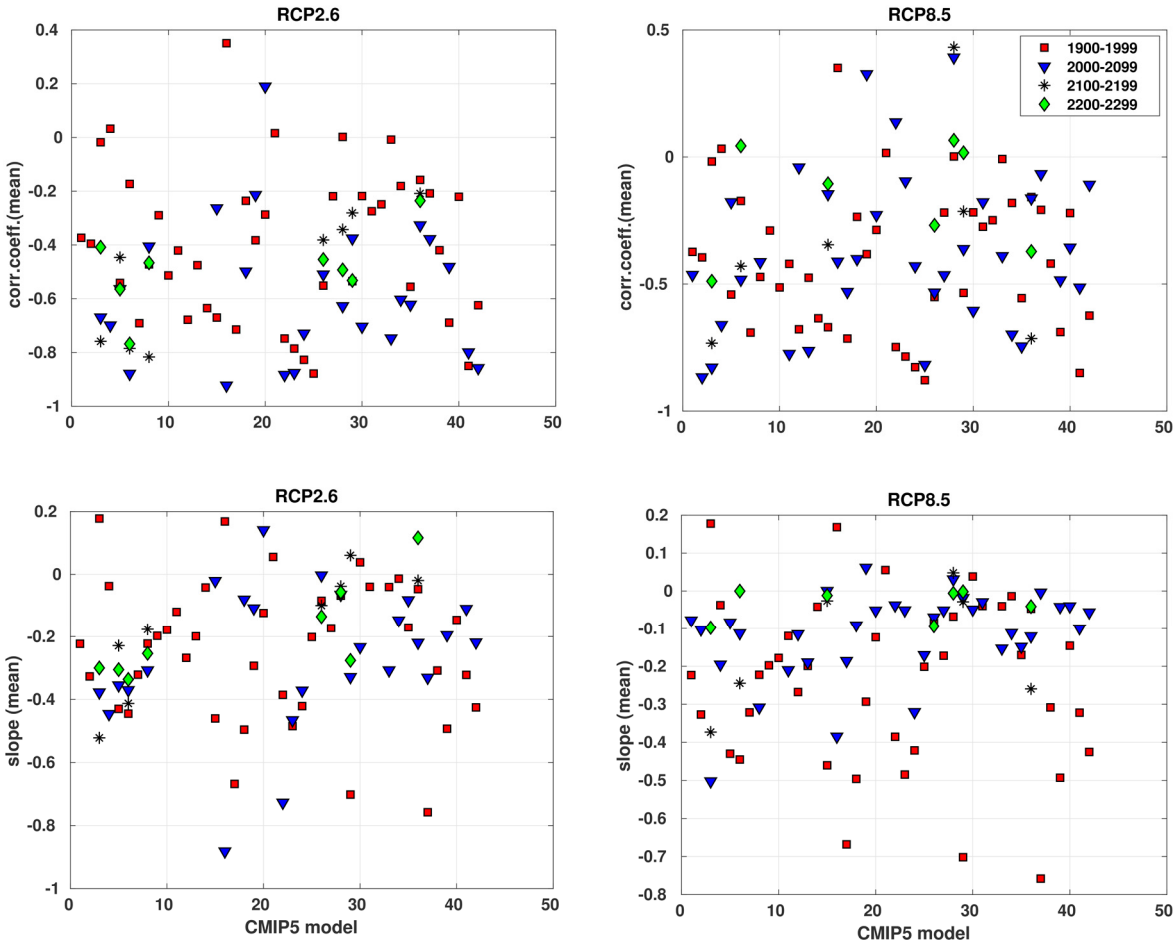

Figure 5.19. Simulations of the AMOC-sea level relation in CMIP5 for decadal variability during 1900-2300 for 100-yr intervals (1900-1999, 2000-2099, 2100-2099 and 2200-2299) under RCP2.6 (left) and RCP8.5 (right). Correlation AMOC against SSH for (a) RCP2.6 and (b) RCP8.5. Slope (Sv/cm) from linear regression for (c) RCP2.6 and (d) RCP8.5. Note that figures (a), (b), (c) and (d) use different scales on the y-axis.

Given the inter-model spread characterising the representation of the AMOC-CSL relationship in this study, as well as the model differences in capturing the observed AMOC and sea level variability respectively, excluding or weighting models may offer advantages by reducing model uncertainty and obtaining more probabilistically reliable projections (Hawkins and Sutton 2009, Knutti et al. 2017). Although the idea of "model democracy" (Knutti 2010) has been challenged by various methods aimed at weighted multi-model ensembles, there is no explicit agreement on how such weights should be obtained.

One approach could be to calculate the distance between each model and observations, and between the respective models, thereby targeting model performance and interdependencies (Knutti et al. 2017). If applying such a scheme, IPSL-CM5B-LR should be excluded because it consistently generates among the largest distances to observations. In addition, IPSL-CM5B-LR exhibits a very weak overturning circulation and hence no clear streamfunction (*Figure 4.1)* and can therefore not be trusted for future scenarios. Other models that do not capture observations well, and therefore should be given less weight, include CESM1-FASTCHEM, NorESM1-M and GFDL-CM2p1. Moreover, models that largely duplicate other models may be given less weight. For example, CCSM4 and CESM1-BGC obtain very similar SSH cross-correlation results (these have same ocean, atmosphere and sea ice model). Furthermore, models that largely deviates from the large majority or perform a case of unexpected or erroneous behaviour should be excluded or given less weight. For example, HadGEM2-CC and IPSL-CM5B-LR exhibit a much larger latitudinal spread in sea level variance compared to the remaining of models (*Figure 4.7*), and CSIRO-Mk3-6-0 and GFDL-CM2p1 generate positive AMOC-CSL correlation values along most of the North American east coast, which stands in contrast to the remaining models' anti-phase nature (*Figure 5.1*).

Importantly, it should be noted that weighted multi-model ensembles do not necessarily offer significant advantages or reasonable quantifications over the equal weighted method, with the latter potentially offering more transparency (Weigel et al. 2010). In the present study, the objective of assessing the AMOC-CSL relationship in as many ensembles as possible, exceeds any goal of obtaining "optimium weighted" multi-model ensemble projections. Yet, future work examining the degree of stationarity in the AMOC-CSL relationship may possibly find advantageous weighting schemes that justifies forsaking strict "model democracy".

	Interannual		Decadal	
	RCP2.6 corr.coeff.(mean)	RCP8.5 corr.coeff.(mean)	RCP2.6 corr.coeff.(mean)	RCP8.5 corr.coeff.(mean)
1900-1999	**-0.2399**	**-0.2399**	**-0.3990**	**-0.3990**
2000-2099	**-0.3832**	**-0.1856**	**-0.5778**	**-0.3814**
2100-2199	**-0.3033**	**-0.1249**	**-0.5024**	**-0.3341**
2200-2299	**-0.2984**	**-0.0971**	**-0.4901**	**-0.1584**

Table 5.1. Overall (CMIP5 ensemble) mean correlation values (mean of model means derived from model values in *Figure 5.18 and 5.19*) for a single 100-year period.

	Interannual		Decadal	
	RCP2.6 slope(mean)	RCP8.5 slope(mean)	RCP2.6 slope(mean)	RCP8.5 slope(mean)
1900-1999	**-0.1401**	**-0.1401**	**-0.2413**	**-0.2413**
2000-2099	**-0.1627**	**-0.0787**	**-0.2645**	**-0.1168**
2100-2199	**-0.0861**	**-0.0535**	**-0.1795**	**-0.1474**
2200-2299	**-0.0886**	**-0.0207**	**-0.1934**	**-0.0419**

Table 5.2. Overall (CMIP5 ensemble) mean slope values (Sv/cm) from linear regression (mean of model means derived from model values *Figure 5.18 and 5.19*) for a single 100-year period.

5.7 Summary

In this chapter, the AMOC-CSL relationship has been examined in 42 CMIP5 models for the historical period 1920-2006 from two different approaches: 1) the direct relationship, including a comparison between initial AMOC simulations and a SSH-based reconstruction of the AMOC derived from linear regression, and 2) calculating and testing a circulation index based on alongshore CSL composites on either side of 35°N. The most striking finding is the moderate to strong anticorrelations (<-0.5) between AMOC and CSL on decadal timescales, particularly between ~35°N-60°N, demonstrated in approximately half of the CMIP5 models (22 ±4). Strong AMOC-CSL anti-phases are also seen on interannual timescales, particularly north of Cape Hatteras, but the number of models exhibiting such a relationship on interannual timescales is modest (about one-quarter of models) compared to

decadal analysis and the strength of the relationship is generally weaker. The remaining models typically exhibit weaker negative correlations, with only a minority of models generating positive correlations.

About three-quarters of models obtain regression slopes between ~-0.1 to -0.35 Sv/cm on interannual timescales, and about three-quarters generate scaling coefficients ranging from ~-0.3 to -0.8 Sv/cm on decadal timescales, whereby about one-third produce a relationship close to -0.5 Sv/cm, which is not too different from Bingham and Hughes' (2009) slope of ~-0.59 Sv/cm.

Building further on McCarthy et al.'s (2015) concept of a circulation index based on alongshore sea level composites on either side of Cape Hatteras, *Chapter 5.4* has assessed the applicability of such an index in the CMIP5 simulations by testing the potential added predictive value of adding the Southern CSL component into the index versus just the Northern composite. The analysis shows that the positive contribution of the index depends on what timescales and latitudes are being considered. Including the Southern component in the index adds predictive value as an AMOC proxy only on interannual timescales at certain latitudinal stretches (north of ~60°N as seen in ~34 models, and south of ~20°N in ~10 models), but not on decadal timescales, where most of the predictive power comes from the Northern sea level component, as seen in about two-thirds of models. Because the Northern composite's outperforming of the index on decadal timescales closely mimics the results from direct AMOC-CSL anticorrelations (*Figure 5.1*), the McCarthy et al. (2015)-inspired index is not particularly useful in the CMIP5 ensemble.

Similar to historical simulations, about half of the available CMIP5 models obtain moderate to strong AMOC-CSL anticorrelations (<-0.5) over the 21st century under both RCP2.6 and RCP8.5 on decadal timescales. About one-fourth of models obtain negative correlations of order <-0.5 on interannual timescales. If extending the analysis up to the 23rd century, the models exhibit a noticeable intra-model spread in correlation and linear regression values over the different centuries respectively, questioning the AMOC-sea level relationship's stationarity and temporal dependence.

Overall, the results demonstrate that sea level along the northeast North American coast is likely primarily driven by, or at least associated with, AMOC variability on decadal timescales.

6 Discussion

6.1 Summary

In the present study, about half of the CMIP5 models (22 ±4) exhibit moderate to strong anticorrelations (<-0.5) between AMOC and sea level variability along the North American northeast coast on decadal timescales. That such a number of coupled models demonstrate a clear anti-phase nature of the relationship is important in the context that several recent analyses exclude any dominating role of the AMOC in influencing CSL variability along the U.S. east coast on this timescale (see Andres et al. 2013, Li et al. 2014, Woodworth et al. 2014, Piecuch et al. 2016, Little et al. 2017).

The first aim of this investigation was to assess the representation of the AMOC in the CMIP5 models. The results show that, while many models agree on several features of the spatiotemporal characteristics of the AMOC, there is still substantial inter-model spread. This is especially the case if considering the magnitude of transport strength and dominant mode of variability when the northward transport anomaly is assessed as a function of time and latitude. Moreover, about half of the models exhibit a similar spatial pattern with discontinuity in interannual AMOC variations at ~40°N, as seen in Bingham et al. (2007). Comparing the AMOC simulations with RAPID observations, relatively large model disagreement dominates the mean AMOC strength and standard deviation for interannual variability. Four model families (ACCESS1, CESM1, GFDL, except GFDL-CM2p1, and MPI) obtain mean AMOC strength values very close to the RAPID 2004-2015 mean (~17.3 Sv), whereas the majority of models exhibit a mean strength between ~12.5-19 Sv. Only two models (GFDL-ESM2M(24) and MPI-ESM-MR(37)) produce standard deviations of interannual AMOC variability that is very close to the RAPID value (~1.3 Sv), with the remaining models underestimating the observed amplitude of interannual AMOC variations to varying degree (~0.25 to 1.07 Sv standard deviation). The models also generally underestimate the RAPID trend magnitude.

The second objective was to assess the spatial and temporal representation of observed CSL in CMIP5 models. Results show that close to all CMIP5 models underestimate the tide gauge variance along the North American east coast on both interannual (40 out of 42 models) and decadal timescales (38 out of 42 models) (*Figure 4.7*). The underestimation of the tide gauge variance is generally larger south of ~35°N compared to the region north of this latitude (*Figure 4.8*). This suggests that the models fail to capture the temporal sea level changes and that the AOGCMs may not reproduce the full range of potential CSL changes. The systematic CMIP5 underestimation of the tide gauge variance is in line with previous studies (e.g. Peyser

and Yin 2017, Meyssignac et al. 2017). Spatially, however, about half of the models capture the distinct spatial characteristic of CSL variability on either side of Cape Hatteras (35°N), as seen in tide gauges (*Figure 4.9*). Particularly, cross-correlations for sites on the same side of 35°N, either north or south, is very high and coherent, but is substantially lower for sites on different sides of 35°N. Although this spatial cross-correlation pattern is in agreement with previous analyses (Woodworth et al. 2014, McCarthy et al. 2015, Little et al. 2017), these studies limit the assessment to a single CMIP5 model (Little et al. 2017), tide gauge data only (McCarthy et al. 2015), or a combination of tide gauges, satellite altimetry and a single ocean model (Woodworth et al. 2014).

The third objective required an exploration of the spatial and temporal characteristics of the AMOC-sea level relationship in CMIP5 models for the historical record (1920-2005) from two different approaches. The most striking result is the moderate to strong anticorrelations (<-0.5) obtained between AMOC and CSL on decadal timescales between ~35°N–60°N, demonstrated in about half of the models. This finding is prominent both in direct correlations and indirectly when correlating initial AMOC simulations with either the SSH-based circulation index based on CSL composites on either side of 35°N, or the SSH-based AMOC reconstruction derived from linear regression. AMOC-CSL anti-phases are also seen on interannual timescales, but the number of models generating a negative relationship is modest (~one-fourth of models obtaining correlations <-0.5) compared to decadal analysis. In addition, there are more models producing positive correlations on interannual (~8 models) versus decadal timescales (~4 models). In direct correlations, the mean AMOC-CSL correlation on decadal timescales, averaged across all models and coastal sites, is -0.3966, with 21 CMIP5 models exhibiting a mean (spatial) anticorrelation of <-0.5. On interannual timescales, the mean correlation is -0.2357, with only three models obtaining mean (spatial) anticorrelations of <-0.5.

Assessment of reconstructed AMOC from a linear regression model relating simulated SSH variations to AMOC, emphasises the clear anti-phase nature of the AMOC-CSL relationship found in direct correlations for approximately half of the models on decadal timescales. On interannual timescales a majority of models (~three-quarters) obtain slopes between ~-0.1 to -0.35 Sv/cm. The negative slopes are generally stronger on decadal timescales, ranging from ~-0.3 to -0.8 Sv/cm for a majority of models (~three-quarters), whereby about one-third produce a relationship close to -0.5 Sv/cm, which is not too different from Bingham and Hughes' (2009) slope of ~-0.59 Sv/cm. Approximately two-fifths of AOGCMs exhibit decadal slope values that are in line with the scaling coefficients of order -1 to -2 cm/Sv recently noted in Little et al. (2019) as a diagnostic of the geostrophic AMOC-CSL relation.

Noticeably, some AOGCMs (~11 models) show weaker negative slopes for the coastal coordinates south of 35°N compared to the northern counterpart.

Testing the McCarthy et al. (2015)-inspired SSH-based circulation index based on alongshore CSL composites, by quantifying the potential added predictive value of including the Southern sea level component as part of the index versus just the Northern composite, it is clear that the positive contribution of the alongshore index depends on what timescales and latitudes are being considered. The inclusion of the Southern component in the circulation index may add limited predictive value as an AMOC proxy on interannual timescales at certain latitudinal stretches (especially north of ~60°N as seen in ~34 models, and south of ~20°N in ~10 models), but not on decadal timescales, where most of the predictive power derives from the Northern sea level component. Since the Northern composite's outperforming of the index on decadal timescales closely mimics the moderate to strong AMOC-CSL anticorrelations revealed in direct correlations (*Figure 5.1*), the McCarthy et al. (2015)-inspired index exhibits no clear usefulness in the CMIP5 ensemble. Rather, a single composite of CSL between ~35°N-48°N stands out as an applicable AMOC proxy on decadal timescales.

The last objective was to investigate the stability of the AMOC-CSL relationship during global warming over the 21st, 22nd and 23rd centuries under the RCP2.5 and RCP8.5 pathways. Similar to historical simulations, about half of the available CMIP5 models obtain moderate to strong AMOC-CSL anticorrelations (<-0.5) over the 21st century under both RCP2.6 and RCP8.5 on decadal timescales. About one-fourth of models obtain negative correlations of order <-0.5 on interannual timescales. The mean correlations, averaged across all models and spatially, are -0.5578 under RCP2.6 and -0.3814 under RCP8.5 for decadal variability, with positive correlations obtained by only one model under RCP2.6 and three models under RCP8.5. If extending the analysis up to the 23rd century, the models exhibit a noticeable intra-model spread (with the maximum intra-model correlation spread noted for a single model (CSIRO-Mk3-6-0) ranging from ~0.37 to -0.95) in correlation and linear regression values over the 20th, 21st, 22nd and 23rd centuries respectively. The intra-model spread is questioning the future AMOC-CSL relationship's stationarity and temporal dependence. Nevertheless, even though the models exhibit intra-model spread and disagree on the exact strength of the relationship over the next centuries, the majority of CMIP5 AOGCMs agree on an anti-phase nature of the future AMOC-CSL connection, and therefore also support the anti-phase dominated result in historical simulations, especially on decadal timescales, highlighting a case of decadal climate predictability.

6.2 Sea level as a tool to monitor AMOC

In the present study, the majority of CMIP5 models exhibit an anti-phase nature between AMOC and sea level variability along the North American east coast on both interannual and decadal timescales, with particularly strong anticorrelations (<-0.5) on decadal timescales north of Cape Hatteras as seen in about half of the models. The negative relationship is prominent in both historical and future simulations and is detected in both direct correlations, and indirectly via testing of the SSH-based circulation index and reconstruction of AMOC strength from a linear regression model relating AMOC and CSL. However, the extent to which the inverse AMOC-CSL relationship, as indicated by multiple models, can be translated into the robustness of CSL-based AMOC proxies, depends on several factors.

Above all, the present study supports a case in which CSL variability along the North American northeast coast (~35°N-48°N) is likely primarily driven by, or at least associated with, AMOC variability on decadal timescales. While a strong inverse connection between AMOC and CSL along the U.S. east coast have been identified in previous studies on decadal timescales (e.g. Hakkinen 2001, Ezer 1999, 2001, Sweet et al. 2009, McCarthy et al. 2015), the present study is the first to establish a clear anti-phase nature of the AMOC-CSL relationship on decadal timescales in a large number (>20) of CMIP5 models in both historical simulations and 21st century projections under two different representative concentration pathways. Consequently, this study's CMIP5 investigation defends the usefulness of AMOC proxies based on CSL variations between ~35°N-48°N along the North American east coast on decadal timescales. Ultimately, the present study challenges some recent analyses having found no significant relationship between AMOC and North American northeast CSL variations on decadal timescales (Woodworth et al. 2014, Little et al. 2017).

However, what is more uncertain is the connection between the AMOC and CSL on interannual timescales. While some studies highlight that AMOC and CSL are strongly negatively related on interannual timescales (e.g. Bingham and Hughes 2009, Goddard et al. 2015), other studies find little evidence of such coupling on interannual timescales (e.g. Woodworth et al. 2014, Little et al. 2017), and rather point at other dominating drivers of interannual CSL variations such as alongshore wind stress (Andres et al. 2013, Woodworth et al. 2014), or highlight a robust AMOC-CSL connection on multidecadal or longer timescales (e.g. Kopp 2013, Ezer 2013, Little et al. 2017). For example, Little et al. (2017) find that CSL variations north of 35°N are associated with AMOC strength on multidecadal to centennial timescales and that the AMOC-CSL coupling is largely externally forced, while processes unrelated to local winds and AMOC strength control Northeast CSL variability on interannual

to decadal timescales. The substantially smaller number of CMIP5 models exhibiting moderate to strong anticorrelations (<-0.5) on interannual compared to decadal timescales (~one-quarter versus half of models) in the present study adds to the already inconclusive evidence of interannual AMOC-CSL coupling along the U.S. east coast in existing studies.

Spatially, although a majority of CMIP5 models in the present study demonstrate a strong anti-phase nature between AMOC strength and northeast CSL variability (north of Cape Hatteras), it is still ambiguity related to the extent to which the AMOC also influence CSL variations south of Cape Hatteras, as also highlighted in previous analyses (e.g. Maul and Hanson 1991, Thompson and Mitchum 2014, Calafat et al. 2018). As noted in *Chapter 5.4,* the inclusion of the Southern composite as part of an alongshore SSH composite-based circulation index adds predictive power and outperforms the Northern composite alone only on interannual timescales along certain latitudinal stretches for some models, especially north of ~60°N as seen in ~34 models, and south of ~20°N in ~10 models. In contrast, the Northern component alone outperforms the index on decadal timescales in a majority of models (~27 models). Because the Northern component's dominance on decadal timescales essentially reflects the same result as the direct AMOC-CSL correlations in *Figure 5.1*, the SSH composite-based circulation index inspired by McCarthy et al. (2015) does not perform particularly well in CMIP5 models. Rather, a composite of CSL from Cape Hatteras to Rimouski (~35°N-48°N) captures the decadal variability of AMOC strength remarkably well, again highlighting the role of decadal northeast CSL variability as an important AMOC proxy and the uncertainty related to the AMOC's potential influence on CSL south of 35°N.

In some respects, a coupling between AMOC and CSL along the North American northeast coast on decadal timescales can possibly be argued to be more important than a coupling on interannual timescales. Particularly, since CMIP5 models demonstrate a strong decadal AMOC-CSL connection, CSL data can be used to infer decadal variations in AMOC strength, in the absence of longer observational records of the overturning circulation. In turn, evidence of an applicable decadal AMOC proxy, as demonstrated in the present study, can be a determining factor in separating internal variability from long-term secular trends in the AMOC. Importantly, early detection of a significant AMOC deceleration lies in enhanced understanding, and corresponding removal, of decadal (and multidecadal) variability (Visbeck 2014), which indirectly could be obtained via CSL data. This has again implications for timely and actionable predictions of associated regional climate impacts of AMOC changes, both from a decadal variability and long-term secular perspective.

Importantly, because the century-long PSMSL tide gauge records are still too short to offer potential reliable multidecadal to centennial AMOC proxies, the strong AMOC-CSL coupling on decadal timescales noted in the present study's CMIP5 assessment is not equivalent to concluding that the there is "no real evidence" for a long-term secular weakening of the AMOC under global warming (Parker and Ollier 2016). Simply, longer observational records are required to validate such statement. However, the decadal AMOC-CSL coupling can help us in the important continuous work of separating natural variations in climate from a long-term trend outside internal climate variability, in which the warming trend is superimposed on decadal accelerations and decelerations. In essence, from a climate-resilience perspective, decadal climate variability cannot be ignored and is to be expected (Visbeck 2014).

6.3 Assessment of CMIP5 models

Even though a majority of CMIP5 models show some common features, such as the general inverse nature of the AMOC-sea level relationship and underestimation of the magnitude of the tide gauge and RAPID variability, the individual models disagree on the detailed magnitude of the AMOC strength, the extent of meridional coherence and strength of the AMOC-CSL relationship, and the spatiotemporal characteristics of tide gauges. Below, some potential sources of the inter-model and model-observational discrepancies are highlighted. It is beyond the scope of this project to perform a detailed analysis of all possible sources and assess how much each source is responsible for a particular model result.

First, large inter-model spread is noted between the models obtaining strong AMOC-CSL anti-phases and those generating weak or positive relationships in historical simulations. The model families ACCESS1, CESM1 (except CESM1-FASTCHEM), CMCC, CNRM, GFDL (except GFDL-CM2p1) and NorESM1 generate strong anticorrelations (*Figure 5.1*) and negative scaling coefficients (*Figure 5.3*) on both interannual and decadal timescales. In contrast, the models CNRM-CM5-2(14), CSIRO-Mk3-6-0(16), GFDL-CM2p1(21), GISS-E2-R(26), HadGEM2-ES(28), IPSL-CM5A-MR(30), MIROC5(33), MPI-ESM-LR(36) and MPI-ESM-MR(37) exhibit weak negative or even positive AMOC-CSL relationships on both timescales. The remaining models exhibit either strong anti-phases on decadal but not interannual timescales, or moderate to weak negative relationships on both timescales.

There are several possible sources underlying these inter-model differences. First, it has been highlighted that the CMIP5 models, which are generally at relatively coarse resolution, may exhibit errors in the representation of CSL due to insufficient horizontal resolution (Higginson et al. 2015). In the present study, there seems to be some connection between the models obtaining strong negative (weak negative/positive) AMOC-CSL relationships and

high (lower) horizontal resolution of models. That is, the models that exhibit weaker negative or even positive AMOC-CSL relationships tend to have slightly lower horizontal resolution compared to the models generating strong anticorrelations or strong negative scaling coefficients. For example, the model families ACCESS1, CESM1, CNRM, FGOALS, GFDL (except GFDL-CM2p1) and NorESM1 obtain moderate to strong anticorrelations (<-0.5) on decadal timescales and are among the models with the highest horizontal resolution (*see Table 3.1*). The models CSIRO-Mk3-6-0(16), GFDL-CM2p1(21), GISS-E2-R(26), IPSL-CM5A-MR(30), IPSL-CM5B-LR(31), MIROC5(33), MIROC-ESM-CHEM(34), MPI-ESM-LR(36) generate weak negative or positive correlations along the coast and are among the models with lower-end resolution. Yet, there are exceptions to this. For example, this pattern cannot explain why GFDL-CM2p1 produce positive AMOC-CSL anticorrelations while the remaining member of its family (GFDL-CM3, GFDL-ESM2, GFDL-ESM2G) generate negative anticorrelations, despite all members having close to same horizontal resolution (~1.0° x 0.86/0.9°). In addition, a few models (CMCC model family) generate strong anticorrelations but are among the models with the lowest horizontal resolution (~1.98° x 1.21°). This reveals that horizontal resolution may only explain some of the inter-model spread.

A weaker but similar pattern applies for vertical resolution. The models generating strong negative (weak negative/positive) AMOC-CSL relationships tend to exhibit the highest (lowest) vertical resolution, but there are single-model exceptions to this. The major exception is the CMCC model family, which obtains relatively strong anticorrelations, but still exhibits lower-end vertical resolution (=31 vertical levels). Moreover, there is no clear pattern between the models generating strong inverse versus weak negative or positive AMOC-CSL relationships and what concerns horizontal (distorted, irregular) or vertical grid systems (z-level, sigma, isopycnal or hybrid). Although all model families generating strong anti-phases have distorted grids, the models producing weak or positive relationships have either distorted or irregular grids. Similarly, AOGCMs in both groups (strong negative versus weak relationships) have a combination of z-coordinate and hybrid systems (*Table S1*).

A potential source of the intra-model spread over the next centuries and general inter-model spread is the general uncertainty related to representation of AMOC in coupled climate models (Reintges et al. 2016). For example, uncertainty in AMOC projections may be associated with poor representation of the density structure of ocean, which in turn may be explained by uncertainties in salinity projections derived from uncertainties in freshwater flux and gyre-strength (Reintges et al. 2016). The gyre-strength projections are in turn related to biases of North Atlantic deep water formation via salt advection (Reintges et al. 2016, Heuze

2017). Interestingly, Heuze (2017) points out that deep convection is most realistic in CMIP5 models applying the CICE ice model, which in the present study includes the ACCESS1, CESM1 and NorESM1 model families, in addition to FIO-ESM and FGOALS-g2. These are all among the models generating moderate to strong inverse AMOC-CSL relationships. Some of the models obtaining strong inverse AMOC-CSL relationships are also built on the same ocean model, with ACCESS1 and GFDL (except GFDL-ESM2G) model families being based on the MOM4.1 ocean model. Still, although some models within a group of similar model behaviour share the same ice or ocean component, other models within the same group do not, and therefore this structural feature may only explain some of the similarities across the given models, not the overall inter-model spread.

Inter-model spread is also evident in the spatial characteristics of the AMOC-CSL relationship. A majority of models exhibit moderate to strong anticorrelations between the zonally integrated AMOC and CSL variability north of Cape Hatteras with weaker or even positive relationships south of Cape Hatteras (*Figure 5.11*). However, not all models simulate such a spatial pattern, but instead generate meridionally coherent anticorrelations that cross the boundary of Cape Hatteras, or no easily detectable spatial pattern. Notably, some of the models obtaining meridionally coherent anticorrelations (ACCESS1 and NorESM1 model families) are all built on the CICE ice module. Other potential explanations for this inter-model discrepancy are differences in AOGCM simulations of the forced response and unforced internal variability. The unforced internal variability may be associated with the North Atlantic Oscillation (NAO), Atlantic multidecadal oscillation (AMO) and El Nino-Southern Oscillation (ENSO) and is dominant on interannual to multi-decadal timescales, ultimately concealing some of the forced signal during the 20th century (Carson et al. 2015, Han et al.2016, Meyssignac et al. 2017). However, this study does not use dedicated regression techniques, EOF analysis, multi-model ensemble means, or other promising but disputable methods to estimate or isolate the unforced internal fluctuations and oscillations in coupled model simulations (Thompson et al. 2015). Consequently, a more systematic evaluation beyond the present study is needed to determine the degree to which unforced internal variability influence the inter-model differences.

Similar to the present study (*Figure 4.7 and 4.8*), earlier analyses also find that coupled models generally underestimate the magnitude of tide gauge variability along the North American east coast, particularly south of Cape Hatteras (e.g. Little et al. 2017, Minobe et al. 2017, Little et al. 2019). The general underestimation of the tide gauge variance along the North American east coast by CMIP5 models may be due to errors in representing shelf bathymetry because of insufficient horizontal and/or vertical resolution, unresolved

atmospheric forcing of the shelf and boundary conditions, such as freshwater inputs, and generally poor representation of physical processes in the shallow ocean (Higginson et al. 2015, Woodworth et al. 2012). The larger underestimation of the CSL variability south of 35°N may be reflected in this region's complex shelf bathymetry, interaction or unclear nature between the AMOC, the Gulf Stream, and the complex nature of the western boundary currents in this region (Joyce and Zhang 2010, Little et al. 2019). This calls for improvement of model resolution in the next generations of coupled models with a focus on improving horizontal and vertical resolution and resolving processes on the shelf.

Importantly, because the in-situ observations of continuous AMOC variability are temporally limited (~15 years), it is not yet possible to fully determine the extent to which the weaker negative or even positive correlations between AMOC strength and CSL south of Cape Hatteras is due to distinct physical dynamics different from the coastal region north of Cape Hatteras, or if these spatial characteristics can be traced to poor resolution and model representation of physical processes in the Southeast region. The former would support the general finding of stronger (weaker) anticorrelations north (south) of Cape Hatteras seen in several CMIP5 models (*Figure 5.1*) and in the observed RAPID-tide gauge relationship in this study (*Figure 5.14*).

As noted earlier, the majority of models show anticorrelations and negative regression slopes for both historical and future simulations (~1900-2300) on both interannual and decadal timescales, but with generally stronger inverse relationships on decadal timescales and north of Cape Hatteras. However, if assessing the AMOC-CSL connection separately for each of the three centuries during 2000-2300, the correlations and scaling coefficients appear remarkably variable for most models between the 21st, 22nd and 23rd centuries. That is, a single model shows quite different magnitudes of the AMOC-CSL strength for different 100-year periods. Besides model and scenario uncertainty (Little et al. 2015), a possible source of this potential non-stationary and temporal-dependency nature of the AMOC-CSL relationship in future projections is simply that there may be periods where the magnitude of the AMOC fluctuations are stronger and therefore have greater influence on CSL variations. Yet, it should be noted that the overall mean (mean of model means) for each 100-year period does not vary considerably (*Table 5.1 and 5.2*). This may support investigations using a multi-model ensemble mean as a complementary to individual coupled models in simulations of the future AMOC-CSL relationship.

6.4 Implications for future sea level

The clear decadal AMOC-CSL coupling demonstrated in CMIP5 models in the present study is particularly important for the heavily populated and socioeconomically vulnerable coastal communities along North American northeast coast. State-of-the-art climate models widely project that the northeast coast is subject to rapid sea level rise (SLR) over the 21st century (Yin et al. 2009, Church et al. 2013). The projected elevated SLR over the next century has traditionally been inextricably linked to a weakening of the AMOC, as suggested by several studies having assessed simulations forced by future radiative forcing scenarios, or freshwater inputs into the subpolar North Atlantic, or a combination of these (e.g. Levermann et al. 2005, Landerer et al. 2007, Hu et al. 2009, Pardaens et al. 2011, Hu et al. 2011, Kienert and Rahmstorf 2012, Chen et al. 2018). However, the clear decadal AMOC-CSL coupling demonstrated in the present CMIP5 study calls for a careful re-examination of any analysis strictly claiming an exceptional slowdown of the AMOC that exceeds the time window of interannual to multidecdal timescales (Roberts et al. 2014, Parker and Ollier 2016), or simply ignores the importance of understanding decadal climate variability (Visbeck 2014). In essence, in-situ continuous AMOC records are still too scarce temporally to appreciate any long-term secular trend cleared of multidecadal variability, and so is the AMOC's link to long-term secular sea level changes along the U.S. northeast coast.

Particularly, although several studies highlight an observed acceleration of sea levels along the North American northeast coast over the past decades (e.g. Boon 2012, Sallenger et al. 2012, Ezer 2013, Ezer and Atkinson 2014), strong decadal AMOC-CSL couplings challenge claims that the recent observed CSL acceleration must be due to anthropogenic causes and linked to a secular AMOC weakening. It is tempting to claim that the active research on the AMOC's potential secular influence on the Northeast CSL acceleration is plagued by a mix-up between "absence of evidence" and "evidence for absence" of a global-warming induced trend. In any case, a precautionary approach should be exercised because heightened coastal sea levels, whether derived from decadal accelerations (and decelerations) or a long-term secular SLR trend linked to AMOC diminishing, could both have large impacts on the coastal communities (Yin et al. 2009, Visbeck 2014, Rahmstorf et al. 2015).

Physically, both decadal accelerations and a secular SLR may affect shoreline dynamics, increase temporary or permanent land flooding and risk of storm flood hazards, cause erosion and shifts in hydrodynamics, which in turn could lead to, for example, poorer water quality and less freshwater supply and changes in coastal habitats (Wong et al. 2014, Romero-Lankao et al. 2014, Folger and Carter 2016). Socioeconomically, the physical changes may result in damage to infrastructure and freshwater habitats, health concerns, and demand large investments to ensure adaptation, protection and restoration, potentially leading to economic

challenges, and social inequality and environmental injustice concerns (Romero-Lankao et al. 2014, Folger and Carter 2016, Hardy et al. 2017).

Yet, the uncertainties related to natural internal variability versus secular trends in CSL change, as well as the general inter-model spread in SLR projections (Little et al. 2015, Chen et al. 2018), make it difficult to agree on mitigation and adaptation strategies that are scientifically robust and accurate enough to provide an informative range of likely outcomes that can direct feasible political action (Mimura 2013). To address such uncertainties it is crucial that more knowledge is obtained on the degree to which far-field Antarctic ice loss effects and Greenland ice losses with freshening of the ocean will affect the overturning circulation and SLR along the North American northeast coast (Gornitz et al. 2019, Yin et al. 2009, Yin and Goddard 2013). Greater understanding is also needed on other potential physical mechanisms of accelerating SLR such as wind forcing (Saenko et al. 2015), glacial isostatic adjustment (Davis and Vinogradova 2017), enhanced oceanic warming in the western Atlantic (Krasting et al. 2016) and air-sea flux uncertainties (Huber and Zanna 2017)

The most dramatic scenario of CSL change would likely be additions of meltwater from the Greenland (Fettweis et al. 2013) and Antarctic ice sheets (Levermann et al. 2014) to the already potential drivers of sea level acceleration along the Northeast coast (Yin et al. 2009, IPCC 2013, Davis and Vinogradova 2017). If a worst case scenario of rapid SLR is realised, the development and implementation of appropriate adaptation and mitigation strategies should not pend on longer observational records to validate the CSL acceleration's temporal characteristic and link to AMOC strength, but follow a precautionary approach. Not to mention, planning and impact management of decadal climate variations should not be ignored, but prioritised.

6.5 Limitations and future work

A major limitation of this project is the exclusion of wind forcing as part of a more broad-targeting assessment of the relative roles of changes in AMOC strength versus alongshore wind forcing in affecting sea level variations along the North American east coast on interannual to decadal timescales. Contrary to studies having found a strong anti-phase nature between AMOC and CSL on interannual and/or decadal timescales (e.g. Bingham and Hughes 2009, Yin and Goddard 2013, Goddard et al. 2015, McCarthy et al. 2015), some analyses (Woodworth et al. 2014, Little et al. 2017) find that AMOC and CSL variations are not robustly related on these timescales, especially if wind forcing is applied (Woodworth et al. 2014). However, a limitation of these latter studies is the evaluation of only a single ocean model with observations (Woodworth et al. 2014) or a single coupled model large ensemble

(Little et al. 2017). Given this, it would be interesting to investigate the role of wind forcing in affecting CSL variations in relation to AMOC on interannual and decadal timescales in a large number of CMIP5 or CMIP6 models. In such an analysis, focus should be directed towards possible timescale and forcing dependence.

A specific shortcoming of this study is the use of inconsistent number of realisations in the historical sea surface height simulations. While some models are based on the r1i1p1 realisation, other models are based on several realisations, up to 24 (GISS-E2-R). A control analysis should be performed to ensure that the results over the 20th century are not skewed in terms of some models retaining significantly more internal variability than others, thus affecting the AMOC-CSL correlations, linear regression analysis and model-data intercomparison.

If time had permitted, the analysis would have examined the AMOC-CSL relationship on multidecadal timescales as well as estimated long-term trends, since such temporal characteristics of the AMOC-CSL relationship are lacking in studies of a large number of CMIP5 models. Moreover, weighting techniques and calculation of a multi-model ensemble mean would be applied.

Not mention, more thorough testing and verification of model results, as well as a structured assessment of model uncertainty, should be performed to investigate the potential underlying causes of the intra- and inter-model spread seen in the AMOC-CSL relationship over the 20th-23rd centuries.

7 Concluding Remarks

The overall aim of this study was to examine the relationship between AMOC and coastal sea level (CSL) variability along the North American east coast on interannual and decadal timescales in CMIP5 models. The present study supports a case in which CSL north of 35°N is likely primarily driven by, or at least associated with, AMOC variability on decadal timescales, over both the 20th and 21st centuries, as indicated by an anti-phase AMOC-CSL nature demonstrated in a majority of models. Overall, the CMIP5 models suggest that dynamic sea level can act as an important AMOC proxy on decadal timescales along the North American northeast coast (~35°N-48°N). Still, the CMIP5 models are subject to inter-model spread as well a noticeable intra-model spread over the different 20th–23rd centuries. Moreover, the models generally underestimate the observed magnitude of both tide gauge and RAPID variability. The AMOC's potential influence on CSL variations on interannual timescales and south of Cape Hatteras remains uncertain and inconclusive.

Given the importance of a decadal AMOC-CSL coupling for climate prediction and corresponding impact management along the heavily populated and vulnerable U.S. east coast, the research community should continue efforts to improve our understanding of the interaction between AMOC, CSL, alongshore wind forcing and modes of low-frequency climate variability. This way, we might obtain a more robust and timely separation of natural low-frequency internal variability from anthropogenic causes as origin of the temporally limited but recently observed deceleration in AMOC strength.

Bibliography

Allan, R. and T. Ansell (2006). A new globally complete monthly historical gridded mean sea level pressure dataset (HadSLP2): 1850–2004. *J. Clim.,* **19,** 5816–5842, doi: 10.1175/JCLI3937.1.

Alley, R.B. (2007). Wally was right: Predictive ability of the North Atlantic "conveyor belt" hypothesis for abrupt climate change. *Annual Reviews of Earth and Planetary Sciences*, **35**, 241-272, doi:10.1146/annurev.earth.35.081006.131524.

Alley, R. B., P. U. Clark, L. D. Keigwin and R. S. Webb (1999). Making sense of millennial-scale climate change. *Geophys. Monograph American Geophys. Union*, **112**, 385– 394, doi:10.1029/GM112p0385.

Alvarez-Solas et al. (2011). Heinrich event 1: an example of dynamical ice-sheet reaction to oceanic changes. *Clim. Past*, **7**, 1297-1306, doi:10.5194/cp-7-1297-2011.

Alvarez-Solas, J., A. Robinson, M. Montoya and C. Ritz (2013). Iceberg discharges of the last glacial period driven by oceanic circulation changes. *PNAS,* **110**, 16350-16354, doi:10.1073/pnas.1306622110.

Andres, M., G. G. Gawarkiewicz and J. M. Toole (2013). Interannual sea level variability in the western North Atlantic: Regional forcing and remote response. *Geophys. Res. Lett*., **40**, 5915–5919, doi:10.1002/2013GL058013.

Ansorge, I. J., et al. (2014). Basin-wide oceanographic array bridges the South Atlantic. *EOS: Trans. Am. Geophys. Union,* **95,** 53-54, doi:10.1002/2014EO060001.

Arora, V. K., et al. (2011). Carbon emission limits required to satisfy future representative concentration path-ways of greenhouse gases. *Geophys. Res. Lett.,* **38**, L05805, doi:10.1029/2010GL046270.

Baehr, J., J. Hirschi, J.-O. Beismann and J. Marotzke (2004). Monitoring the meridional overturning circulation in the North Atlantic: A model-based array design study. *J. Mar. Res.*, **62**, 283–312, doi:10.1357/0022240041446191.

Bakker, P., et al. (2016). Fate of the Atlantic Meridional Overturning Circulation: Strong decline under continued warming and Greenland melting. *Geophys. Res. Lett.,* **43**, 12,212-252,260, doi:10.1002/2016GL070457.

Bao, Q., et al. (2013). The Flexible Global Ocean-Atmosphere-Land System model Version: FGOALS-s2. *Adv. Atmos. Sci.*, **30**, 561–576, doi:10.1007/s00376-012-2113-9.

Baringer, M. O., and J. C. Larsen (2001). Sixteen years of Florida Current transport at 27°N. *Geophys. Res. Lett.*, **28**, 3179–3182, doi:10.1029/2001GL013246.

Barker, S., et al. (2011). 800,000 years of abrupt climate variability. *Science*, **334**, 347-351, doi:10.1126/science.1203580.

Bentsen, M., et al. (2013). The Norwegian Earth System Model, NorESM1-M – Part 1: Description and basic evaluation of the physical climate. *Geosci. Model Dev.*, **6**, 687–720, doi:10.5194/gmd-6-687-2013.

Bi, D., et al. (2013). The ACCESS Coupled Model: Description, Control Climate and Preliminary Validation. *Aust. Met. Oceanogr. J.*, **63**, 41–64, doi:10.22499/2.6301.004.

Bingham, R. J, C. W. Hughes, V. Roussenov, R. G. Williams (2007). Meridional coherence of the North Atlantic meridional overturning circulation. *Geophys. Res. Lett.* **34**, L23606, doi:10.1029/2007GL031731.

Bingham, R. J., and C. W. Hughes (2008). Determining North Atlantic meridional transport variability from pressure on the western boundary: A model investigation. *J. Geophys. Res. Oceans*, **113**, C09008, doi:10.1029/2007JC004679.

Bingham, R. J., and C. W. Hughes (2009). Signature of the Atlantic meridional overturning circulation in sea level along the east coast of North America. *Geophys. Res. Lett.* **36,** L02603, doi: 10.1029/2008GL036215

Blaker, A. T., et al. (2014). Historical analogues of the recent extreme minima observed in the Atlantic meridional overturning circulation at 26°N. *Clim. Dyn*., doi:10.1007/s00382-014-2274-6.

Bond, G., et al. (1993). Correlation between climate records from North Atlantic sediments and Greenland ice. *Nature,* **365**, 143-147, doi:10.1038/365143a0.

Boon, J. D. (2012). Evidence of sea level acceleration at U.S. and Canadian tide stations, Atlantic coast, North America. *J. Coast. Res*., **28**, 1437–1445, doi:10.2112/JCOASTRES-D-12-00102.1.

Booth, B. B. B., N. J. Dunstone, P. R. Halloran, T. Andrews and N. Bellouin (2012). Aerosols implicated as a prime driver of twentieth-century North Atlantic climate variability. *Nature,* **484**, 228-232, doi:10.1038/nature10946.

Boulton, C.A., L.C. Allison and T.M. Lenton (2014). Early warming signals of Atlantic Meridional Overturning Circulation collapse in a fully coupled climate model. *Nature Comm.*, **5**, doi:10.1038/ncomms6752.

Bouttes, N., J. M. Gregory, T. Kuhlbrodt and R. S. Smith (2014). The drivers of projected North Atlantic sea level change. *Clim. Dynam*., **43**, 1531–1544, doi:10.1007/s00382-013-1973-8.

Brayshaw, D. J., T. Woollings and M. Vellinga (2009): Tropical and extratropical responses of the North Atlantic atmospheric circulation to a sustained weakening of the MOC. *J. Clim.,* **22**, 3146–3155, doi:10.1175/2008JCLI2594.1.

Brix, H., and R. Gerdes (2003). North Atlantic deep water and Antarctic bottom water: Their interaction and influence on the variability of the global ocean circulation. *J. Geophys. Res.*, **108**(C2), 3022, doi:10.1029/2002JC001335.

Broccoli, A. J., K. A. Dahl and R. J. Stouffer (2006). Response of the ITCZ to Northern Hemisphere cooling. *Geophys. Res. Lett.,* **33,** L01702, 1-4, doi:10.1029/2005GL024546.

Broecker, W. S. (1979). A Revised Estimate for the radiocarbon age of North Atlantic Deep Water. *J. Geophys. Res.*, **84(C6)**, 3218–3226, doi:10.1029/JC084iC06p03218.

Broecker, W. S. (1991). The great ocean conveyor. *Oceanography,* **4**, 79–89, doi:10.5670/oceanog.1991.07.

Broecker, W. S. (2006). Abrupt climate change revisited, *Global Planet. Change*, **54,** 211–215, doi:10.1016/j.gloplacha.2006.06.019.

Broecker, W.S., D.M. Peteet, and D. Rind, (1985). Does the ocean-atmosphere system have more than one stable mode of operation? *Nature*, **315**, 21-26, doi:10.1038/315021a0.

Brunnabend. S.-E., J. Schroter, R. Rietbroek, J. Kusche (2015). Regional sea level change in response to ice mass loss in Greenland, the west Antarctic and Alaska, *J. Geophys. Re. Oceans*, **120**, 7316-7328.

Bryden, H. L., H. R. Longworth and S. A. Cunningham (2005). Slowing of the Atlantic meridional overturning circulation at 25°N. *Nature*, **438**, 655-657 (2005).

Bryden, H. L., B. A. King and G. D. McCarthy (2011). South Atlantic overturning circulation at 24°S. *J. Mar. Res.*, **69**, 39–56, doi:10.1357/002224011798147633.

Buckley, M.W., and J. Marshall (2015). Observations, inferences, and mechanisms of Atlantic Meridional Overturning Circulation variability: A review*, Rev. Geophys*., **54,** 5-63, doi: 10.1002/2015RG000493(2016).

Böhm, E., J. Lippold, M. Gutjahr et al. (2015). Strong and deep Atlantic meridional overturning circulation during the last glacial cycle. *Nature*, **517**, 74-79. doi:10.1038/nature14059

Caesar, L., S. Rahmstorf, A. Robinson, G. Feulner and V. Saba (2018). Observed fingerprint of a weakening Atlantic Ocean overturning circulation. *Nature*, **556**, 191–196, doi:10.1038/s41586-018-0006-5.

Calafat, F. M., T. Wahl, F. Lindsten, J. Williams and E. Frajka-Williams (2018). Coherent modulation of the sea-level annual cycle in the United States by Atlantic Rossby waves. *Nat. Commun.,* **9**, 2571*,* doi:10.1038/s41467-018-04898-y.

Calvo, N., R. R. Garcia, D. R. Marsh, M. J. Miils, D. E. Kinnison, and P. J. Young (2012). Reconciling modeled and observed temperature trends over Antarctica. *Geophys. Res. Lett.*, **39**, L16803, doi:10.1029/2012GL052526.

Carlson A.E. (2013). The Younger Dryas Climate Event. In: Elias S.A. (ed.). *Encyclopedia of Quaternary Science*, **3**, 126-134, doi:10.1016/B978-0-444-53643-3.00029-7.

Carson, M., A. Köhl and D. Stammer (2015). The impact of regional multidecadal and century-scale internal climate variability on sea level trends in CMIP5 models. *J. Clim.*, **28**, 853–861, doi:10.1175/JCLI-D-14-00359.1.

Chen, C., W. Liu and G. Wang (2018). Understanding the uncertainty in the 21st century dynamic sea level projections: The role of the AMOC. *Geophys. Res. Let.,* **46**, 210-217.

Cheng, W., J. C. H. Chiang and D. Zhang (2013). Atlantic meridional overturning circulation (AMOC). in CMIP5 models: RCP and historical simulations. *J. Clim.*, **26**, 7187–7197, doi:10.1175/JCLI-D-12-00496.1.

Chereskin, T. K., and D. Roemmich (1991). A Comparison of Measured and Wind-derived Ekman Transport at 11°N in the Atlantic. *Ocean, J. Phys. Oceanogr.*, **21**, 869–878, doi:10.1175/1520-0485(1991)021<0869:ACOMAW>2.0.CO;2.

Church, J.A., P.U. Clark, A. Cazenave, J.M. Gregory, S. Jevrejeva, A. Levermann, M.A. Merrifield, G.A. Milne, R.S. Nerem, P.D. Nunn, A.J. Payne, W.T. Pfeffer, D. Stammer and A.S. Unnikrishnan, (2013). Sea Level Change. In: *Climate Change 2013: The Physical Science Basis. Contribution of Working Group I to the Fifth Assessment Report of the Intergovernmental Panel on Climate Change* [Stocker, T.F., D. Qin, G.-K. Plattner, M. Tignor, S.K. Allen, J. Boschung, A. Nauels, Y. Xia, V. Bex and P.M. Midgley (eds.)]. Cambridge University Press, Cambridge, United Kingdom and New York, NY, US.

Clark, P. U., N. G. Pisias, T. F. Stocker and J. A. Weaver (2002). The role of the thermohaline circulation in abrupt climate change. *Nature*, **415**, 863–869, doi:10.1038/415863a.

Clark, P. U., S. W. Hostetler, N.G. Pisias, A. Schmittner and K. J. Meissner (2007). Mechanisms for an ~7-kyr Climate and Sea-Level Oscillation During Marine Isotope Stage 3. *Geophys. Monograph Series*, **173**, 209-246.

Clement, A. C., and L. C. Peterson (2008). Mechanisms of abrupt climate change of the Last Glacial period. *Rev. Geophys.*, **46**, RG4002, doi:10.1029/2006RG000204.

Collins, M., et al. (2012). Quantifying future climate change. *Nature Clim. Change*, **2**, 403–409, doi:10.1038/nclimate1414.

Collins, M., R. Knutti, J. Arblaster, J.-L. Dufresne, T. Fichefet, P. Friedlingstein, X. Gao, W.J. Gutowski, T. Johns, G. Krinner, M. Shongwe, C. Tebaldi, A.J. Weaver, and M. Wehner (2013). Long-term climate change: Projections, commitments and irreversibility. In *Climate Change 2013: The Physical Science Basis. Contribution of Working Group I to the Fifth Assessment Report of the Intergovernmental Panel on Climate Change*. [T.F. Stocker, D. Qin, G.-K. Plattner, M. Tignor, S.K. Allen, J. Doschung, A. Nauels, Y. Xia, V. Bex, and P.M. Midgley, (Eds.)].Cambridge University Press, pp. 1029-1136, doi:10.1017/CBO9781107415324.024

Collins, W. J., et al. (2011). Development and evaluation of an Earth-System model HadGEM2. *Geosci. Model Dev.*, **4**, 1051–1075, doi:10.5194/gmd-4-1051-2011.

Cunningham, S. A., et al. (2007). Temporal variability of the Atlantic meridional overturning circulation at 26.5°N. *Science,* **317**, 935–938, doi:10.1126/science.1141304.

Davini, P., J. von Hardenberg, L. Filippi and A. Provenzale (2015). Impact of Greenland orography on the Atlantic Meridional Overturning Circulation. *Geophys. Res. Lett.*, **42**, 871–879, doi:10.1002/2014GL062668.

Davis, J.L. and N.T. Vinogradova (2017). Causes of accelerating sea level on the East Coast of North America. *Geophys. Res. Lett.*, **44**, 5133-5141, doi:10.1002/2017GL072845.

de Coëtlogon et al. (2006). Gulf Stream variability in five oceanic general circulation models. *J. Phys. Oceanogr.*, **36**, 2119-2135, doi:10.1175/JPO2963.1.

Delworth, T. L., and M.E. Mann. (2000). Observed and simulated multidecadal variability in the Northern Hemisphere. *Clim. Dynam*. **16**, 661-676, doi:10.1007/s003820000075.

Delworth, T. L., et al. (2006). GFDL's CM2 global coupled climate models. Part I: Formulation and simulation characteristics. *J. Clim.*, **19**, 643–674, doi:10.1175/JCLI3629.1.

Delworth, T. L., Clark, P. U., Holland, M., Johns, T., Kuhlbrodt, T., Lynch-Stieglitz, C., Seager, R., Weaver, A. J. and Zhang, R. (2008). *The potential for abrupt change in the Atlantic Meridional Overturning Circulation.* In: Abrupt Climate Change. A report by the U.S. Climate Change Science Program and the Subcommittee on Global Change Research. U. S. Geological Survey, Reston, VA, 258-359. Downloaded November 2016 from https://www.gfdl.noaa.gov/bibliography/related_files/td0802.pdf.

Dix, M., et al. (2013). The ACCESS Coupled Model: Documentation of core CMIP5 simulations and initial results. *Aust. Met. Oceanogr. J.*, **63**, 83–99, doi:10.22499/2.6301.006.

Donner, L. J., et al. (2011). The dynamical core, physical parameterizations, and basic simulation characteristics of the atmospheric component AM3 of the GFDL Global Coupled Model CM3. *J. Clim.*, **24**, 3484–3519, doi:10.1175/2011JCLI3955.1

Döscher, R., C. W. Böning and P. Herrmann (1994). Response of circulation and heat transport in the North Atlantic to changes in thermohaline forcing in northern latitudes: a model study. *J. Phys. Oceanogr.,* **24**, 2306–2320, doi:10.1175/1520-0485(1994)024<2306:ROCAHT>2.0.CO;2.

Dufresne, J.-L., et al. (2013). Climate change projections using the IPSL-CM5 Earth System Model: From CMIP3 to CMIP5. *Clim. Dyn.*, **40**, 2123–2165, doi:10.1007/s00382-012-1636-1.

Dunne, J. P., et al. (2012). GFDL's ESM2 Global coupled climate-carbon Earth System models. Part I: Physical formulation and baseline simulation characteristics. *J. Clim.*, **25**, 6646–6665, doi:10.1175/JCLI-D-11-00560.1.

Drijfout, S. S., S. L. Weber and E. van der Swaluw (2011). The stability of the MOC as diagnosed from model projections for pre-industrial, present and future climates. *Clim. Dyn.*, **37**, 1575–1586, doi:10.1007/s00382-010-0930-z.

Ekman, V.W. (1905). On the influence of earth's rotation on ocean currents. *Ark.Mat.Ast.Fys., Stockholm,* **2**, 1-52.

Enderlin, E. M., et al. (2014). An improved mass budget for the Greenland ice sheet. *Geophys. Res. Lett.*, **41**, 866–872, doi:10.1002/2013GL059010.

Enfield, D., A. M. Mestas-Nuñez, D. A. Mayer and L. Cid-Serrano (1999). How ubiquitous is the dipole relationship in tropical Atlantic sea surface temperatures. *J. Geophys. Res.*, **104**, 7841–7848, doi:10.1029/1998JC900109.

Ezer, T. (1999). Decadal variabilities of the upper layers of the subtropical North Atlantic: an ocean model study. *J. Phys. Oceanogr.* **29**, 3111–3124, doi:10.1175/1520-0485(1999)029

Ezer, T. (2001). Can long-term variability in the Gulf Stream transport be inferred from sea level? *Geophys. Res. Lett*., **28**, 1031–1034, doi:10.1029/2000GL011640.

Ezer, T. (2013). Sea level rise, spatially uneven and temporally unsteady: why the U.S. East Coast, the global tide gauge record, and the global altimeter data show different trends. *Geophys. Res. Lett*., **40,** 5439–5444, doi:10.1002/2013GL057952.

Ezer, T. (2015). Detecting changes in the transport of the Gulf Stream and the Atlantic overturning circulation from coastal sea level data: The extreme decline in 2009–2010 and estimated variations for 1935–2012. *Global and Planetary Change*, 2015, **129**, 23-36, doi:10.1016/j.gloplacha.2015.03.002.

Ezer, T. (2016). Can the Gulf Stream induce coherent short-term fluctuations in sea level along the U.S. East Coast?: A modeling study, *Ocean Dynamics*, **66**(2). 207-220

Ezer, T., and L. P. Atkinson (2014). Accelerated flooding along the U.S. East Coast: on the impact of sea-level rise, tides, storms, the Gulf Stream, and the North Atlantic Oscillations. *Earth's Future,* **2**, 362–382, doi:10.1002/2014EF000252.

Ezer, T., and W. B. Corlett (2012). Is sea level rise accelerating in the Chesapeake Bay? A demonstration of a novel new approach for analyzing sea level data. *Geophys. Res. Lett.*, **39**, L19605, doi:10.1029/2012GL053435.

Ezer, T., L. P. Atkinson, W. C. Corlett and J. L. Blanco. (2013). Gulf Stream's induced sea level rise and variability along the U.S. mid-Atlantic coast. *J. Geophys. Res*. **118**, 685–697, doi:10.1002/jgrc.20091.

Fettweis, X., et al. (2013). Estimating the Greenland ice sheet surface mass balance contribution to future sea level rise using the regional atmospheric climate model MAR. *The Cryosphere*, **7**, 469–489, doi:10.5194/tc-7-469-2013

Feulner, G., S. Rahmstorf, A. Levermann and S. Volkwardt (2013). On the origin of the surface air temperature difference between the hemispheres in Earth's present-day climate. *J. Clim*. **26**, 7136-7150, doi:10.1175/JCLI-D-12-00636.1.

Fichefet, T., et al. (2003). Implications of changes in freshwater flux from the Greenland ice sheet for the climate of the 21st century. *Geophys. Res. Lett.*, **30 (17)**, 1911, doi:10.1029/2003GL017826.

Flato, G., J. Marotzke, B. Abiodun, P. Braconnot, S.C. Chou, W. Collins, P. Cox, F. Driouech, S. Emori, V. Eyring, C. Forest, P. Gleckler, E. Guilyardi, C. Jakob, V. Kattsov, C. Reason and M. Rummukainen (2013). Evaluation of Climate Models. In: *Climate Change 2013: The Physical Science Basis. Contribution of Working Group I to the Fifth Assess- ment Report of the Intergovernmental Panel on Climate Change* [Stocker, T.F., D. Qin, G.-K. Plattner, M. Tignor, S.K. Allen, J. Boschung, A. Nauels, Y. Xia, V. Bex and P.M. Midgley (eds.)]. Cambridge University Press, Cambridge, United Kingdom and New York, NY, USA.

Fogli, P. G., et al. (2009). INGV-CMCC Carbon (ICC): A Carbon Cycle Earth System Model. *CMCC Res. Paper,* **61***,* 1-30*,* doi:10.2139/ssrn.1517282.

Folger, P., and N. T. Carter (2016). Sea-Level Rise and U.S. Coasts: Science and Policy Considerations. *CRS REPORT*, Prepared for Members and Commitees of Congress, Congressional Research Service, 7-5700, downloaded 20th of November 2019 from https://fas.org/sgp/crs/misc/R44632.pdf.

Fontela, M., M. I. García-Ibáñez, D. A. Hansell, H. Mercier and F. F. Pérez (2016). Dissolved Organic Carbon in the North Atlantic Meridional Overturning Circulation. *Sci. Rep.,* **6**, 1-9, doi: 10.1038/srep26931.

Frajka-Williams, E. (2015). Estimating the Atlantic MOC at 26°N using satellite altimetry and cable measurements. *Geophys. Res. Lett.*, **42**, 3458–3464, doi: 10.1002/2015GL063220.

Frajka-Williams E, Ansorge IJ, Baehr J, Bryden HL, Chidichimo MP, Cunningham SA, Danabasoglu G, Dong S, Donohue KA, Elipot S, Heimbach P, Holliday NP, Hummels R, Jackson LC, Karstensen J, Lankhorst M, Le Bras IA, Lozier MS, McDonagh EL, Meinen CS, Mercier H, Moat BI, Perez RC, Piecuch CG, Rhein M, Srokosz MA, Trenberth KE, Bacon S, Forget G, Goni G, Kieke D, Koelling J, Lamont T, McCarthy GD, Mertens C, Send U, Smeed DA, Speich S, van den Berg M, Volkov D and Wilson C (2019). Atlantic Meridional Overturning Circulation: Observed Transport and Variability. *Front. Mar. Sci.*, 6:260, doi: 10.3389/fmars.2019.00260

Franklin, C. N., et al. (2013). Evaluation of clouds in ACCESS using the satellite simulator package COSP. Global, seasonal and regional cloud properties. *J. Geophys. Res.*, **118**, 732–748. doi:10.1029/2012JD018469.

Frierson, D., Hwang, Y, Fučkar N, et al. (2013). Contribution of ocean overturning circulation to tropical rainfall peak in the Northern Hemisphere. *Nature Geosci.*, **6**, 940–944, doi:10.1038/NGEO1987.

Gent, P. R., et al. (2011). The Community Climate System Model version 4. *J. Clim.*, **24**, 4973–4991, doi:10.1175/2011JCLI4083.1.

Giorgetta, M. A., et al. (2013). Climate and carbon cycle changes from 1850 to 2100 in MPI-ESM simulations for the Coupled Model Intercomparison Project phase 5. *J. Adv. Mod. Earth Sys.*, **5**, 572–597, doi:10.1002/jame.20038.

Goddard, P. B., Yin, J., Griffies, S., and Zhang, S. (2015). An extreme event of sea-level rise along the Northeast coast of North America in 2009–2010, *Nat Commun*., **6**, 6346, doi:10.1038/ncomms7346, 2015.

Goldenberg, S. B., C. W. Landsea, A. M. Mestas-Nunez, and W. M. Gray (2001). The recent increase in Atlantic hurricane activity: Causes and implications, *Science*, **293**, 474–479, doi:10.1126/science.1060040.

Gordon, C., et al. (2000). The simulation of SST, sea ice extents and ocean heat transports in a version of the Hadley Centre coupled model without flux adjustments. *Clim. Dyn.*, **16**, 147–168, doi:10.1007/s003820050010.

Gornitz, V., et al. (2019). New York City Panel on Climate Change 2019 Report Chapter 3: Sea Level Rise. *Ann. N.Y. Acad. Sci.*, **1439**, 71-94, doi:10.1111/nyas.14006.

Greatbatch, R. J. (1994). A note on the representation of steric sea level in models that conserve volume rather than mass. *J. Geophys. Res.*, **99**, 12,767–12,771, doi:10.1029/94JC00847.

Green, B., and J. Marshall (2017). Coupling of trade winds with ocean circulation damps ITCZ shifts. *J. Clim.*, **30**, 4395–4411, doi:10.1175/JCLI-D-16-0818.1.

Gregorio, S., et al. (2015). Intrinsic variability of the Atlantic meridional overturning circulation at interannual-to-multidecadal time scales. *J. Phys. Oceanogr.* **45** (7). 1929–1946. http://dx.doi.org/10. 1175/JPO-D-14-0163.1.

Gregory, J.M., et al. (2005). A model intercomparison of changes in the Atlantic thermohaline circulation in response to increasing atmospheric CO2 concentration. *Geophys. Res. Lett.*, **32**, L12703, doi:10.1029/2005GL023209.

Griffies, S.M., and R.J. Greatbatch (2012). Physical processes that impact the evolution of global mean sea level in ocean climate models. *Ocean Modell.*, **51**, 37–72, doi:10.1016/j.ocemod.2012.04.003.

Hakkinen, S. (2000). Decadal air-aea interaction in the North Atlantic based on observations and modeling results. *J. Clim.,***13**, 1195–1219, doi:10.1175/15200442(2000)013<1195:DASIIT>2.0.CO;2.

Hakkinen, S. (2001). Variability in sea surface height: A qualitative measure for the meridional overturning in the North Atlantic. *J. Geophys.Res*., **106**, 837-848.

Hall, M. M., and H. L. Bryden (1982). Direct estimates and mechanisms of ocean heat transport. *Deep Sea Res.*, **29**, 339–359, doi:10.1016/0198-0149(82)90099-1.

Halloran, P. R., et al. (2015). The mechanisms of North Atlantic CO2 uptake in a large Earth System Model ensemble. *Biogeosciences*, **12**, 4497–4508, doi:10.5194/bg-12-4497-2015.

Han, Z., et al. (2016). Simulation by CMIP5 models of the Atlantic Multidecadal Oscillation and its climate impacts. *Adv. Atmos. Sci.*, **33**, 1329– 1342, doi:10.1007/s00376-016-5270-4.

Hardy, R. D., R. A. Milligan and N. Heynen (2017). Racial coastal formation: The environmental injustice of colorblind adaptation planning for sea-level rise. *Geoforum*, **87**, 62-72, doi:10.1016/j.geoforum.2017.10.005.

Hawkins, E., and R. Sutton (2009). The potential to narrow uncertainty in regional climate predictions. *Bull. Am. Meteorol. Soc*., **90**, 1095-1107, doi:10.1175/2009BAMS2607.1.

Hawkins, E., et al. (2011). Bistability of the Atlantic overturning circulation in a global climate model and links to ocean freshwater transport. *Geophys. Res. Lett.*, **38**, L10605, doi:10.1029/2011GL047208.

Hazeleger, W., et al. (2012). EC-Earth V2.2: Description and validation of a new seamless earth system prediction model. *Clim. Dyn.*, **39**, 2611–2629, doi:10.1007/s00382-011-1228-5.

Heuzé, C. (2017). North Atlantic deep water formation and AMOC in CMIP5 models. *Ocean Sci.*, **13**, 609–622, doi:10.5194/os-13-609-2017.

Hayhoe, K., J. Edmonds, R.E. Kopp, A.N. LeGrande, B.M. Sanderson, M.F. Wehner, and D.J. Wuebbles (2017). Climate models, scenarios, and projections. In *Climate Science Special Report: Fourth National Climate Assessment, Volume I*. [D.J. Wuebbles, D.W. Fahey, K.A. Hibbard, D.J. Dokken, B.C. Stewart, and T.K. Maycock, (Eds.)]. U.S. Global Change Research Program, 133-160, doi:10.7930/J0WH2N54.

Higginson, S., Y. Thompson, P. L. Woodworth and C. W. Hughes (2015). The tilt of mean sea level along the east coast of North America. *Geophys. Res. Lett.*, **42**, 1471–1479, doi:10.1002/2015GL063186

Hobbs, W., M. D. Palmer and D. Monselesan (2016). An energy conservation analysis of ocean drift in the CMIP5 global coupled models. *J. Clim.*, **29**, 1639–1653, doi:10.1175/JCLI-D-15-0477.1.

Hofmann, M., and S. Rahmstorf (2009). On the stability of the Atlantic meridional overturning circulation. *Proc. Natl Acad. Sci. USA* **106**, 20584-20589. doi.org/10.1073/pnas.0909146106

Holgate, S. J., et al. (2013). New Data Systems and Products at the Permanent Service for Mean Sea Level. *J. Coast. Res.,* **29**, 493-504, doi:10.2112/JCOASTRES-D-12-00175.1.

Houghton, R.W., and Y.M. Tourre (1992). Characteristics of low-frequency sea surface temperature fluctuations in the tropical Atlantic. *J. Clim.*, **5**, 765–771, doi:10.1175/1520-0442(1992)005<0765:COLFSS>2.0.CO;2.

Howard, T., et al. (2014). The land-ice contribution to 21st-century dynamic sea level rise. *Ocean Sci*., **10,** 485–500, doi:10.5194/os-10-485-2014, 2014.

Hu, A., B. L. Otto-Bliesner and G. A. Meehl (2008). Response of thermohaline circulation to freshwater forcing under present-day and LGM conditions. *J. Clim.*, **21**, 2239–2258, doi:10.1175/2007JCLI1985.1.

Hu, A., G.A. Meehl, W. Han and J. Yin (2009). Transient response of the MOC and climate to potential melting of the Greenland ice sheet in the 21st century. *Geophys. Res. Lett.*, **36**, L10707, doi:10.1029/2009GL037998.

Hu, A., G. A. Meehl, W. Han, and J. Yin (2011), Effect of the potential melting of the Greenland Ice Sheet on the Meridional Overturning Circulation and global climate in the future, *Deep Sea Res. Part II*, *58*, 1914–1926, doi:10.1016/j.dsr2.2010.10.069

Huber, M. B., and L. Zanna (2017). Drivers of uncertainty in simulated ocean circulation and heat uptake. *Geophys. Res. Lett.*, **44**, 1402-1413, doi:10.1002/2016GL071587.

Huisman, S. E., M. den Toom and H. A. Dijkstra (2010). An indicator of the multiple equilibria regime of the Atlantic meridional overturning circulation. *J. Phys. Oceanogr.*, **40**, 551–567, doi:10.1175/2009JPO4215.1.

Huthnance, J. M. (2004). Ocean-to-shelf signal transmission: a parameter study. *J. Geophys. Res.*, **109**, C12029, 1-11, doi:10.1029/2004JC002358.

IPCC, 2013. Climate Change 2013: The Physical Science Basis. Contribution of Working Group I to the Fifth Assessment Report of the Intergovernmental Panel on Climate Change [Stocker, T.F., D. Qin, G.-K. Plattner, M. Tignor, S.K. Allen, J. Boschung, A. Nauels, Y. Xia, V. Bex and P.M. Midgley (eds.)]. Cambridge University Press, Cambridge, United Kingdom and New York, NY, USA, 1535 pp.

Ivchenko, V. O., D. Sidorenko, S. Danilov, M. Losch and J. Schröter (2011). Can sea surface height be used to estimate oceanic transport variability? *Geophys. Res. Lett.*, **38**, L11601, doi:10.1029/2011GL047387.

Iversen, T., et al. (2013). The Norwegian Earth System Model, NorESM1-M – Part 2: Climate response and scenario projections. *Geosci. Model Dev.*, **6**, 389–415, doi:10.5194/gmd-6-389-2013.

Jackson, L. C., K. A. Peterson, C. D. Roberts and R. A. Wood (2016). Recent slowing of Atlantic overturning circulation as a recovery from earlier strengthening. *Nature Geosci.*, **9**, 518–522. doi:10.1038/ngeo2715.

Jeffreys, H. (1925). On fluid motions produced by differences of temperature and humidity, Q.J.R. *Meteorol. Soc.*, **51**, 347–356, doi:10.1002/qj.49705121604.

Ji, D., et al. (2014). Description and basic evaluation of BNU-ESM version 1. *Geoscientific Model Development*, **7**, 1601-1647, doi:10.5194/gmdd-7-1601-2014.

Jiang, Y., T. H. Dixon and S. Wdowinski (2010). Accelerating uplift in the North Atlantic region as an indicator of ice loss. *Nature Geosci.*, **3(6)**, 404–407, doi:10.1038/ngeo845.

Johns, W. E., and Beal, L. M., et al. (2008). Variability of shallow and deep western boundary currents off the Bahamas during 2004–05: Results from the 26°N RAPID-MOC array. *J. Phys. Oceanogr.*, **38**, 605–623, doi:10.1175/2007JPO3791.1.

Johns, W. E., et al. (2011). Continuous, array-based estimates of Atlantic Ocean heat transport at 26.5° N. *J. Clim.*, **24**, 2429– 2449, doi:10.1175/2010JCLI3997.1.

Johnson, H. L., and D. P. Marshall (2002). A theory for the surface Atlantic response to thermohaline variability. *J. Phys. Oceanogr.,* **32**, 1121-1132.

Joyce, T. M., and R. Zhang (2010). On the path of the Gulf Stream and the Atlantic Meridional Overturning Circulation. *J. Clim.*, **23**, 3146–3154, doi:10.1175/2010JCLI3310.1.

Jungclaus, J. H., H. Haak, M. Esch, E. Roeckner and J. Marotzke (2006). Will Greenland melting halt the thermohaline circulation? *Geophy. Res. Lett.*, **33**, L17708, doi:10.1029/2006GL026815.

Kageyama, M., et al. (2013). Climatic impacts of fresh water hosing under Last Glacial Maximum conditions: a multi-model study. *Clim. Past*, **9**, 935–953, doi:10.5194/cp-9-935-2013.

Kamykowski, D. (2010). Atlantic meridional overturning circulation and phosphate-classified bottom up control of Atlantic pelagic ecosystems through the 20th century. *Deep Sea Res.*, **57,** 1266-1277, doi:10.1016/j.dsr.2010.06.013.

Kang, S. M., I. M. Held, D. M. W. Frierson and M. Zhao (2008). The response of the ITCZ to extratropical thermal forcing: Idealized slab-ocean experiments with a GCM. *J. Clim.*, **21**, 3521–3532, doi:10.1175/2007JCLI2146.1.

Kang, S. M., R. Seager, D. M. W. Frierson and X. Liu (2014). Croll revisited: Why is the northern hemisphere warmer than the southern hemisphere? *Clim. Dyn.*, **44**, 1457–1472, doi:10.1007/s00382-014-2147-z.

Kanzow, T., et al. (2007). Observed flow compensation associated with the MOC at 26.5°N in the Atlantic. *Science*, **317**, 938–941, doi:10.1126/science.1141304.

Kanzow, T, H. Johnson, D. Marshall, S. A. Cunningham, J. J.-M. Hirschi, A. Mujahid, H. L. Bryden, and W. E. Johns (2009). Basinwide integrated volume transports in an eddy-filled ocean. *J. Phys. Oceanogr.,* **39,** 3091–3110

Kawase, M. (1987). Establishment of deep ocean circulation driven by deep-water production. *J. Phys. Oceanogr.*, **17**, 2294–2317, doi:10.1175/1520-0485(1987)017<2294:EODOCD>2.0.CO;2.

Keenlyside, N., M. Latif, J. Jungclaus, L. Kornblueh and E. Roeckner (2008). Advancing decadal-scale climate prediction in the North Atlantic sector. *Nature*, **453**, 84–88, doi:10.1038/nature06921.

Keigwin, L. D., and E. A. Boyle (2000). Detecting Holocene changes in thermohaline circulation. *PNAS*, **97**, 1343-1346, doi:10.1073/pnas.97.4.1343.

Khatiwala, S., et al. (2013). Global ocean storage of anthropogenic carbon. *Biogeosciences*, **10**, 2169–2191, doi:10.5194/bg-10-2169-2013.

Kienert, H., and S. Rahmstorf (2012). On the relation between meridional overturning circulation and sea-level gradients in the Atlantic, *Earth Syst. Dynam*.,**3,** 109–120, doi:10.5194/esd-3-109-2012

Kirtman, B., S.B. Power, J.A. Adedoyin, G.J. Boer, R. Bojariu, I. Camilloni, F.J. Doblas-Reyes, A.M. Fiore, M. Kimoto, G.A. Meehl, M. Prather, A. Sarr, C. Schär, R. Sutton, G.J. van Oldenborgh, G. Vecchi and H.J. Wang (2013). Near-term Climate Change: Projections and Predictability. *In: Climate Change 2013: The Physical Science Basis. Contribution of Working Group I to the Fifth Assessment Report of the Intergovernmental Panel on Climate Change* [Stocker, T.F., D. Qin, G.-K. Plattner, M. Tignor, S.K. Allen, J. Boschung, A. Nauels, Y. Xia, V. Bex and P.M. Midgley (eds.)]. Cambridge University Press, Cambridge, United Kingdom and New York, NY, USA.

Knutti, R. (2010). The end of model democracy? *Clim. Change*, **102**, 395-404, doi:10.1007/s10584-010-9800-2.

Knutti, R., J. Sedlacek, B.M. Sanderson, R. Lorenz, E.M. Fischer and V. Eyring (2017). A climate model projection weighting scheme accounting for performance and interdependence. *Geophys. Res. Lett*, **44**, 1909-1918, doi:10.1002/2016GL072012.

Kopp, R. E. (2013). Does the mid-Atlantic United States sea-level acceleration hot spot reflect ocean dynamic variability?. *Geophys. Res. Lett.*, **40**, 3981–3985, doi:10.1002/grl.50781.

Krasting, J. P., J. P. Dunne, R. J. Stouffer and R. W. Hallberg (2016). Enhanced Atlantic sea-level rise relative to the Pacific under high carbon emission rates. *Nature Geosci.*, **9**, 210, doi:10.1038/ngeo2641.

Kuhlbrodt, T., et al. (2007). On the driving processes of the Atlantic meridional overturning circulation. *Rev. Geophys*., **45**, RG2001, doi:10.1029/2004RG000166.

Lamarque, J. F., et al. (2012), CAM-chem: Description and evaluation of interactive atmospheric chemistry in the Community Earth System Model,. *Geosci. Model Dev.*, **5**, 369–411, doi:10.5194/gmd-5-369-2012.

Landerer, F. W., Jungclaus, J. H., & Marotzke, J.(2007). Regional dynamic and steric sea level change in response to the IPCC-A1B Scenario. *Journal of Physical Oceanography*, **37**, 296–312. doi.org/10.1175/JPO3013.1.

Larsen, J. C., and Sanford, T. B. (1985). Florida Current volume transports from voltage measurements. *Science*, **227**, 302–304, doi:10.1126/science.227.4684.302.

Latif, M., et al. (2004). Reconstructing, monitoring, and predicting multidecadal-scale changes in the North Atlantic thermohaline circulation with sea surface temperature. *J. Clim.*, **17**, 1605-1614, doi:10.1175/1520-0442(2004)017<1605:RMAPMC>2.0.CO;2.

Latif, M., et al. (2006). Is the Thermohaline Circulation Changing? *J. Clim.*, **19**, 4631–4637, doi:10.1175/JCLI3876.1.

Lavin, A., H. L. Bryden and G. Parilla (1998). Meridional transport and heat flux variations in the subtropical North Atlantic. *Global Atmos. Ocean Sys.*, **6**, 269-293, doi:10.1007/s11110-007-0004-x.

Lawrence, D., et al. (2012). The CCSM4 Land Simulation, 1850-2005: Assessment of Surface Climate and New Capabilities. *J. Climate*, **25**, 2240-2260, doi:10.1175/Jcli-D-11-00103.1.

Lecci, R., S. Masina, A. Cherchi and M. Barreiro (2016). A coupled model study on the Atlantic Meridional Overturning Circulation under extreme atmospheric CO2 conditions. *Annals of Geophys.,* **59,** P0215, doi:10.4401/ag-6658.

Levermann, A., A. Griesel, M. Hofmann, M. Montoya, and S. Rahmstorf. (2005). Dynamic sea level changes following changes in the thermohaline circulation, *Clim. Dyn.,* **24**, 347-354, doi: 10.1007/s00382-004-0505-y.

Levermann A, et al. (2012). Potential climatic transitions with profound impact on Europe - Review of the current state of six 'tipping elements of the climate system'. *Clim Change,* **110**, 845–878. doi:10.1007/s10584-011-0126-5.

Levermann, A., Winkelmann, R., Nowicki, S., Fastook, J. L., Frieler, K., Greve, R., Hellmer, H. H., Martin, M. A., Meinshausen, M., Mengel, M., Payne, A. J., Pollard, D., Sato, T., Timmermann, R., Wang, W. L., and Bindschadler, R. A. (2014). Projecting Antarctic ice discharge using response functions from SeaRISE ice-sheet models, *Earth Syst. Dynam*., **5**, 271–293, https://doi.org/10.5194/esd-5-271-2014, 2014.

Li, L., et al. (2013). The flexible global ocean-atmosphere-land system model, Grid-point Version 2: FGOALS-g2. *Adv. Atmos. Sci.*, **30**, 543-560 , doi:10.1007/s00376-012-2140-6.

Li, Y., R. Ji, P. S. Fratantoni, C. Chen, J. A. Hare, C. S. Davis, and R. C. Beardsley (2014). Wind- induced interannual variability of sea level slope, along-shelf flow, and surface salinity on the Northwest Atlantic shelf. *J. Geophys. Res. Oceans*, **119**, 2462–2479, doi:10.1002/2013JC009385.

Li, H., T. Ilyina, W. A. Müller and F. Sienz (2016). Decadal predictions of the North Atlantic CO2 uptake. *Nat. Commun.*, **7**, 11076, doi:10.1038/ncomms11076.

Little, C.M., R.M. Horton, R.E. Kopp, M. Oppenheimer, and S. Yip (2015). Uncertainty in twenty-first-century CMIP5 sea level projections. *J. Climate*, **28**, 838-852, doi:10.1175/JCLI-D-14-00453.1.

Little, C.L, C.G. Piecuch and R.M. Ponte (2017). On the relationship between the meridional overturning circulation, alongshore wind stress, and the United States East Coast sea level in the Community Earthy System Model Large Ensemble. *Journal of Geophysical Research,* **122**, 4554-4568, doi:10.1002/2017JC012713.

Little, C. M., et al. (2019). The Relationship Between U.S. East Coast Sea Level and the Atlantic Meridional Overturning Circulation: A Review. *JGR Oceans,* **124**, 6435-6458, doi:10.1029/2019JC015152.

Liu, W., Liu, Z., & Brady, E. C. (2014). Why is the AMOC monostable in coupled general circulation models? *Journal Of Climate*, **27**, 2427-2443. doi:10.1175/JCLI-D-13-00264.1

Liu, W., S.-P. Xie, Z. Liu and J. Zhu (2017). Overlooked possibility of a collapsed Atlantic Meridional Overturning Circulation in warming climate. *Sci. Adv.,* **3**, e1601666, doi:10.1126/sciadv.1601666.

Long, J.A., and P.C. Stoy (2013). Quantifying the periodicity of Heinrich and Dansgaard-Oeschger events during Marine Oxygen Isotope Stage 3, *Quaternary Research*, **79**, 413-423, doi:10.1016/j.yqres.2013.02.003.

Long, M. C., K. Lindsay, S. Peacock, J. K. Moore, and S. C. Doney, (2013). Twentieth-century oceanic carbon uptake and storage in CESM1(BGC). *J. Clim.*, **26**, 6775-6800, doi:10.1175/JCLI-D-12-00184.1.

Lorbacher, K., J. Dengg, C. W. Boning and A. Biastoch (2010). Regional patterns of sea level change related to interannual variability and multidecadal trends in the Atlantic meridional overturning circulation. *J. Clim.*, **23**, 4243–4254, doi:10.1175/2010JCLI3341.1.

Losch, M., A. Adcroft and J.-M. Campin (2004). How sensitive are coarse general circulation models to fundamental approximations in the equations of motion? *J. Phys. Oceanogr.*, **34**, 306–319, doi:10.1175/1520-0485(2004)034<0306:HSACGC>2.0.CO;2.

Lozier, M. S., et al. (2017). Overturning in the Subpolar North Atlantic Program: a new international ocean observing system. *Bull. Amer. Met. Soc.*, **98**, 737–752, doi:10.1175/BAMS-D-16-0057.1.

Lynch-Stieglitz, J. (2017). The Atlantic Meridional Overturning Circulation and Abrupt Climate Change. *Annu. Rev. Marine. Sci.,* **9**, 83-104, doi:10.1146/annurev-marine-010816-060415.

Mahajan et al. (2011). Predicting Atlantic meridional overturning circulation (AMOC) variations using subsurface and surface fingerprints, *Deep Sea Research Part II: Topical Studies in Oceanography,* **58**, 1895-1903, doi:10.1016/j.dsr2.2010.10.067

Marshall, J., Donohoe, A., Ferreira , D., and McGee, D. (2014). The ocean's role in setting the mean position of the Inter-Tropical Convergence Zone. *Clim. Dyn*., **42**, 1967–1979, doi:10.1007/s00382-013-1767-z.

Martin, G. M., et al. (2011). The HadGEM2 family of Met Office Unified Model climate configurations. *Geophys. Model Dev.*, **4**, 723–757, doi:10.5194/gmd-4-723-2011.

Masui, T., Matsumoto, K., Hijioka, Y. et al. (2011). An Emission Pathway for Stabilization at 6 Wm^{-2} Radiative Forcing. *Clim. Change*, **109,** 59-76, doi:10.1007/s10584-011-0150-5.

Maul, G. A., and K. Hanson (1991). Interannual coherence between North Atlantic atmospheric surface pressure and composite southern USA sea level. *Geophys. Res. Lett.,***18,** 653–656.

McCarthy, G. D., E. Frajka-Williams, W. E. Johns, M. O. Baringer, C. Meinen, H. L. Bryden, D. Rayner, A. Duchez and S. A. Cunningham (2012). Observed interannual variability of the Atlantic meridional overturning circulation at 26.5°N. *Geophys. Res. Lett.*, **39**, L19609, doi:10.1029/2012GL052933.

McCarthy, G.D., I.D. Haigh, J. J.-M. Hirschi, J.P. Grist, D. A. Smeed (2015). Ocean impact on decadal Atlantic climate variability revealed by sea-level observations. *Nature*, **521**, 508-510, doi:10.1038/nature14491.

McCarthy, G.D., D.A. Smeed, S.A. Cunningham and C.D. Roberts (2017). Atlantic meridional overturning circulation. *MCCIP Science Review 2017*, 15-21, doi:10.14465/2017.arc10.002-atl.

McManus, J. F., R. Francois, J.-M. Gherardi, L. D. Keigwin and S. Brown-Leger (2004). Collapse and rapid resumption of Atlantic meridional circulation linked to deglacial climate changes. *Nature*, **428**, 834–837, doi:10.1038/nature02494.

Medhaug, I., and T. Furevik (2011). North Atlantic 20th century multidecadal variability in coupled climate models: Sea surface temperature and ocean overturning circulation. *Ocean. Sci.,* **7**, 389–404, doi:10.5194/os-7-389-2011.

Meehl, G. A., et al. (2012). Climate System Response to External Forcings and Climate Change Projections in CCSM4. *J. Clim.*, **25**, 3661-3683, doi:10.1175JDLI-D-11-00240.1.

Meyssignac, B., et al. (2017). Evaluating Model Simulations of Twentieth-Century Sea-Level Rise. Part II: Regional Sea-Level Changes. *J. Clim.*, **30**, 8565-8593, doi:10.1175/JCLI-D-17-0112.1.

Mimura, N. (2013). Sea-level rise caused by climate change and its implications for society. *Proc. Jpn. Acad. Ser. B Phys. Biol. Sci.*, **89**, 281–301, doi:10.2183/pjab.89.281.

Minobe, S., M. Terada, B. Qiu and N. Schneider (2017). Western Boundary Sea Level: A Theory, Rule of Thumb, and Application to Climate Models. J. Phys. Oceanogr., **47**, 957–977, doi:10.1175/JPO-D-16-0144.1.

Muir, L.C. and A.V. Fedorov (2015). How the AMOC affects ocean temperatures on decadal to centennial timescales> the North Atlantic versus an interhemispheric seesaw. *Climate Dynamics***, 45,** 151-160. doi.org/10.1007/s00382-014-2443-7.

Muller, R. A., et al. (2013). Decadal variations in the global atmospheric land temperatures. *J. Geophysical: Atmospheres*, **118**, 5280-5286, doi/10.1002/jgrd.50458.

Munk, W., and C. Wunsch (1998). Abyssal recipes II: Energetics of tidal and wind mixing. *Deep Sea Res. Part I*, **45**, 1977–2010, doi:10.1016/S0967-0637(98)00070-3.

Muthers, S., C. C. Raible, E. Rozanov and T. F. Stocker (2016). Response of the AMOC to reduced solar radiation—the modulating role of atmospheric-chemistry. *Earth Syst. Dynam.,* **7,** 877-892, doi:10.5194/esd-7-877-2016.

Neale, R. B., et al. (2010). Description of the NCAR Community Atmosphere Model (CAM 4.0). *NCAR Technical Note NCAR/TN-486+STR*. National Center for Atmopsheric Research, Boulder, CO, April 2010, 268 pp. Downloaded September 2018 from www.cesm.ucar.edu/models/ccsm4.0/cam/docs/description/cam4_desc.pdf.

Orsi, A. H., Johnson, G. C., and Bullister, L. (1999). Circulation, mixing, and production of Antarctic Bottom Water. *Progress in Oceanography*, **43**, 55-109, doi:10.1016/S0079-6611(99)00004-X.

Ortega, P., J. Robson, R. T. Sutton and M. B. Andrews (2017). Mechanisms of decadal variability in the Labrador Sea and the wider North Atlantic in a high-resolution climate model. *Clim. Dyn.*, **49**, 2625–2647, doi:10.1007/s00382-016-3467-y.

Ostapoff, F. (1960). On the mass transport through the Drake Passage. *J. Geo. Res.*, **65**, 2861-2868, doi:10.1029/JZ065i009p02861.

Otterå, O. H., M. Bentsen, H. Drange and L. Suo (2010). External forcing as a metronome for Atlantic multidecadal variability. *Nature Geosci.*, **3**, 688–694, doi:10.1038/ngeo955.

Palter, J. B. (2014). The role of the Gulf Stream in European climate. *Annu. Rev. Mar. Sci.*, **7**, 113–37, doi:10.1146/ annurev-marine-010814-015656.

Palter, J. B., and M. S. Lozier (2008). On the source of Gulf Stream nutrients. *J. Geo. Res.*, **113**, C06018, doi:10.1029/2007JC004611.

Pardaens, A. K., J. M. Gregory and J. A. Lowe (2011). A model study of factors influencing projected changes in regional sea level over the twenty-first century. *Clim. Dyn.*, **36**, 2015–2033, doi:10.1007/s00382-009-0738-x.

Park, J. and W. Sweet (2015). Accelerated sea level rise and Florida current transport. *Ocean Sci*. **11**, 607-615, doi:10.5194/os-11-607-2015.

Parker, A. and C. Ollier (2016). Atlantic meridional overturning circulation stable over the last 150 years. *Quaestiones Geographicae,* **38**, 31-40, doi:10.2478/quageo-2019-0026.

Perez, F. F., et al. (2013). Atlantic Ocean CO2 uptake reduced by weakening of the Meridional Overturning Circulation. *Nature Geosci.*, **6**, 146-152, doi:10.1038/ngeo1680.

Peterson, R. G. (1988). On the transport of the Antarctic Circumpolar Current through Drake Passage and its relation to wind. *J. Geophys. Res.*, **93**, 13993–14004, doi:10.1029/JC093iC11p13993.

Peyser, C.W, and J. Yin (2017). Interannual and decadal variability in tropical Pacific sea level. *Water*, **9**, 402-14.

Piecuch, C. G. (2016). Understanding Tide Gauge Mean Sea Level Changes on the East Coast of North America. Open Access Dissertations, Paper 472, Downloaded April 2018 from http://digitalcommons.uri.edu/oa_diss/472.

Piecuch, C. G., S. Dangendorf, R. M., Ponte, M. Marcos (2016). Annual sea level changes on the North American Northeast Coast: Influence of local winds and barotropic motions. *Journal of Climate*, **29**, 4801–4816.

Piecuch, C. G., et al. (2019). How is New England Coastal Sea Level Related to the Atlantic Meridional Overturning Circulation at 26°N? Geo. Res. Lett., **46**, 5351-5360, doi:10.1029/2019GL083073.

Ponte, R. M., (1992). The sea level response of a stratified ocean to barometric pressure forcing. *J. Phys. Oceanogr.*, **22**, 109–113, doi:10.1175/1520-0485(1992)022<0109:TSLROA>2.0.CO;2.

Qiao, F., et al. (2013). Development and evaluation of an Earth System Model with surface gravity waves. *J. Geophys. Res. Oceans*, **118**, 4514–452, doi:10.1002/jgrc.20327.

Rahmstorf, S. (2002). Ocean circulation and climate during the past 120,000 years. *Nature*, **419**, 207-214, doi:10.1038/nature01090.

Rahmstorf, S., et al. (2005). Thermohaline circulation hysteresis: A model intercomparison. *Geo. Res. Lett.*, **32**, L23605, doi:10.1029/2005GL023655.

Rahmstorf, S., et al. (2015). Exceptional twentieth-century slowdown in Atlantic Ocean overturning circulation. *Nature Clim. Change*, **5**, 475-480, doi:10.1038/nclimate2554.

Reintges, A., T. Martin, M. Latif and N. S. Keenlyside (2016). Uncertainty in 21st Century Projections of the Atlantic Meridional Overturning Circulation in CMIP3 and CMIP5 models. *Clim. Dyn.*, **49**, doi:10.1007/s00382-016-3180-x.

Renssen, H., et al. (2015). Multiple causes of the Younger Dryas cold period. *Nature Geosci.*, **8**, 946–949, doi:10.1038/ngeo2557.

Riahi, K., et al. (2011). RCP 8.5 - A scenario of comparatively high greenhouse gas emissions. *Clim. Change*, **109**, 33–57, doi:10.1007/s10584-011-0149-y.

Ridley, J. K., P. Huybrechts, J. M. Gregory and J. A. Lowe (2005). Elimination of the Greenland Ice Sheet in a high CO2 climate. *J. Clim.*, **18**, 3409–3427, doi:10.1175/JCLI3482.1.

Rignot, E., I. Velicogna, M. R. van den Broeke, A. Monaghan and J. Lenaerts (2011). Acceleration of the contribution of the Greenlandand Antarctic ice sheets to sea level rise. *Geophys. Res. Lett.*, **38**, L05503, doi:10.1029/2011GL046583.

Roberts, C. D., and M. D. Palmer (2012). Detectability of changes to the Atlantic meridional overturning circulation in the Hadley Centre Climate Models. *Clim. Dyn.*, **39**, 2533–2546, doi:10.1007/s00382-012-1306-3.

Roberts, C. D, L. Jackson and D. McNeall (2014). Is the 2004–2012 reduction of the Atlantic meridional overturning circulation significant? *Geophys. Res. Lett.,* **41**, 3204-3210, doi:10.1002/2014GL059473.

Roberts, C. D., F. K. Garry and L. C. Jackson (2013). A multimodel study of sea surface temperature and subsurface density fingerprints of the Atlantic meridional overturning circulation. *J. Clim*., **26**, 9155-9174, doi:10.1175/JCLI-D-12-00762.1.

Robson, J., D. Hodson, E. Hawkins and R. Sutton (2014). Atlantic overturning in decline? *Nature Geosci*., **7**, 2-3, doi:10.1038/ngeo2050.

Romero-Lankao, P., J.B. Smith, D.J. Davidson, N.S. Diffenbaugh, P.L. Kinney, P. Kirshen, P. Kovacs, and L. Villers Ruiz. (2014). North America. In: *Climate Change 2014: Impacts, Adaptation, and Vulnerability. Part B: Regional Aspects. Contribution of Working Group II to the Fifth Assessment Report of the Intergovernmental Panel on Climate Change* [Barros, V.R., C.B. Field, D.J. Dokken, M.D. Mastrandrea, K.J. Mach, T.E. Bilir, M. Chatterjee, K.L. Ebi,Y.O. Estrada, R.C. Genova, B. Girma, E.S. Kissel, A.N. Levy, S. MacCracken, P.R. Mastrandrea, and L.L. White (eds.)]. Cambridge University Press, Cambridge, United Kingdom and New York, NY, USA, pp. 1439-1498.

Rooth, C. (1982). Hydrology and ocean circulation. *Prog. Oceanogr.*, **11**, 131–149, doi:10.1016/0079-6611(82)90006-4.

Rossby, T. and E. Gottlieb. (1998). The Oleander Project: Monitoring the variability of the Gulf Stream and adjacent waters between New Jersey and Bermuda. *Bulletin of the American Meteorological Society*, **79**, 5-18. doi:10.1175/1520-0477(1998)079<0005:TOPMTV>2.0.CO;2

Rossby, T., C. Flagg and K. Donohue (2010). On the variability of Gulf Stream transport from seasonal to decadal timescales. *J. Mar. Res.,* **68**, 503–522, doi:10.1357/002224010794657128.

Rossby, T., C. N. Flagg, K. Donohue, A. Sanchez-Franks and J. Lillibridge (2014). On the long-term stability of Gulf Stream transport based on 20 years of direct measurements. *Geophys. Res. Lett.*, **41**, 114-120, doi:10.1002/2013GL058636.

Rotstayn, L. D., et al. (2012). Aerosol- and greenhouse gas-induced changes in summer rainfall and circulation in the Australasian region: A study using single-forcing climate simulations. *Atmos. Chem. Phys.*, **12**, 6377–6404, doi:10.5194/acp-12-6377-2012.

Roussenov V. M, R. G. Williams, C. W. Hughes, and R. J. Bingham (2007). Boundary wave communication of bottom pressure and overturning changes for the North Atlantic. *J. Geophys. Res*., **113**, 1-12, doi:10.1029/2007JC004501

Sabine, C. L., et al. (2004). The oceanic sink for anthropogenic CO2. *Science*, **305**, 367–371, doi:10.1126/science.1097403.

Saenko, O. A., D. Yang, J. M. Gregory, P., Spence P. G. Myers (2015). Separating the influence of projected changes in air temperature and wind on patterns of sea level change and ocean heat content. *J. Geophy. Res. Oceans*, **120**, 5749–5765, doi:10.1002/jgrc.v120.8.

Sakamoto, T. T., et al. (2012). MIROC4h – a new high-resolution atmosphere-ocean coupled general circulation model. *J. Meteorol. Soc. Jpn.*, **90**, 325–359, doi:10.2151/jmsj.2012-301.

Sandström, J. W. (1916). Meteorologische Studien im Schwedischen Hochgebirge, *Göteborgs K. Vetensk. Vitterhetssamhällets Handkl.*, **27**, 48pp.

Sallenger, A. H., K. S. Doran and P. Howd (2012). Hotspot of accelerated sea-level rise on the Atlantic coast of North America. *Nat. Clim. Change*, **2**, 884–888, doi:10.1038/nclimate1597.

Sarnthein, M., et al. (1994). Changes in east Atlantic deep-water circulation over the last 30000 years: Eight time slice reconstructions. *Paleoceanography*, **9**, 209– 267, doi:10.1029/93PA03301.

Sarnthein, M., et al. (2001). Fundamental Modes and Abrupt Changes in North Atlantic Circulation and Climate over the last 60 ky — Concepts, Reconstruction and Numerical Modeling. In: Schäfer P., Ritzrau W., Schlüter M., Thiede J. (eds) *The Northern North Atlantic: A changing environment, Springer, Berlin*, 365–410, doi:10.1007/978-3-642-56876-3_21.

Schewe, J. (2007). The role of Southern Ocean winds for the global meridional overturning circulation in the Earth System Model of Intermediate Complexity CLIMBER-3α. Diploma Thesis at the Department of Physics, Freie Universität Berlin. Downloaded March 2018 from http://www.pikpotsdam.de/~schewe/publications/dpeffect.pdf .

Schiermeier, Q. (2014). Atlantic current strength declines. *Nature,* **509**, 270–271, doi:10.1038/509270a.

Schmidt, G. A., et al. (2006). Present day atmospheric simulations using GISS ModelE: Comparison to in-situ, satellite and reanalysis data. *J. Clim.*, **19**, 153–192, doi:10.1175/JCLI3612.1.

Schmittner, A. (2005). Decline of the marine ecosystem caused by a reduction in the Atlantic overturning circulation. *Nature*, **434**, 628-633, doi:10.1038/nature03476.

Schmitz, W. J. (1995). On the interbasin-scale thermohaline circulation. *Rev. Geophys.*, **33**, 151–173, doi:10.1029/95RG00879.

Scoccimarro, E., et al., (2011). Effects of tropical cyclones on ocean heat transport in a high resolution Coupled General Circulation Model. *J. Clim.*, **24**, 4368–4384, doi:10.1175/2011JCLI4104.1.

Sen Gupta, A., N. C. Jourdain, J. N. Brown and D. Monselesan (2013). Climate drift in the CMIP5 models. *J. Climate*, **26**, 8597–8615, doi:10.1175/JCLI-D-12-00521.1.

Sévellec, F., A.V. Fedorov and W. Liu (2017). Arctic sea-ice decline weakens the Atlantic Meridional Overturning Circulation. *Nature Clim. Change*, **7**, 604-610, doi:10.1038/nclimate3353.

Sgubin, G., D. Swingedouw, S. Drijfhout, Y. Mary and A. Bennabi (2017). Abrupt cooling over the North Atlantic in modern climate models. *Nat. Commun.*, **8**, 14375, doi:10.1038/ncomms14375.

Slangen, A., J. A. Church, X. Zhang and D. P. Monselesan (2015). The sea level response to external forcings in historical simulations of CMIP5 climate models. *J. Clim.,* **28**, 8521–8539, doi:10.1175/JCLI-D-15-0376.1.

Smeed, D. A., et al. (2014). Observed decline of the Atlantic meridional overturning circulation 2004-2012. *Ocean Sci*. **10**, 29-38 (2014).

Smeed, D. A., et al. (2018). The North Atlantic Ocean Is in a State of Reduced Overturning. *Geophys. Res. Lett.*, **45**, 1527-1533, doi:10.1002/2017GL076350.

Srokosz, M., et al. (2012). Past, Present, and Future Changes in the Atlantic Meridional Overturning Circulation. *Bull. Am. Meteorol. Soc.,* **93**, 1663-1676, doi:10.1175/BAMS-D-11-00151.1.

Srokosz, M. A., and H. L. Bryden (2015). Observing the Atlantic Meridional Overturning Circulation yields a decade of inevitable surprises. *Science*, **348**, 6241, doi:10.1126/science.1255575.

Stommel, H. M. (1961). Thermohaline convection with two stable regimes of flow. *Tellus*, **13**, 224–230, doi:10.1111/j.2153-3490.1961.tb00079.x.

Stouffer, R., et al. (2006). Investigating the causes of the response of the thermohaline circulation to past and future climate changes. *J. Clim*., **19**, 1365-1387, doi:10.1175/JCLI3689.1.

Sun, C., J. Li, and F.-F. Jin (2015). A delayed oscillator model for the quasi-periodic multidecadal variability of the NAO. *Climate Dynamics*, **45,** 2083-2099, doi:10.1007/s00382-014-2459-z.

Sutton, R., and Dong, B (2012). Atlantic Ocean influence on a shift in European climate in the 1990s. *Nature Geoscience*, **5**, 788-793, doi.org/10.1038/ngeo1595.

Sutton, R. T., and D. L. R. Hodson (2005). Atlantic Ocean forcing of North American and European summer climate. *Science*, **309**, 115–118, doi:10.1126/science.1109496.

Sweet, W., C. Zervas and S. Gill. (2009). Elevated east coast sea level anomaly: June-July 2009, NOAA Tech. Rep. No. NOS CO-OPS 051, NOAA National Ocean Service, Silver Spring, MD, Downloaded March 2018 from https://repository.library.noaa.gov/view/noaa/2569.

Swingedouw, D., C. B. Rodehacke, E. Behrens, M. Menary, S. M. Olsen, Y. Gao, U. Mikolajewicz, J. Mignot, and A. Biastoch (2013). Decadal fingerprints of freshwater discharge around Greenland in a multi-model ensemble, *Clim. Dyn.*, **41**, 695–720, doi:10.1007/s00382-012-1479-9.

Talley, L. D. (2013). Closure of the global overturning circulation through the Indian, Pacific, and Southern Oceans: Schematics and transports. Oceanography, **26**, 80-97, doi:10.5670/oceanog.2013.07.

Talley, L. D., J. L. Reid and P. E. Robbins (2003). Data-based meridional overturning streamfunctions for the global ocean. *J. Clim.*, **16,** 3213–3226, doi:10.1175/1520-0442(2003)016<3213:DMOSFT>2.0.CO;2.

Taylor, K. E. (2001). Summarizing multiple aspects of model performance in a single diagram. *J. Geophys. Res.*, **106**, 7183–7192, doi:10.1029/2000JD900719.

Taylor, K. E., R. J. Stouffer and G. A. Meehl (2012). An overview of CMIP5 and the experiment design. *Bull. Am. Meteorol. Soc.*, **93**, 485-498, doi:10.1175/BAMS-D-11-00094.1.

Thompson, K. R. (1986). North Atlantic sea-level and circulation. *Geophys. J. Int.*, **87**, 15–32, doi:10.1111/j.1365-246X.1986.tb04543.x.

Thompson, R. G., and G. T. Mitchum (2014). Coherent sea level variability on the North Atlantic western boundary. *J. Geophys. Res. Oceans*, **119**, 5676-5689, doi:10.1002/2014JC009999.

Thompson D.W.J, E.A. Barnes, C. Deser, W.E. Foust, A.S. Phillips (2015). Quantifying the role of internal climate variability in future climate trends. *J Clim*, **28**, 6443–6456, doi/10.1175/JCLI-D-14-00830.1.

Thomson, A. M., et al. (2011). RCP4.5: a pathway for stabilization of radiative forcing by 2100. *Clim. Change,* **109**, 77–94, doi:10.1007/s10584-011-0151-4.

Timmermann, A., M. Schulz, H. Gildor and E. Tziperman (2003). Coherent resonant millennial-scale climate oscillations triggered by massive meltwater pulses. *J. Climate*, **16**, 2569–2585, doi:10.1175/1520-0442%282003%29016%3C2569%3ACRMCOT%3E2.0.CO%3B2.

Toggweiler, J. R., and B. Samuels (1993). Is the magnitude of the deep outflow from the Atlantic ocean actually governed by southern hemisphere winds? In: Heimann M (ed.) The global carbon cycle. NATO ASI Ser. I, Springer-Verlag, doi:10.1007/978-3-642-84608-3_13.

Toggweiler, J. R., and B. Samuels (1995). Effect of Drake Passage on the global thermohaline circulation. *Deep-Sea Res. I.*, **42**, 477–500, doi:10.1016/0967-0637(95)00012-U.

Toggweiler, J. R., and B. Samuels (1998). On the ocean's large-scale circulation near the limit of no vertical mixing. *J. Phys. Oceanogr.*, **28**, 1832–1852, doi:10.1175/1520-0485(1998)028<1832:OTOSLS>2.0.CO;2.

Van Vuuren DP, J. Edmonds, A. Thomson, K. Riahi, M. Kainuma, T. Matsui, G.C. Hurtt, J.-F. Lamarque, M. Meinshausen, S. Smith et al (2011). Representative concentration pathways: an overview. *Clim. Change*, **109**, 5-31, doi.org/10.1007/s10584-011-0148-z.

Vellinga, M., and R. A. Wood (2002): Global climatic impacts of a collapse of the Atlantic thermohaline circulation. *Clim. Change*, **54**, 251-267, doi:10.1023/A:1016168827653.

Vellinga, M., and R. A. Wood (2008). Impacts of thermohaline circulation shutdown in the twenty-first century. *Clim. Change*, **91**, 43-44, doi:10.1007/s10584-006-9146-y.

Vichi, M., et al. (2011). Global and regional ocean carbon uptake and climate change: Sensitivity to a substantial mitigation scenario. *Clim. Dyn.*, **37**, 1929–1947, doi:10.1007/s00382-011-1079-0.

Visbeck, M., H. Cullen, G. Krahman and N. Naik (1998). An ocean model's response to North Atlantic Oscillation-like wind forcing. *Geophys. Res. Lett.*, **25**, 4521–4524, doi:10.1029/1998GL900162.

Visbeck, M. (2014). Bumpy path to a warmer world. *Nature Geoscience*, **7**, 160-161. doi:10.1038/ngeo2104

Voldoire, A., et al. (2013). The CNRM-CM5.1 global climate model: Description and basic evaluation. *Clim. Dyn.*, **40**, 2091–2121, doi:10.1007/S00382-011-1259-Y.

Volodin, E. M., N. A. Dianskii and A. V. Gusev (2010). Simulating present-day climate with the INMCM4.0 coupled model of the atmospheric and oceanic general circulations. *Izvestiya Atmos. Ocean. Phys.*, **46**, 414–431, doi:10.1134/S000143381004002X.

Wong, P.P., I.J. Losada, J.-P. Gattuso, J. Hinkel, A. Khattabi, K.L. McInnes, Y. Saito, and A. Sallenger. (2014). Coastal systems and low-lying areas. In: *Climate Change 2014: Impacts, Adaptation, and Vulnerability. Part A: Global and Sectoral Aspects. Contribution of Working Group II to the Fifth Assessment Report of the Intergovernmental Panel on Climate Change* [Field, C.B., V.R. Barros, D.J. Dokken, K.J. Mach, M.D. Mastrandrea, T.E. Bilir, M. Chatterjee, K.L. Ebi, Y.O. Estrada, R.C. Genova, B. Girma, E.S. Kissel, A.N. Levy, S. MacCracken, P.R. Mastrandrea, and L.L. White (eds.)]. Cambridge University Press, Cambridge, United Kingdom and New York, NY, USA, pp. 361-409

Wang, Z., D. Brickman, and B.J.W. Greeman (2019). Characteristic evolution of the Atlantic meridional overturning circulation from 1990 to 2015: An eddy-resolving ocean model study, Deep Sea Res Part 1: *Ocean. Res. Papers*, **149,** 102056, doi:10.1016/j.dsr.2019.06.002

Watanabe, M., M. Chikira, Y. Imada and M. Kimoto (2011). Convective control of ENSO simulated in MIROC. *J. Clim.*, **24**, 543–562, doi:10.1175/2010JCLI3878.1.

Watanabe, M., et al. (2010). Improved climate simulation by MIROC5: Mean states, variability, and climate sensitivity. *J. Clim.*, **23**, 6312–6335, doi:10.1175/2010JCLI3679.1.

Weaver, A. J., et al. (2012). Stability of the Atlantic meridional overturning circulation: A model intercomparison. *Geophys. Res. Lett.,* **39**, L20709, doi:10.1029/2012GL053763.

Weber, S. L., et al. (2007). The modern and glacial overturning circulation in the Atlantic Ocean in PMIP coupled model simulations. *Clim. Past*, **3**, 51–64, doi:10.5194/cp-3-51-2007.

Weigel, A.P., R. Knutti, M.A. Liniger and C. Appenzeller (2010). Risk of Model Weighting in Multimodel Climate Projections. *J. Climate*, 1**5**, 4175-4191, doi.org/10.1175/2010JCLI3594.1.

Weijer, W., W. P. M. De Ruijter, H. A. Dijkstra and P. J. van Leeuwen (1999). Impact of interbasin exchange on Atlantic overturning. *J. Phys. Oceanogr.*, **29**, 2266–2284, doi:10.1175/1520-0485(1999)029<2266:IOIEOT>2.0.CO;2.

Woodworth, P., C. Hughes, R. Bingham, and T. Gruber (2012). Towards worldwide height system unification using ocean information, *J. Geod. Sci.*, **2**, 302–318, doi:10.2478/v10156-012-0004-8.

Woodworth, P. L., M. A. Morales Maqueda, V. M. Roussenov, R. G. Williams and C. W. Hughes (2014). Mean sea-level variability along the northeast American Atlantic coast and the roles of the wind and the overturning circulation. *J. Geophys. Res.-Oceans*, **119**, 8916–8935, doi:10.1002/2014JC010520.

Wu, L., and Z. Liu (2005). North Atlantic decadal variability: Air-sea coupling, oceanic memory, and potential Northern hemisphere resonance*. *J. of Climate*, **18**, 331-349, doi/full/10.1175/JCLI-3264.1.

Wu, T., et al. (2014). An overview of BCC climate system model development and application for climate change studies. J. Met. Res., **28**, 34–56, doi:10.1007/s13351-014-3041-7.

Wunsch, C. (2008). Mass and volume transport variability in an eddy-filled ocean. *Nature Geoscience*, **1**, 165–168, doi:10.1038/ngeo126

Wunsch, C., and D. Stammer (1997). Atmospheric loading and the oceanic "inverted barometer" effect. *Rev. Geophys.*, **35**, 79-107, doi:10.1029/96rg03037.

Xu, X., E. P. Chassignet and F. Wang (2019). On the variability of the Atlantic meridional overturning circulation transports in coupled CMIP5 simulations. *Clim. Dyn.*, **52**, 6511-6531, doi:10.1007/s00382-018-4529-0.

Yamamoto, A., J. B. Palter, M. S. Lozier, M. S. Bourqui and S. J. Leadbetter (2015). Ocean versus atmosphere control on western European wintertime temperature variability. *Clim. Dyn.*, **45**, 3593–3607, doi:10.1007/s00382-015-2558-5.

Yamamoto A., H. Tatebe, and M. Nonaka (2018). On the existence of a potential multidecadal AMOC-AMO-NAO feedback loop in MIROC. *Geophysical Research Abstracts*, **20**, EGU2018-11708.

Yan, X., R. Zhang, and T.R. Knutson (2018). Underestimated AMOC variability and implications for AMV and predictability in CMIP5 models. *Geophys. Res. Lett.,* **45**, 4319-4328, doi:10.1029/2018GL077378.

Yang, Q., T. H. Dixon and S. Wdowinski (2013). Annual variation of coastal uplift in Greenland as an indicator of variable and accelerating ice mass loss. *Geochem. Geophys. Geosyst.*, **14**, 1569–1589, doi:10.1002/ggge.20089.

Yang, Q., et al. (2016). Recent increases in Arctic freshwater flux affects Labrador Sea convection and Atlantic overturning circulation. *Nature Commun.*, **7**, 10525, doi:10.1038/ncomms10525.

Yeager, S. G., and M. Jochum (2009). The connection between Labrador Sea buoyancy loss, deep western boundary current strength, and Gulf Stream path in an ocean circulation model. *Ocean Modell.*, **30**, 207–224, doi:10.1016/j.ocemod.2009.06.014.

Yin, J. (2012). Century to multi-century sea level rise projections from CMIP5 models. *Geophys. Res. Lett.*, **39**, L17709, doi:10.1029/2012GL052947.

Yin, J., and P. B. Goddard (2013). Oceanic control of sea level rise patterns along the East coast of the United States. *Geophys. Res. Lett.,* **40**, 5514-5520, doi:10.1002/2013GL057992.

Yin, J., M. E. Schlesinger and R. J. Stouffer (2009). Model projections of rapid sea-level rise on the northeast coast of the United States. *Nature Geosci.,* **2**, 262-266, doi:10.1038/ngeo462.

Yin, J., S. M. Griffies and R. J. Stouffer (2010). Spatial Variability of Sea Level Rise in Twenty-First Century Projections. *J. Clim.,* **23**, 4585-4607, doi:10.1175/2010JCLI3533.1.

Yukimoto, S., et al. (2012). A new global climate model of the Meteorological Research Institute: MRI-CGCM3–Model description and basic performance. *J. Meteorol. Soc. Jpn.*, **90A**, 23–64, doi:10.2151/jmsj.2012-A02.

Zhang, R. (2008). Coherent surface-subsurface fingerprint of the Atlantic meridional overturning circulation. *Geophys. Res. Lett.,* **35**, L20705, doi:10.1029/2008GL035463.

Zhang, R. (2010). Latitudinal dependence of Atlantic meridional overturning circulation (AMOC) variations. *Geophys. Res. Lett.*, **37**, L16703, doi:10.1029/2010GL044474.

Zhang, R., and T. L. Delworth (2005). Simulated Tropical Response to a Substantial Weakening of the Atlantic Thermohaline Circulation. *J. Clim.*, **18**, 1853-1860, doi:10.1175/JCLI3460.1.

Zhang, R., and T. L. Delworth (2006). Impact of Atlantic multidecadal oscillations on India/Sahel rainfall and Atlantic hurricanes. *Geophys. Res. Lett*., **33**, L17712, doi.org/10.1029/2006GL026267.

Zhang, L., and C. Wang (2013). Multidecadal North Atlantic sea surface temperature and Atlantic meridional overturning circulation variability in CMIP5 historical simulations, *J. Geophys. Res*. *Oceans*, **118,** 5772–5791, doi:10.1002/jgrc.20390.

Zhang, R., et al. (2011). Sensitivity of the North Atlantic Ocean Circulation to an abrupt change in the Nordic Sea overflow in a high resolution global coupled climate model. *J. Geophys. Res*. *Oceans*, **116**, C12024, doi:10.1029/2011JC007240.

Appendix

Model Number	Modelling Centre	Model Code	Ocean Model	Atmosphere Model	Sea Ice Model	Integral Period	Ensemble Size
1	Commonwealth Scientific and Industrial Research Organisation (CSIRO) and Bureau of Meteorology, Australia (BOM)	ACCESS1-0 **(*1)**	NOAA/GFDL MOM4p1	AGCM	CICE4.1	1850-2005	2
2		ACCESS1-3 **(*2)**	MOM4p1	GA 1.0	CICE4.1	1850-2005	3
3	Beijing Climate Centre, China Meteorological Administration	bcc-csm1-1 **(*3)**	MOM4-L40	BCC-AGCM2.1	SIS	1850-2012	3
4		bcc-csm1-1-m **(*4)**	MOM4-L40	BCC-CSM1.1(M)	SIS	1850-2012	3
5	College of Global Change and Earth System Science Beijing Normal University	BNU-ESM	MOM4P1	CAM4	CICE4		
6	Canadian Centre for Climate Modelling and Analysis	CanCM4	CANOM4	CANAM4	CANSIM1	1961-2005	10
7		CanESM2 **(*5)**	CANOM4 AND CMOC1.2	CANAM4	CANSIM1	1850-2005	5
8		CCSM4 **(*6)**	POP2	CAM	CICE	1850-2005	6
9	Community Earth System Model Contributors	CESM1-BGC **(*7)**	POP2	CAM	CICE	1850-2005	1
10		CESM1-CAM5-1-FV2	POP2	CAM	CICE		
11		CESM1-CAM5 **(*8)**	POP2	CAM	CICE	1850-2005	3
12		CESM1-FASTCHEM **(*9)**	POP2	CAM	CICE	1850-2005	3
13		CESM1-WACCM **(*10)**	POP2	WACCAM	CICE	1850-2005	4
14	Centro Euro-Mediterraneo per I Cambiamenti Climatici	CMCC-CESM **(*11)**	NEMO/OPA8.2	ECHAM5	LIM2	1850-2005	1
15		CMCC-CM **(*12)**	NEMO/OPA8.2	ECHAM5	LIM2	1850-2005	1
16		CMCC-CMS **(*13)**	NEMO/OPA8.2	ECHAM5	LIM2	1850-2005	1
17	Centre National de Recherches Météorologiques / Centre Européen de Recherche et Formation Avancée en Calcul Scientifique	CNRM-CM5-2 **(*14)**	NEMO	ARPEGE	GELATO	1850-2005	1
18		CNRM-CM5 **(*15)**	NEMO	ARPEGE	GELATO	1850-2005	10
19	Commonwealth Scientific and Industrial Research Organisation in collaboration with Queensland Climate Change Centre of Excellence	CSIRO-Mk3-6-0 **(*16)**	MOM2.2	CSIRO AGCM		1850-2005	10
20	EC-EARTH consortium	EC-EARTH **(*17)**	NEMO	EC-EARTH IFS	LIM2	1850-2005	13
21	LASG, Institute of Atmospheric Physics, Chinese Academy of Sciences and CESS,Tsinghua University	FGOALS-*g2* **(*18)**	LICOM2	GAMIL2	CICE4-LASG	1850-2005	5
22	LASG, Institute of Atmospheric Physics, Chinese Academy of Sciences	FGOALS-s2 **(*19)**	LICOM2	SAMIL2	CSIM5	1850-2005	3
23	The First Institute of Oceanography, SOA, China	FIO-ESM **(*20)**	POP2.0	CAM3	CICE4	1850-2005	3
24	NOAA Geophysical Fluid Dynamics Laboratory	GFDL-CM2p1 **(*21)**	MOM4.1	Included	SIS	1861-2040	10
25		GFDL-CM3 **(*22)**	MOM4.1	Included	SIS	1860-2005	2
26		GFDL-ESM2G **(*23)**	GOLD	Included	SIS	1861-2005	1
27		GFDL-ESM2M **(*24)**	MOM4.1	Included	SIS	1861-2005	1
28	NASA Goddard Institute for Space Studies	GISS-E2-H-CC	HYCOM	TCAD	Included		
29		GISS-E2-H	HYCOM	TCAD	Included		
30		GISS-E2-R-CC **(*25)**	Russell	TCAD	Included	1850-2010	1
31		GISS-E2-R **(*26)**	Russell	TCAD	Included	1850-2005	24
32	Met Office Hadley Centre	HadCM3	HadOM	HadAM3	Included		
33	National Institute of Meteorological Research/Korea Meteorological Administration	HadGEM2-AO	HADGEM2 Included	HadGAM2	Included		
34	Met Office Hadley Centre	HadGEM2-CC **(*27)**	HADGEM2 Included	HadGAM2	Included	1859-2005	3
35		HadGEM2-ES **(*28)**	HADGEM2 Included	HadGAM2	Included	1859-2005	5
36	Institute for Numerical Mathematics	inmcm4	Included	Included	Included	1850-2005	1
37	Institut Pierre-Simon Laplace	IPSL-CM5A-LR **(*29)**	NEMO	LMDz5	LIM2	1850-2005	6
38		IPSL-CM5A-MR **(*30)**	NEMO	LMDz5	Included	1850-2005	3
39		IPSL-CM5B-LR **(*31)**	NEMO	LMDz	Included	1850-2005	1
40	Atmosphere and Ocean Research Institute (The University of Tokyo), National Institute for Environmental Studies, and Japan Agency for Marine-Earth Science and Technology	MIROC4h **(*32)**	COC3.4	CCSR/NIES/FRCGC	Included	1850-2005	3
41		MIROC5 **(*33)**	COC3.4	MIROC-AGCM	Included	1850-2012	5
42	Japan Agency for Marine Earth Science and Technology, Atmosphere and Ocean Research Institute (The University of Tokyo) and National Institute for Environmental Studies	MIROC-ESM-CHEM **(*34)**	COC3.4	MIROC-AGCM	Included	1850-2005	1
43		MIROC-ESM **(*35)**	COC3.4	MIROC-AGCM	Included	1850-2005	3
44	Max Planck Institute	MPI-ESM-LR **(*36)**	MPIOM	ECHAM6	MPIOM	1850-2005	3
45		MPI-ESM-MR **(*37)**	MPIOM	ECHAM6	MPIOM	1850-2005	3
46		MPI-ESM-P **(*38)**	MPIOM	ECHAM6	MPIOM	1850-2005	2
47	Meteorological Research Institute	MRI-CGCM3 **(*39)**	MRI.COM3	MRI-AGCM3	Incl. MRI.COM3	1850-2005	5
48		MRI-ESM1 **(*40)**	MEI.COM3	MRI.AGCM3	Incl. MRI.COM3	1851-2005	1
49	Norwegian Climate Centre	NorESM1-ME **(*41)**	HAMOCC/MICOM	CAM4-Oslo	CICE4	1850-2005	1
50		NorESM1-M **(*42)**	HAMOCC/MICOM	CAM4	CICE	1850-2005	3

Model Number	Model Code	Horizontal Grid Points	Horizontal Resolution	Vertical Levels	Horizontal Grid System	Vertical Grid System	Reference(s)
1	ACCESS1-0 **(*1)**	360x300	1.00 x 0.60	50	D	z*	Bi et al. (2013), Franklin et al. (2013), Dix et al. (2013)
2	ACCESS1-3 **(*2)**	360x300	1.00 x 0.60	50	D	z*	Bi et al. (2013), Franklin et al. (2013), Dix et al. (2013)
3	bcc-csm1-1 **(*3)**	360x232	1.00 x 0.78	40	D	z	Wu et al. (2014)
4	bcc-csm1-1-m **(*4)**	360x232	1.00 x 0.78	40	D	z	Wu et al. (2014)
5	BNU-ESM	360x200	1.00 x 0.90	50	R		Ji et al. (2014)
6	CanCM4	256x192	1.41 x 0.94	40	R	z	Merryfield et al. (2014)
7	CanESM2 **(*5)**	256x192	1.41 x 0.94	40	R	z	Arora et al. (2011)
8	CCSM4 **(*6)**	320x384	1.13 x 0.47	60	D	depth (level)	Gent et al (2011), Lawrence et al. (2011), Meehl et al. (2012)
9	CESM1-BGC **(*7)**	320x384	1.13 x 0.47	60	D	depth (level)	Gent et al. (2011), Long et al. (2013)
10	CESM1-CAM5-1-FV2	320x384	1.13 x 0.47	60	D	depth (level)	Neale et al. (2010), Gent et al. (2011)
11	CESM1-CAM5 **(*8)**	320x384	1.13 x 0.47	60	D	z	Neale et al. (2010), Gent et al. (2011)
12	CESM1-FASTCHEM **(*9)**	320x384	1.13 x 0.47	60	D	depth (level)	Gent et al. (2011), Lamarque et al. (2012)
13	CESM1-WACCM **(*10)**	320x384	1.13 x 0.47	60	D	depth (level)	Calvo et al. (2012), Gent et al. (2011)
14	CMCC-CESM **(*11)**	182x149	1.98 x 1.21	31	D	depth (z-level)	Fogli et al. (2009)
15	CMCC-CM **(*12)**	182x149	1.98 x 1.21	31	D	z	Scoccimarro et al. (2011), Vichi et al. (2011)
16	CMCC-CMS **(*13)**	182x149	1.98 x 1.21	31	D	z	Fogli et al. (2009)
17	CNRM-CM5-2 **(*14)**	362x292	0.99 x 0.62	42	D	z	Voldoire et al. (2012)
18	CNRM-CM5 **(*15)**	362x292	0.99 x 0.62	42	D	z	Voldoire et al. (2012)
19	CSIRO-Mk3-6-0 **(*16)**	192x189	1.88 x 0.95	31	R	z	Rotstayn et al. (2012)
20	EC-EARTH **(*17)**	362x292	0.99 x 0.62	42	D	z	Hazeleger et al. (2012)
21	FGOALS-g2 **(*18)**	360x196	1.00 x 0.92	30	R	z*	Li et al. (2013)
22	FGOALS-s2 **(*19)**	360x196	1.00 x 0.92	30	R	depth	Bao et al. (2013)
23	FIO-ESM **(*20)**	320x384	1.13 x 0.47	40	D	depth	Qiao et al. (2013)
24	GFDL-CM2p1 **(*21)**	360x200	1.00 x 0.90	50	D	depth	Delworth et al. (2006)
25	GFDL-CM3 **(*22)**	360x200	1.00 x 0.90	50	D	z*	Donner et al. (2011)
26	GFDL-ESM2G **(*23)**	360x210	1.00 x 0.86	50	D	isopycnic	Dunne et al. (2012)
27	GFDL-ESM2M **(*24)**	360x200	1.00 x 0.86	50	D	z*	Dunne et al. (2012)
28	GISS-E2-H-CC	360x180	1.00 x 1.00	33	R	hybrid z-isopycnic	Schmidt et al. (2006)
29	GISS-E2-H	360x180	1.00 x 1.00	33	R	hybrid z-isopycnic	Schmidt et al. (2006)
30	GISS-E2-R-CC **(*25)**	288x180	1.25 x 1.00	32	R	z*	Schmidt et al. (2006)
31	GISS-E2-R **(*26)**	288x180	1.25 x 1.00	32	R	z*	Schmidt et al. (2006)
32	HadCM3	288x144	1.25 x 1.25	20	R	z	Gordon et al. (2000)
33	HadGEM2-AO	360x216	1.00 x 0.83	40	R	z	Martin et al. (2011)
34	HadGEM2-CC **(*27)**	360x216	1.00 x 0.83	40	R	z	Collins et al. (2011), Martin et al. (2011)
35	HadGEM2-ES **(*28)**	360x216	1.00 x 0.83	40	R	z	Collins et al. (2011)
36	inmcm4	360x340	1.00 x 0.53	40	D	σ	Volodin et al. (2010)
37	IPSL-CM5A-LR **(*29)**	182x149	1.98 x 1.21	31	D	z	Dufresne et al. (2013)
38	IPSL-CM5A-MR **(*30)**	182x149	1.98 x 1.21	31	D	z	Dufresne et al. (2013)
39	IPSL-CM5B-LR **(*31)**	182x149	1.98 x 1.21	31	D	z depth	Dufresne et al. (2013)
40	MIROC4h **(*32)**	1280x912	0.28 x 0.20	48	D	hybrid σ-z	Sakamoto et al. (2012)
41	MIROC5 **(*33)**	256x224	1.41 x 0.80	50	D	hybrid σ-z	Watanabe et al. (2010)
42	MIROC-ESM-CHEM **(*34)**	256x192	1.41 x 0.94	44	R	hybrid σ-z	Watanabe et al. (2011)
43	MIROC-ESM **(*35)**	256x192	1.41 x 0.94	44	R	hybrid σ-z	Watanabe et al. (2011)
44	MPI-ESM-LR **(*36)**	256x220	1.41 x 0.82	40	D	z	Giorgetta et al. (2013)
45	MPI-ESM-MR **(*37)**	802x404	0.45 x 0.45	40	D	z	Giorgetta et al. (2013)
46	MPI-ESM-P **(*38)**	256x220	1.41 x 0.82	40	D	z depth	Giorgetta et al. (2013)
47	MRI-CGCM3 **(*39)**	360x368	1.00 x 0.49	51	D	hybrid σ-z	Yukimoto et al. (2012)
48	MRI-ESM1 **(*40)**	360x368	1.00 x 0.49	51	D	hybrid σ-z	Yukimoto et al. (2012)
49	NorESM1-ME **(*41)**	320x384	1.13 x 0.47	70	D	hybrid z-isopycnic	Bentsen et al. (2013), Iversen et al. (2013)
50	NorESM1-M **(*42)**	320x384	1.13 x 0.47	70	D	hybrid z-isopycnic	Bentsen et al. (2013), Iversen et al. (2013)

Table S1. Detailed overview of CMIP5 models. * next to model name indicates the respective model (number 1-42) examined in the AMOC-sea level relationship, if not otherwise given by model names. Z=depth-geopotential coordinate, σ=terrain-following coordinate. For horizontal resolution, longitude is listed before latitude.

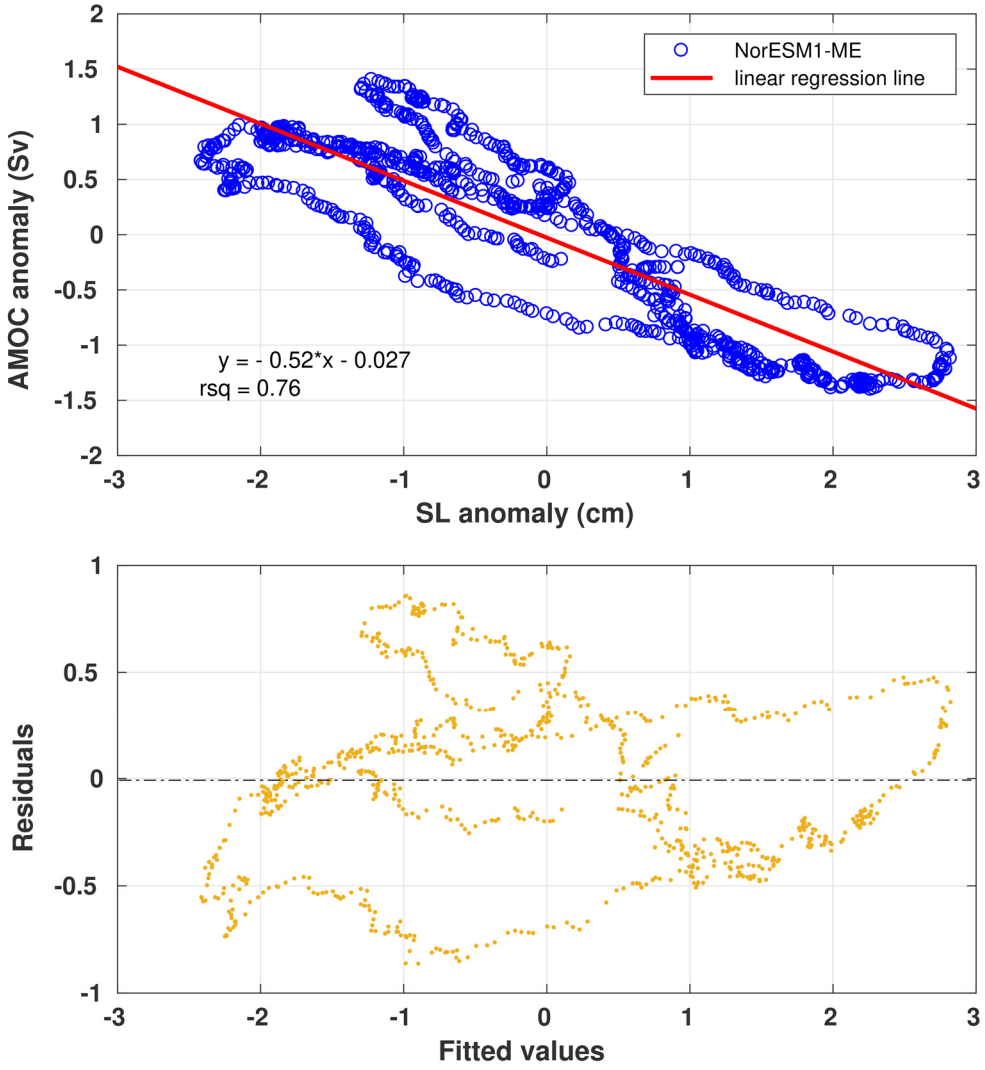

Figure S1. Scatterplot of simulated decadal coastal sea level variability against AMOC transport at 40.7°N (New York City) for NorESM1-ME 1920-2006. Linear regression line by least squares (red). Scatterplot of residuals (amber). Time mean, linear trend and seasonal cycle removed, and 121-month lowpass filter applied.